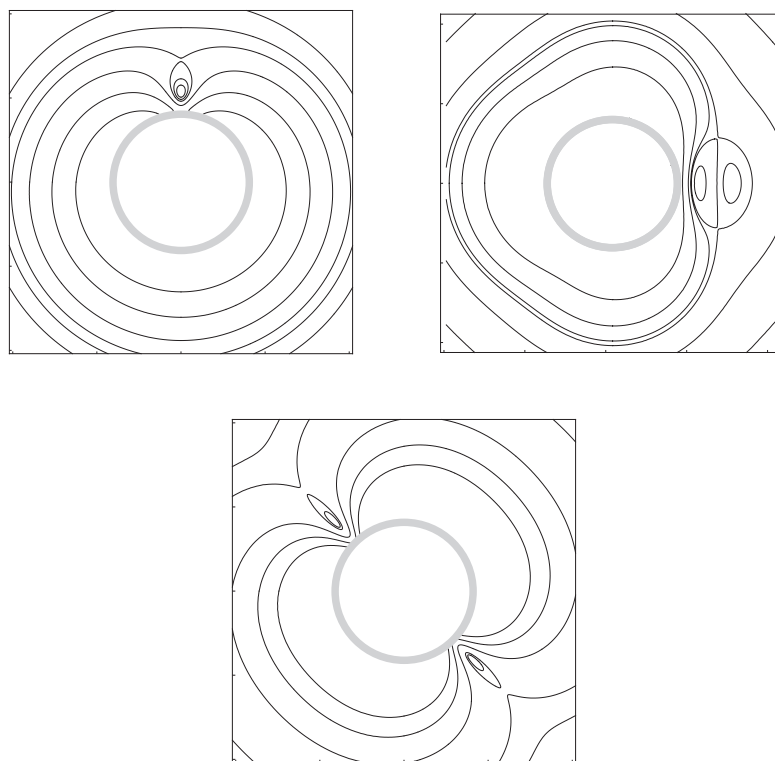


Light induced trapping potential for neutral atoms by mode interference of a blue detuned light field in ultra thin fibres

Diplomarbeit von Alexander Baade



vorgelegt bei

Prof. Dr. Arno Rauschenbeutel

Institut für Physik der
Johannes Gutenberg-Universität Mainz

09. März 2009

1. Gutachter: Prof. Dr. Arno Rauschenbeutel
2. Gutachter: Prof. Dr. Jochen Walz

Contents

1	Introduction	1
2	Propagation of light in optical fibres	3
2.1	Wave equations	3
2.2	Propagation of light in a step-index circular waveguide	5
2.3	Propagating modes	8
2.4	Mode propagation in ultra thin optical fibres	11
2.4.1	The fundamental HE_{11} mode with quasi-linear polarisation	12
2.4.2	The HE_{21} mode with quasi-linear polarisation	16
2.4.3	The TE_{01} mode	18
2.4.4	The TM_{01} mode	20
3	Mode Interference Traps	23
3.1	The optical potential	24
3.2	$HE_{11}+TE_{01}$ trap	26
3.3	$HE_{11}+HE_{21}$ trap	32
3.4	$HE_{21}+TE_{01}$ trap	35
3.5	Traps using the TM_{01} mode	37
3.6	Loading the traps	38
3.7	Summary	38
4	Investigation of modes in ultra thin optical fibres	41
4.1	Fibre tapering	41
4.2	Examination of the modes during the fibre pulling process	43
4.2.1	Intensity distribution between the different modes	44
4.2.2	Mode interference during the tapering process	45
4.2.3	Fibre diameter examination	48
4.2.4	Minimum fibre radius for light propagation	48
4.3	Investigation of the evanescent field of the HE_{11} mode	50
4.3.1	Evanescent coupling between two fibres	51
4.3.2	Experimental setup	53
4.3.3	Azimuthal investigation of an evanescent light field	56
4.3.4	Radial investigation of the evanescent light field	58
4.3.5	Longitudinal investigation of the evanescent light field	62
5	Summary and Outlook	67
A	Energy level diagram for Caesium	69

B Piezo calibration	71
Graphics Index	73
Tables Index	75
Bibliography	77

1 Introduction

When Sir Isaac Newton examined total internal reflection in the 18th century, he discovered that when bringing two dioptries next to each other without them being in contact, some light that should be reflected would instead cross the small gap and be transmitted by the second dioptry. Without the means to explain this phenomenon, he gave a purely descriptive analysis [1]. A more quantitative approach was taken by Quincke in 1966 [2] on whose observations a series of experimental and theoretical treatments were based [3, 4].

If a propagating light field is reflected at the boundary between two media, it does not drop instantly to zero, but rather decays quasi-exponentially from the interface on a scale of the field's wavelength in the form of an evanescent field. This leads to a finite probability to find the photon on the outside of the guiding medium. This quasi-exponential decay has been experimentally validated, for example by using fibre tips [5].

The evanescent light field is able to couple to matter via the optical dipole force [6], which can be repulsive or attractive, depending on the detuning of the light field with respect to the working transition. This can be used, for example to build atomic mirrors on planar surfaces [7]. In 1997 a gravito-optical surface trap (GOST) [8] that used the evanescent field in combination with the field of gravity on a flat dielectric surface to trap atoms next to the surface was realised. A further application for evanescent fields are hollow atomic wave guides [9]. These use the repulsive potential of the evanescent field on the inside of a tube to lead atoms along the axial direction of the guide.

The inverse case, where the light inside a waveguide causes an evanescent field on the outside can be found in tapered optical fibres (TOF). Here, the light is guided inside the fibre by total internal reflection and like in the case of Newton's experiment, the light projects over the guiding bulk of the fibre. If the fibre is fabricated with a diameter that is similar to the guided light's wavelength, it gives rise to a pronounced evanescent field. In recent years various laboratories have developed the facilities to manufacture these subwavelength diameter fibres [10, 11, 12, 13]. Tapered optical fibres offer a number of interesting properties that make them attractive for scientists. They combine tight transversal confinement and a pronounced evanescent field which enhances the coupling between light and matter. This has led to a variety of experiments using such fibres: "slow light" experiments [14] or spectroscopical applications [15, 16]. Furthermore, the strong radial confinement is maintained over the complete length of the fibre waist, which, in our case, can be as long as 5 mm. This surpasses the Rayleigh length of a freely propagating beam of a comparable diameter by several orders of magnitude. This led to the idea of using the evanescent field around a TOF to trap cold atoms in the vicinity of the fibre, which was first proposed by J.P. Dowling [17]. A more recent proposal by V.I. Balykin suggests using the superposition of the repulsive and attractive potential of the evanescent fields of a blue-detuned and red-detuned light field propagating in the same fibre to create a potential well for atoms [18]. This proposal has just recently been experimentally realised in our group [19].

In this thesis a similar idea to the proposal [18] is explored. Instead of using the superposition of two light fields travelling in the fundamental transversal mode, the interference pattern of two transversal fibre modes of the same blue-detuned light field is used.

This thesis is structured as follows: Chapter 2 gives the theoretical background of light propagation in fibres and discusses the properties of sub-wavelength optical fibres. An analysis of the spatial fibre modes and their evanescent field is given. Chapter 3 describes the fibre based atom traps using the interference of more than one mode in a fibre. Chapter 4 presents the experimental part of this work: A method to investigate the simultaneous propagation of a few modes in a subwavelength-diameter optical fibre is described and the results are discussed. In order to non-destructively measure the evanescent field arising around the waist of a tapered optical fibre, a near-field probing method using a second tapered fibre as a probe has been developed and successfully implemented. Finally, chapter 5 summarizes the results obtained and gives an outlook to what is possible with the experimental setup and what questions are worth examining in the future.

Parts of this thesis have been published in the following journal article:

G. Sagué, A. Baade and A. Rauschenbeutel. Blue-detuned evanescent field surface traps for neutral atoms based on mode interference in ultra thin optical fibres, *New J. Phys.* **10** 113008, 2008.

2 Propagation of light in optical fibres

Glass fibres have become a standard tool in telecommunication in the last decade, due to their effectiveness in transmitting signals over large distances while at the same time showing a larger resistance to environmental influences than the conventional copper cable.

A standard optical telecommunications fibre consists mainly of three parts, as is shown in figure 2.1 : The silica core has a typical diameter of $8 - 10 \mu\text{m}$, where the light is guided. It is embedded in a much larger silica cladding, with a typical diameter of about $125 \mu\text{m}$. The core is doped to increase its refractive index over that of the cladding, thus enabling guiding of light in the core via total internal reflection [20]. The difference in refractive indices between core and cladding is typically less than one percent, in which case the fibre is said to be weakly guiding, as it only accepts light with a small angle of incidence with respect to the fibre axis. To mechanically protect the fibre, the cladding is surrounded by a layer of synthetic material, the buffer (often some sort of acrylate [21]), which is about twice in diameter as the cladding.

In this section a short introduction to the propagation of light in such fibres and a discussion of the arising modes will be given. The description will closely follow the treatment given in [22, 23].

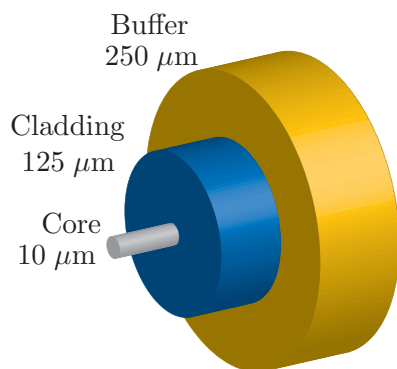


FIGURE 2.1: Schematic of a telecommunication step index fibre

2.1 Wave equations

The wave equation for light propagation in an isotropic charge free medium is given by [22]:

$$\nabla^2 \vec{E} - \mu\epsilon \frac{\partial^2 \vec{E}}{\partial t^2} = -\nabla \left(\frac{1}{\epsilon} \vec{E} \cdot \vec{\nabla} \epsilon \right), \quad (2.1)$$

where \vec{E} is the electric field vector, μ is the magnetic permeability of the medium and ϵ is the electric permittivity of the medium.

Since the fibre is cylindrically symmetric, it is convenient to use the cylindrical coordinate system. The electric and magnetic components of the light field will thus be denoted $E_r, E_\phi, E_z, H_r, H_\phi$ and H_z , respectively.

Using Maxwell's equations in cylindrical coordinates [22]

$$\begin{aligned} i\omega\varepsilon E_r &= i\beta H_\phi + \frac{1}{r} \frac{\partial}{\partial \phi} H_z \\ i\omega\varepsilon E_\phi &= -i\beta H_r - \frac{\partial}{\partial r} H_z \\ i\omega\varepsilon E_z &= -\frac{1}{r} \frac{\partial}{\partial \phi} H_r + \frac{1}{r} \frac{\partial}{\partial r} (r H_\phi) \end{aligned} \quad (2.2)$$

$$\begin{aligned} -i\omega\mu H_r &= i\beta E_\phi + \frac{1}{r} \frac{\partial}{\partial \phi} E_z \\ -i\omega\mu H_\phi &= -i\beta E_r - \frac{\partial}{\partial r} E_z \\ -i\omega\mu H_z &= -\frac{1}{r} \frac{\partial}{\partial \phi} E_r + \frac{1}{r} \frac{\partial}{\partial r} (r E_\phi), \end{aligned} \quad (2.3)$$

one can express all remaining components in terms of E_z and H_z :

$$\begin{aligned} E_r &= \frac{-i\beta}{\omega^2\mu\varepsilon - \beta^2} \left(\frac{\partial}{\partial r} E_z + \frac{\omega\mu}{\beta} \frac{\partial}{r\partial\phi} H_z \right) \\ E_\phi &= \frac{-i\beta}{\omega^2\mu\varepsilon - \beta^2} \left(\frac{\partial}{r\partial\phi} E_z - \frac{\omega\mu}{\beta} \frac{\partial}{\partial r} H_z \right) \\ H_r &= \frac{-i\beta}{\omega^2\mu\varepsilon - \beta^2} \left(\frac{\partial}{\partial r} H_z - \frac{\omega\varepsilon}{\beta} \frac{\partial}{r\partial\phi} E_z \right) \\ H_\phi &= \frac{-i\beta}{\omega^2\mu\varepsilon - \beta^2} \left(\frac{\partial}{r\partial\phi} H_z - \frac{\omega\varepsilon}{\beta} \frac{\partial}{\partial r} E_z \right). \end{aligned} \quad (2.4)$$

The wave equation for the z -component is relatively simple. The field quantities vary as $E_j = \text{Re}[E_j^0 e^{i\omega t}]$ with $j \in \{r, \phi, z\}$ and the spatial variation of ε along the propagation axis is small, so the right hand side of equation (2.1) can be neglected:

$$(\nabla^2 + k^2) \begin{bmatrix} E_z \\ H_z \end{bmatrix} = 0, \quad (2.5)$$

where $k^2 = \omega^2 n^2 / c^2$ is the wave number and ∇^2 is the Laplace operator in cylindrical coordinates. The time evolution and axial dependence of the electric and magnetic field can be written as

$$\begin{bmatrix} \vec{E}(\vec{r}, t) \\ \vec{H}(\vec{r}, t) \end{bmatrix} = \begin{bmatrix} \vec{E}(r, \phi) \\ \vec{H}(r, \phi) \end{bmatrix} e^{i(\omega t - \beta z)}, \quad (2.6)$$

where β is the propagation constant which will play a central role in the description of the light. Using equation (2.6) the wave equation takes the form

$$\left(\frac{\partial^2}{\partial r^2} + \frac{1}{r} \frac{\partial}{\partial r} + \frac{1}{r^2} \frac{\partial^2}{\partial \phi^2} + (k^2 - \beta^2) \right) \begin{bmatrix} E_z \\ H_z \end{bmatrix} = 0. \quad (2.7)$$

With the ansatz

$$\begin{bmatrix} E_z \\ H_z \end{bmatrix} = \begin{bmatrix} \psi_1 \\ \psi_2 \end{bmatrix} e^{\pm i l \phi}, \quad l = 0, 1, 2, \dots \quad (2.8)$$

the wave equation then becomes the well known Bessel differential equation

$$\frac{\partial^2 \psi}{\partial r^2} + \frac{1}{r} \frac{\partial \psi}{\partial r} + \left(k^2 - \beta^2 - \frac{l^2}{r^2} \right) \psi = 0, \quad (2.9)$$

with $\psi = \psi_1, \psi_2$. The solutions to equation (2.9) are the Bessel functions of order l [24]. There are two sets of solutions, depending on whether $k^2 - \beta^2$ is positive or negative. For $k^2 - \beta^2 > 0$ the general solution to equation (2.9) is given by

$$\psi(r) = c_1 J_l(hr) + c_2 Y_l(hr), \quad c_1, c_2 \in \mathbb{C}, \quad (2.10)$$

where J_l and Y_l are the Bessel functions of first and second kind of order l and $h^2 = k^2 - \beta^2$ determining the argument of these functions. The second set of solutions to equation (2.9) is given for $k^2 - \beta^2 < 0$ by

$$\psi(r) = c_3 I_l(qr) + c_4 K_l(qr), \quad c_3, c_4 \in \mathbb{C}. \quad (2.11)$$

Here I_l and K_l are the modified Bessel functions of the first and second kind of order l [24] and $q^2 = \beta^2 - k^2$ determines their argument. The general form of the mentioned Bessel functions are shown in figures 2.2 and 2.3, respectively. The Bessel functions J_l and Y_l are oscillatory functions with Y_l showing a singularity for $r \rightarrow 0$. I_l is a strictly increasing function in r , whereas K_l is strictly decreasing in r .

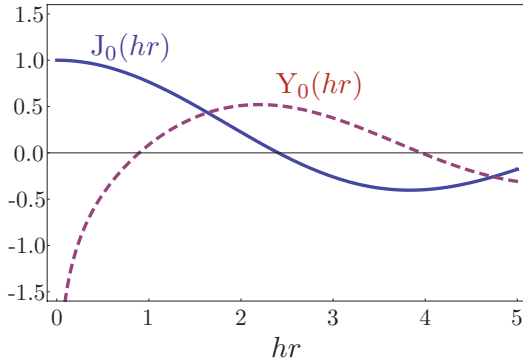


FIGURE 2.2: Plot of the Bessel functions of first and second kind, J_0 (blue solid line) and Y_0 (red dashed line)

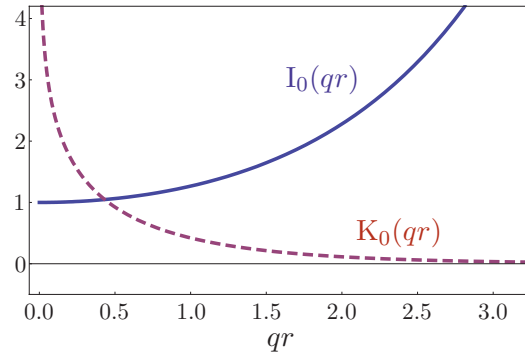


FIGURE 2.3: Plot of the modified Bessel functions of first and second kind, I_0 (blue solid line) and K_0 (red dashed line)

2.2 Propagation of light in a step-index circular waveguide

Now the effect of boundary conditions in the form of an optical waveguide on a propagating light field is discussed. Consider a step-index circular waveguide with a core of refractive index n_1 and radius a and a cladding of refractive index n_2 and radius b , as shown in figure 2.4. For a large radius b , the field on the outer cladding surface is vanishing. This condition is almost always fulfilled in any practical application.

In the core ($r < a$), the radial dependence of the field is given by equation (2.10). Since the Bessel function Y_l is singular at $r = 0$ (compare to figure 2.2), $c_2 = 0$ and the field distribution in the core is given by the Bessel function of first kind $J_l(hr)$:

$$\begin{aligned} E_z^\pm(\vec{r}, t) &= A J_l(hr) e^{i(\omega t \pm l\phi - \beta z)} \\ H_z^\pm(\vec{r}, t) &= B J_l(hr) e^{i(\omega t \pm l\phi - \beta z)}, \end{aligned} \quad (2.12)$$

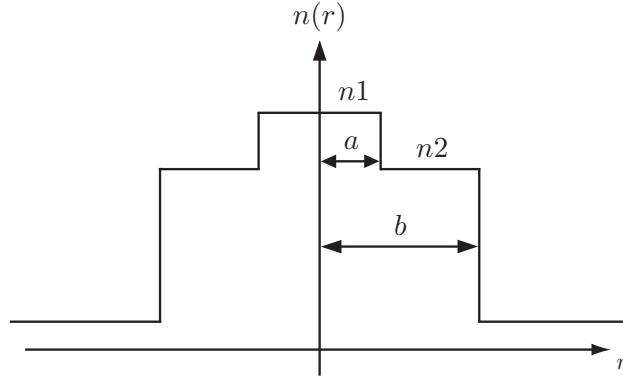


FIGURE 2.4: Schematic step-index fibre profile. Shown is the refractive index of the fibre over radial distance from the fibre center.

where A and B are normalisation constants. The parameter h is defined as

$$h^2 = n_1^2 k_0^2 - \beta^2, \quad (2.13)$$

with $k_0 = \omega/c_0$ the propagation constant in free space, where c_0 is the speed of light in vacuum. In the cladding region ($r > a$) the radial dependence of the field is given by equation (2.11). As the power density of a guided mode is restricted to the fibre, the field has to drop off for $r \rightarrow \infty$. From the form of the modified Bessel functions (figure 2.3), this requires $c_1 = 0$ in equation (2.11) and the field in the cladding shows an evanescent decay determined solely by $K_l(qr)$:

$$\begin{aligned} E_z^\pm(\vec{r}, t) &= CK_l(qr)e^{i(\omega t \pm l\phi - \beta z)} \\ H_z^\pm(\vec{r}, t) &= DK_l(qr)e^{i(\omega t \pm l\phi - \beta z)}, \end{aligned} \quad (2.14)$$

where C and D are again normalisation constants and q is defined as:

$$q^2 = \beta^2 - n_2^2 k_0^2. \quad (2.15)$$

From $h^2 > 0$ and $q^2 > 0$ follows $n_1 k_0 > \beta > n_2 k_0$. This is evident from the fact, that the guided light is at least partially confined inside the core with refractive index n_1 , so the propagation constant has to take values between $n_1 k_0$ and $n_2 k_0$. The “+” and “-” sign in equations (2.12) and (2.14) represents two degenerate circularly polarised states. The linear polarisation state for \vec{E} and \vec{H} can be created via superposition of the two states with circular polarisation. One example for the z -component of the linear polarisation state then reads:

$$\begin{aligned} E_z^{\text{lin}} &= \frac{1}{\sqrt{2}} (E_z^+ + E_z^-) \\ H_z^{\text{lin}} &= \frac{1}{\sqrt{2}} (H_z^+ + H_z^-) \end{aligned} \quad (2.16)$$

All field components in the core and cladding regions can now be expressed, using equations (2.4), (2.12) and (2.14). The field components inside the core ($r < a$) are then given

by:

$$\begin{aligned}
 E_r &= -\frac{i\beta}{h^2} \left(AhJ'_l(hr) + \frac{i\omega\mu l}{\beta r} BJ_l(hr) \right) e^{i(\omega t + l\phi - \beta z)} \\
 E_\phi &= -\frac{i\beta}{h^2} \left(\frac{il}{r} AJ_l(hr) - \frac{\omega\mu}{\beta} BhJ'_l(hr) \right) e^{i(\omega t + l\phi - \beta z)} \\
 E_z &= AJ_l(hr) e^{i(\omega t + l\phi - \beta z)} \\
 H_r &= -\frac{i\beta}{h^2} \left(BhJ'_l(hr) - \frac{i\omega\varepsilon_1 l}{\beta r} AJ_l(hr) \right) e^{i(\omega t + l\phi - \beta z)} \\
 H_\phi &= -\frac{i\beta}{h^2} \left(\frac{il}{r} BJ_l(hr) + \frac{\omega\varepsilon_1}{\beta} AhJ'_l(hr) \right) e^{i(\omega t + l\phi - \beta z)} \\
 H_z &= BJ_l(hr) e^{i(\omega t + l\phi - \beta z)},
 \end{aligned} \tag{2.17}$$

where $J'_l(hr) = dJ_l(hr)/d(hr)$ is the first derivative of the Bessel function J_l and $\varepsilon_1 = \varepsilon_0 n_1^2$. Analogously, the field components in the cladding ($r > a$) are:

$$\begin{aligned}
 E_r &= \frac{i\beta}{q^2} \left(CqK'_l(qr) + \frac{i\omega\mu l}{\beta r} DK_l(qr) \right) e^{i(\omega t + l\phi - \beta z)} \\
 E_\phi &= \frac{i\beta}{q^2} \left(\frac{il}{r} CK_l(qr) - \frac{\omega\mu}{\beta} DqK'_l(qr) \right) e^{i(\omega t + l\phi - \beta z)} \\
 E_z &= CK_l(qr) e^{i(\omega t + l\phi - \beta z)} \\
 H_r &= \frac{i\beta}{q^2} \left(DqK'_l(qr) - \frac{i\omega\varepsilon_2 l}{\beta r} CK_l(qr) \right) e^{i(\omega t + l\phi - \beta z)} \\
 H_\phi &= \frac{i\beta}{q^2} \left(\frac{il}{r} DK_l(qr) + \frac{\omega\varepsilon_2}{\beta} CqK'_l(qr) \right) e^{i(\omega t + l\phi - \beta z)} \\
 H_z &= DK_l(qr) e^{i(\omega t + l\phi - \beta z)},
 \end{aligned} \tag{2.18}$$

where $K'_l(qr) = dK_l(qr)/d(qr)$ is the first derivative of the Bessel function K_l and $\varepsilon_2 = \varepsilon_0 n_2^2$. To determine the propagation constant, the boundary conditions, that all field components parallel to the core-cladding boundary, E_ϕ , E_z , H_ϕ and H_z must be continuous at $r = a$ [25], have to be taken into account. Equations (2.17) and (2.18) yield:

$$\begin{aligned}
 AJ_l(ha) - CK_l(qa) &= 0 \\
 A \left(\frac{il}{h^2 a} J_l(ha) \right) + B \left(-\frac{\omega\mu}{h\beta} J'_l(ha) \right) + C \left(\frac{il}{q^2 a} K_l(qa) \right) + D \left(-\frac{\omega\mu}{q\beta} K'_l(qa) \right) &= 0 \\
 BJ_l(ha) - DK_l(qa) &= 0 \\
 A \left(\frac{\omega\varepsilon_1}{h\beta} J'_l(ha) \right) + B \left(\frac{il}{h^2 a} J_l(ha) \right) + C \left(\frac{\omega\varepsilon_2}{q\beta} K'_l(qa) \right) + D \left(\frac{il}{q^2 a} K_l(qa) \right) &= 0.
 \end{aligned} \tag{2.19}$$

This system of equations can be solved for nontrivial values of A, B, C and D using the coefficient matrix method [26]. The arising condition reads

$$\begin{aligned} & \left(\frac{J'_l(ha)}{haJ_l(ha)} + \frac{K'_l(qa)}{qaK_l(qa)} \right) \left(\frac{n_1^2 J'_l(ha)}{haJ_l(ha)} + \frac{n_2^2 K'_l(qa)}{qaK_l(qa)} \right) \\ &= l^2 \left[\left(\frac{1}{qa} \right)^2 + \left(\frac{1}{ha} \right)^2 \right]^2 \left(\frac{\beta}{k_0} \right)^2. \end{aligned} \quad (2.20)$$

Solving for β at a given l and ω , the normalisation constants that determine the strength of the field components are obtained

$$\begin{aligned} \frac{C}{A} &= \frac{J_l(ha)}{K_l(qa)} \\ \frac{B}{A} &= \frac{i\beta l}{\omega\mu} \left(\frac{1}{q^2 a^2} + \frac{1}{h^2 a^2} \right) \left(\frac{J'_l(ha)}{haJ_l(ha)} + \frac{K'_l(qa)}{aqK_l(qa)} \right)^{-1} \\ \frac{D}{A} &= \frac{J_l(ha)}{K_l(qa)} \frac{B}{A}. \end{aligned} \quad (2.21)$$

Equation (2.20) describes the propagation of light in a step index fibre. In the following, it is shown, that this equation can be separated into two classes and how the propagation constants β for these classes can be obtained.

2.3 Propagating modes

Equation (2.20) expresses the boundary conditions of the confinement created by the fibre, that a light field has to meet in order to propagate. These light fields are called modes of the fibre. This chapter examines the boundary conditions given by the fibre and describes the determination of the arising modes and their propagation constants β from the results of section 2.2.

Equation (2.20) is quadratic in $J'_l(ha)/(haJ_l(ha))$, so solving for this quantity gives two classes of solutions:

$$\begin{aligned} \frac{J'_l(ha)}{haJ_l(ha)} &= - \left(\frac{n_1^2 + n_2^2}{2n_1^2} \right) \frac{K'_l}{qaK_l} \\ &\pm \sqrt{\left(\frac{n_1^2 - n_2^2}{2n_1^2} \right)^2 \left(\frac{K'_l}{qaK_l} \right)^2 + \frac{l^2}{n_1^2} \left(\frac{\beta}{k_0} \right)^2 \left(\frac{1}{q^2 a^2} + \frac{1}{h^2 a^2} \right)^2}, \end{aligned} \quad (2.22)$$

where $K'_l = K'_l(qa)$ and $K_l = K_l(qa)$. Using the Bessel function relations

$$\begin{aligned} J'_l(x) &= -J_{l+1}(x) + \frac{l}{x} J_l(x) \\ J'_l(x) &= J_{l-1}(x) - \frac{l}{x} J_l(x), \end{aligned} \quad (2.23)$$

equation (2.22) separates into two sets of solutions, which are conventionally named EH modes [22]:

$$\frac{J_{l+1}(ha)}{haJ_l(ha)} = \frac{n_1^2 + n_2^2}{2n_1^2} \frac{K'_l(qa)}{qaK_l(qa)} + \left(\frac{l}{(ha)^2} - R \right) \quad (2.24)$$

and HE modes

$$\frac{J_{l-1}(ha)}{haJ_l(ha)} = - \left(\frac{n_1^2 + n_2^2}{2n_1^2} \right) \frac{K'_l(qa)}{qaK_l(qa)} + \left(\frac{l}{(ha)^2} - R \right), \quad (2.25)$$

where

$$R = \sqrt{\left(\frac{n_1^2 - n_2^2}{2n_1^2} \right)^2 \left(\frac{K'_l(qa)}{qaK_l(qa)} \right)^2 + \frac{l^2}{n_1^2} \left(\frac{\beta}{k_0} \right)^2 \left(\frac{1}{q^2 a^2} + \frac{1}{h^2 a^2} \right)^2}. \quad (2.26)$$

The designation EH and HE indicates whether the z -component of the electric or the magnetic field is larger. For the EH mode E_z contributes more to the mode than H_z . For the HE mode the opposite holds true. Equations (2.24) and (2.25) are transcendental functions in ha and can only be solved graphically by plotting each side as a function of ha using

$$(qa)^2 = a^2(n_1^2 - n_2^2)k_0^2 - (ha)^2, \quad (2.27)$$

given by equations (2.15) and (2.13). The parameter V , defined as

$$V = k_0 a \sqrt{n_1^2 - n_2^2} \quad (2.28)$$

determines how many modes can propagate in a fibre as a function of fibre radius a and the laser wavelength $\lambda = 2\pi/k_0$.

For the case of $l = 0$ the characteristic equation for the EH modes, equation (2.24) becomes

$$\frac{J_1(ha)}{haJ_0(ha)} = - \frac{K_1(qa)}{qaK_0(qa)}, \quad (2.29)$$

where the relation $K'_0 = -K_1$ has been used. Entering this result in equations (2.21) yields $A = C = 0$. This means that the only non-vanishing field components in equations (2.17) and (2.18) are H_r, H_z and E_ϕ . The modes are thus named transversal electric modes (TE). For $l=0$ the characteristic equation for the HE modes (equation (2.25)) yields

$$\frac{J_1(ha)}{haJ_0(ha)} = - \frac{n_2^2}{n_1^2} \frac{K_1(qa)}{qaK_0(qa)}, \quad (2.30)$$

with $J_{-1}(x) = -J_1(x)$. According to equation (2.21) the components B and D vanish and the only remaining field components are E_r, E_z and H_ϕ . These modes are therefore called transversal magnetic (TM) modes.

The graphical solutions of equations (2.29) and (2.30) are shown in figure 2.5. Here, the right hand side of equations (2.29) and (2.30) is shown together with the left hand side. Each intersection corresponds to a transversal fibre mode with a propagation constant resulting from ha . The modes are labelled TM_{0m} and TE_{0m} , respectively, where m denotes the different solutions of the modes. Note that the right hand side has a singularity at $ha = V = k_0 a \sqrt{n_1^2 - n_2^2} = 7.8$. For values of ha greater than V , no more intersections can be found, therefore the number of modes that can propagate through the fibre is determined by the V parameter. Using the replacement in equation (2.27), only the right hand sides of the equations (2.29) and (2.30) depends on the V parameter. Thus, when increasing the V parameter, the singularity is moved to the right. As a result, more intersections between the curves occur, meaning that more modes can propagate in the fibre. As $V \propto a$, the number of modes for a light field of a given wavelength λ can be chosen by selecting a

fibre of appropriate radius a . From the value of $(ha)_{\text{int}}$, where both curves intersect, the propagation constant β of the mode can be derived via

$$\beta = \sqrt{n_1^2 k_0^2 - \frac{(ha)_{\text{int}}}{a}}, \quad (2.31)$$

as follows from the definition of the parameter h . Single mode fibres operate in the regime,

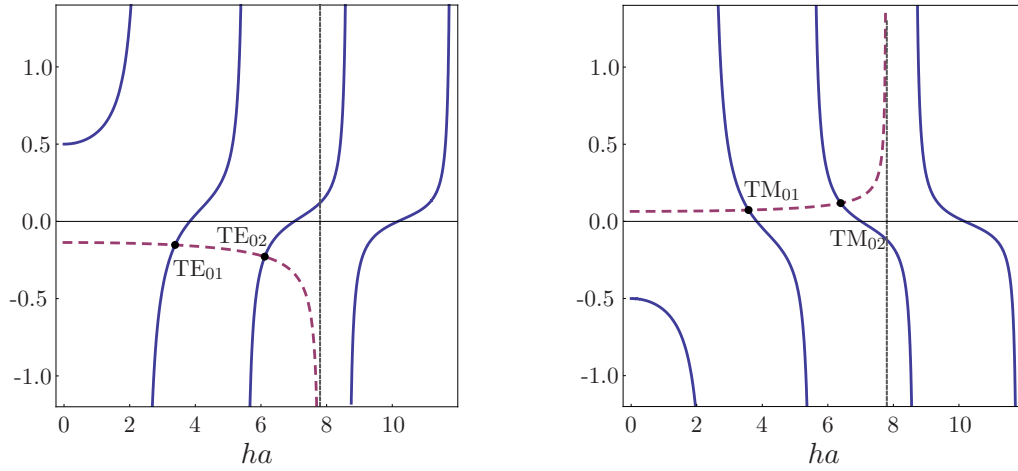


FIGURE 2.5: Plot of the right hand side (red, dashed) and left hand side (blue, solid) of equations (2.29)(left) and (2.30)(right) over the Bessel function argument ha . The dashed grey line marks the parameter $V = 7.8$. The intersections are the TE_{0m} and TM_{0m} modes, respectively.

where the V parameter is so small, that only the fundamental HE_{11} mode propagates. The single mode condition reads $V < 2.4$. If V is increased, more modes can be guided in the fibre, as is displayed in figure 2.6. In order to propagate through the fibre the normalised propagation constant β/k_0 must lie between the refractive indices of the cladding n_2 and the core n_1 .

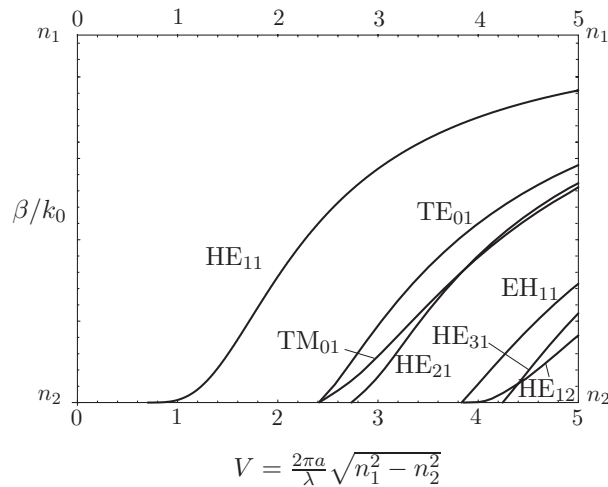


FIGURE 2.6: Normalised propagation constant β/k_0 over the V parameter for the first seven modes in a fibre.

Now the case of $l = 1$ is considered. The analogue treatment of equations (2.24) and (2.25) as for $l = 0$ results in the graphs shown in figure 2.7. In this case all six possible field components are non-vanishing. Hence these modes are neither transversal electric nor transversal magnetic but hybrid EH and HE modes. They are labelled in the same way as described earlier for the TM and TE modes as HE_{lm} and EH_{lm} with $l = 1$, where again, m denotes the different solutions of the modes. Note, that the mode HE_{11} has no cutoff value regardless of which V parameter is chosen. It is therefore called the *fundamental mode*.

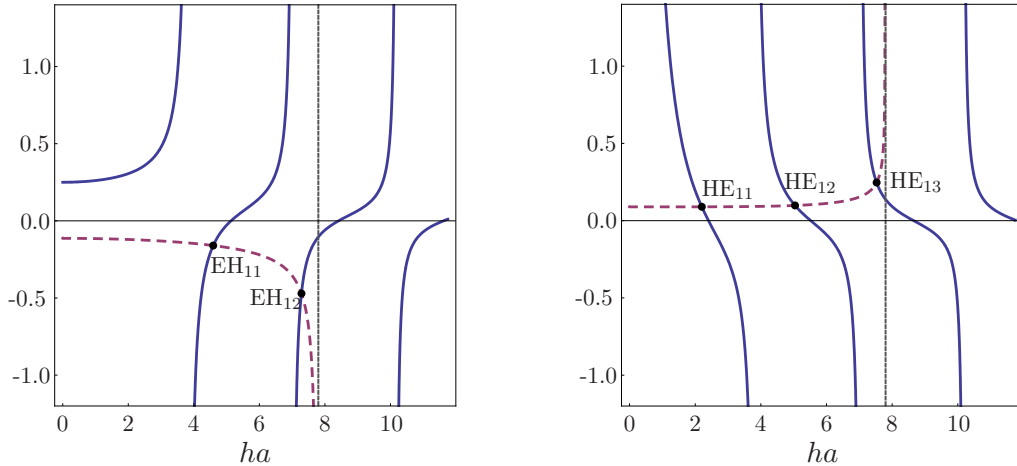


FIGURE 2.7: Plot of the right hand side (red, dashed) and left hand side (blue, solid) of equations (2.24)(left) and (2.25)(right) over the Bessel function argument ha . The dashed grey line marks the parameter $V = 7.8$. The intersections are the EH_{1m} and HE_{1m} modes, respectively.

2.4 Mode propagation in ultra thin optical fibres

Now the propagation of modes in a fibre with a diameter smaller than the wavelength of the guided light is presented. Such fibres can be fabricated by stretching standard fibres until the core becomes too thin to guide the light and it is therefore guided in the cladding. This transition takes place for a fibre diameter of less than $7 \mu\text{m}$ [27]. In such a configuration the surrounding medium plays the role of the cladding in an untapered fibre, creating a step-wise decrease of the refractive index at the boundary. As a consequence the evanescent field now becomes accessible, because it projects over the limits of the fibre, as is shown in figure 2.8. The equations derived in sections 2.2 and 2.3 remain valid, taking into account the changed refractive indices.

Introducing more than one mode into the fibre leads to modal dispersion that is based on the difference in the propagation constants of the travelling mode. This effect is usually undesirable, for example for telecommunication purposes, as it broadens a communication signal and thus lowers the information transfer efficiency. However, throughout this thesis, the effect of mode interference in a fibre and the resulting evanescent field is examined, so more modes than the fundamental mode must be considered. On the other hand, too many propagating modes, and therefore too many propagation constants would complicate

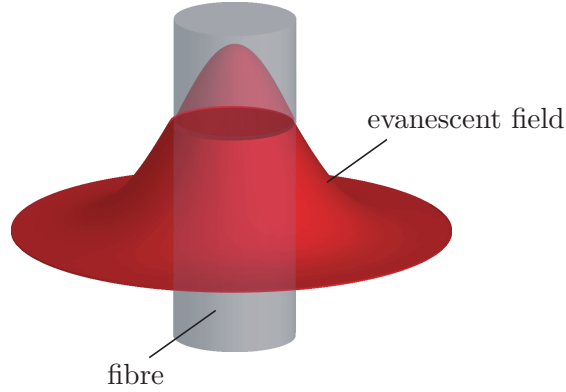


FIGURE 2.8: Schematic of the fundamental HE_{11} mode in a subwavelength diameter fibre and the quasi-exponentially decaying evanescent field.

matters theoretically and experimentally. The simplest case is, when exactly two modes are guided by the fibre. Now consider figure 2.6 for a fixed wavelength λ : The higher order modes TE_{01} , TM_{01} and HE_{21} are introduced into the fibre almost at the same fibre diameter, making it very difficult to separate them experimentally. Furthermore, the fibre radius should be as small as possible to maximise the evanescent field. For these reasons, only the fundamental mode HE_{11} and the three higher order modes TE_{01} , TM_{01} and HE_{21} are considered. This section will examine the properties of these four modes.

2.4.1 The fundamental HE_{11} mode with quasi-linear polarisation

We will start our examination of the mode characteristics with the fundamental HE_{11} mode in a *quasi-linear* polarisation state [28]. The field components E_r^{lin} and E_ϕ^{lin} are constructed in the same manner as E_z^{lin} (equation (2.16))

$$\begin{aligned} E_r^{\text{lin}} &= \frac{1}{\sqrt{2}} (E_r^+ + E_r^-) \\ E_\phi^{\text{lin}} &= \frac{1}{\sqrt{2}} (E_\phi^+ + E_\phi^-) \end{aligned} \tag{2.32}$$

and transformed into cartesian coordinates

$$\begin{aligned} E_x^{\text{lin}} &= E_r^{\text{lin}} \cos(\phi) - E_\phi^{\text{lin}} \sin(\phi) \\ E_y^{\text{lin}} &= E_r^{\text{lin}} \sin(\phi) + E_\phi^{\text{lin}} \cos(\phi) \\ E_z^{\text{lin}} &= E_z^{\text{lin}} \end{aligned} \tag{2.33}$$

Henceforth, the superscript “lin” will be omitted. Using equation (2.33), the field equations for the electric field in the quasi-linearly polarised HE_{11} for the propagation in the core

($r < a$) are given by:

$$\begin{aligned}
 E_x(r, \phi, z, t) &= -iA_{11} \frac{\beta_{11}}{2h_{11}} [(1 - s_{11})J_0(h_{11}r) \cos(\varphi_0) - \\
 &\quad - (1 + s_{11})J_2(h_{11}r) \cos(2\phi - \varphi_0)] e^{i(\omega t - \beta_{11}z)} \\
 E_y(r, \phi, z, t) &= -iA_{11} \frac{\beta_{11}}{2h_{11}} [(1 - s_{11})J_0(h_{11}r) \sin(\varphi_0) - \\
 &\quad - (1 + s_{11})J_2(h_{11}r) \sin(2\phi - \varphi_0)] e^{i(\omega t - \beta_{11}z)} \\
 E_z(r, \phi, z, t) &= A_{11} J_1(h_{11}r) \cos(\phi - \varphi_0) e^{i(\omega t - \beta_{11}z)}
 \end{aligned} \tag{2.34}$$

Analogously, the electric field components for the cladding ($r > a$) are

$$\begin{aligned}
 E_x(r, \phi, z, t) &= A_{11} \frac{\beta_{11}}{2q_{11}} \frac{J_1(h_{11}a)}{K_1(q_{11}a)} [(1 - s_{11})K_0(q_{11}r) \cos(\varphi_0) + \\
 &\quad + (1 + s_{11})K_2(q_{11}r) \cos(2\phi - \varphi_0)] e^{i(\omega t - \beta_{11}z)} \\
 E_y(r, \phi, z, t) &= A_{11} \frac{\beta_{11}}{2q_{11}} \frac{J_1(h_{11}a)}{K_1(q_{11}a)} [(1 - s_{11})K_0(q_{11}r) \sin(\varphi_0) + \\
 &\quad + (1 + s_{11})K_2(q_{11}r) \sin(2\phi - \varphi_0)] e^{i(\omega t - \beta_{11}z)} \\
 E_z(r, \phi, z, t) &= iA_{11} \frac{J_1(h_{11}a)}{K_1(q_{11}a)} K_1(q_{11}r) \cos(\phi - \varphi_0) e^{i(\omega t - \beta_{11}z)},
 \end{aligned} \tag{2.35}$$

where

$$s_{11} = \left[\frac{1}{(h_{11}a)^2} + \frac{1}{(q_{11}a)^2} \right] \left[\frac{J_1'(h_{11}a)}{h_{11}a J_1(h_{11}a)} + \frac{K_1'(q_{11}a)}{q_{11}a K_1(q_{11}a)} \right]^{-1} \tag{2.36}$$

$$h_{11} = \sqrt{k_0^2 n_1^2 - \beta_{11}^2} \tag{2.37}$$

$$q_{11} = \sqrt{\beta_{11}^2 - k_0^2 n_2^2}. \tag{2.38}$$

The angle φ_0 gives the polarisation direction of the transverse electric field $\vec{E}_\perp = (E_x, E_y)$, with $\varphi_0 = 0$ leading to a polarisation along the x -axis and $\varphi_0 = \pi/2$ to a polarisation along the y -axis. Note that the designation ‘‘quasi-linear’’ polarisation stems from the fact that the z -component has a $\pi/2$ phase shift to the perpendicular components. This results in elliptical polarisation, where E_z is not zero. Figure 2.9 shows the electric field components $\vec{E}_\perp = (E_x, E_y)$ of the HE₁₁ mode with x -polarisation ($\varphi_0 = 0$) for $t = 0$ and $z = 0$. The polarisation direction is the same over the entire field.

The field intensity distribution of the HE₁₁ mode can now be calculated using

$$I = \frac{1}{2} \varepsilon_0 c_0 |\vec{E}|^2, \tag{2.39}$$

where ε_0 is the electric permittivity for vacuum. The equation

$$|\vec{E}|^2 = |E_x|^2 + |E_y|^2 + |E_z|^2 \tag{2.40}$$

in combination with equations (2.34) and (2.35) yields for the electric field in the core ($r < a$):

$$\begin{aligned}
 |E|^2 &= g_{in} (J_0^2(hr) + uJ_1^2(hr) + fJ_2^2(hr) \\
 &\quad + [uJ_1^2(hr) - f_p J_0(hr) J_2(hr)] \cos(2(\phi - \varphi_0)))
 \end{aligned} \tag{2.41}$$

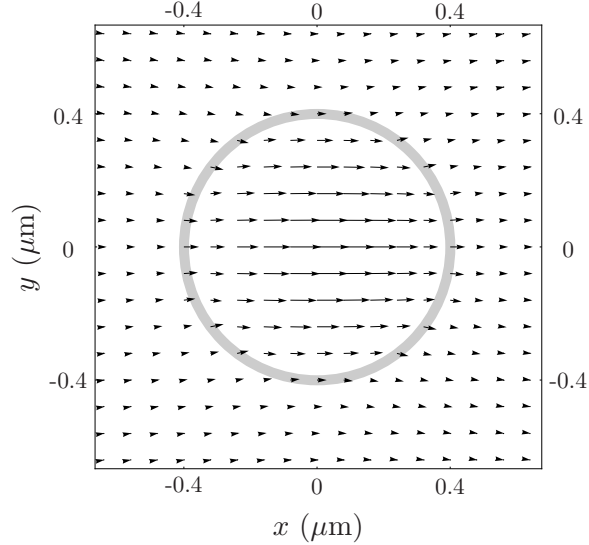


FIGURE 2.9: Field plot of the electric field component perpendicular to the fibre axis $\vec{E}_\perp = (E_x, E_y)$ for the HE_{11} mode at $t = 0$, $z = 0$ and for $\varphi_0 = 0$ (see equations (2.34) and (2.35)). The fibre is indicated by the grey circle. The following parameters have been used: $a = 400$ nm, $n_1 = 1.452$, $n_2 = 1$, and $\lambda = 850$ nm.

and for the cladding ($r > a$):

$$|E|^2 = g_{out} (K_0^2(qr) + wK_1^2(qr) + fK_2^2(qr) + [wK_1^2(qr) + f_p K_0(qr)K_2(qr)] \cos(2(\phi - \varphi_0))), \quad (2.42)$$

where

$$\begin{aligned} u &= \frac{2h^2}{\beta(1-s)^2}, & w &= \frac{2q^2}{\beta^2(1-s)^2} \\ f &= \frac{(1+s)^2}{(1-s)^2}, & f_p &= \frac{2(1+s)}{(1-s)} \\ g_{in} &= \frac{|A|^2}{2u}, & g_{out} &= \frac{|A|^2 J_1^2(ha)}{2wK_1^2(qa)}. \end{aligned} \quad (2.43)$$

The intensity distribution according to equation (2.39) on the inside and the outside of a fibre for a linearly polarised HE_{11} mode with polarisation in x -direction ($\varphi_0 = 0$) in a vacuum-clad fibre is shown in figure 2.10. The electric field components at the border of two media with different refractive indices are discontinuous when perpendicular to the fibre surface and continuous when parallel to the fibre surface [29]. The density plot of the intensity distribution, figure 2.11 displays the fundamental mode's bell-shaped intensity profile.

As can be seen in figure 2.9, the electric field for the linearly polarised HE_{11} is perpendicular to the fibre surface for $\phi = 0$ and $\phi = \pi$ and parallel for $\phi = \pi/2$ and $\phi = 3\pi/2$. The corresponding intensity distributions are shown in figures 2.12 and 2.13 and display the discontinuity of the intensity at the transition from the silica fibre with $n_1 = 1.452$ to vacuum with $n_2 = 1$ in the first and the continuity in the latter case. The fibre surface is indicated by the dashed grey line. The evanescent field decays quasi-exponentially with a decay constant of $\Lambda_{11} = 1/q_{11} = 164$ nm for these parameters.

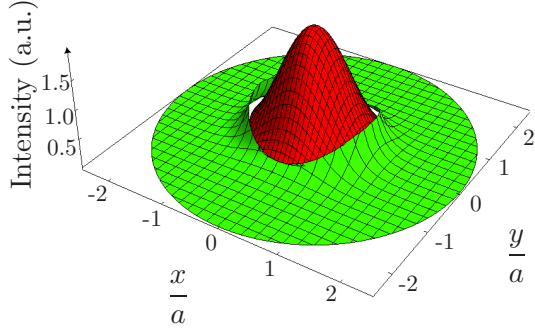


FIGURE 2.10: Intensity distribution of the HE_{11} mode inside (red) and outside (green) of a 400 nm fibre and a wavelength $\lambda = 850$ nm. The intensity shows an azimuthal dependence.

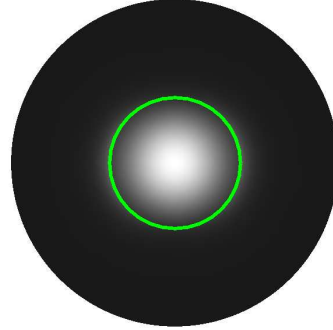


FIGURE 2.11: Intensity distribution of the HE_{11} mode. Bright spots indicate regions of high intensity. The green circle indicates the fibre surface. The fibre parameters are identical to figure 2.10.

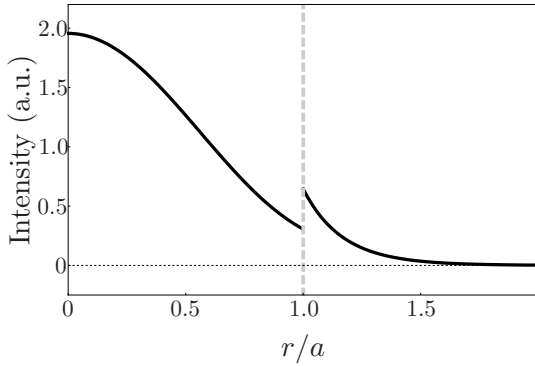


FIGURE 2.12: Radial intensity distribution of the HE_{11} mode at $\phi = 0$. At the fibre-vacuum transition (dashed grey line), the electric field is perpendicular to the surface (compare to figure 2.9), so the intensity shows a discontinuity.

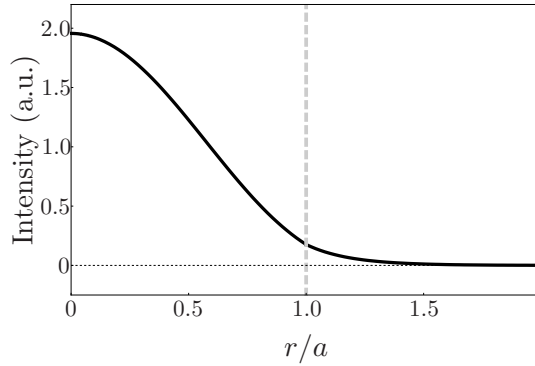


FIGURE 2.13: Radial intensity distribution of the HE_{11} mode at $\phi = \pi/2$. At the fibre-vacuum transition (dashed grey line), the electric field is parallel to the surface (compare to figure 2.9), so the intensity is continuous.

2.4.2 The HE₂₁ mode with quasi-linear polarisation

The next hybrid mode propagating in the fibre is the HE₂₁, whose properties will be discussed in this section. Analogue to section 2.4.1 the field equations for the linearly polarised HE₂₁ mode can be obtained for propagation in the core ($r < a$) as [22]:

$$\begin{aligned}
E_x(r, \phi, z, t) &= iA_{21} \frac{\beta_{21}}{2h_{21}} [(1 - 2s_{21})J_1(h_{21}r) \cos(\phi + 2\varphi_0) - \\
&\quad - (1 + 2s_{21})J_3(h_{21}r) \cos(3\phi + 2\varphi_0)] \exp[i(\omega t - \beta_{21}z)] \\
E_y(r, \phi, z, t) &= -iA_{21} \frac{\beta_{21}}{2h_{21}} [(1 - 2s_{21})J_1(h_{21}r) \sin(\phi + 2\varphi_0) + \\
&\quad + (1 + 2s_{21})J_3(h_{21}r) \sin(3\phi + 2\varphi_0)] \exp[i(\omega t - \beta_{21}z)] \\
E_z(r, \phi, z, t) &= -A_{21}J_2(h_{21}r) \cos(2(\phi + \varphi_0)) \exp[i(\omega t - \beta_{21}z)]
\end{aligned} \tag{2.44}$$

and for propagation in the cladding ($r > a$):

$$\begin{aligned}
E_x(r, \phi, z, t) &= -A_{21} \frac{\beta_{21}}{2q_{21}} \frac{J_2(h_{21}a)}{K_2(q_{21}a)} [(1 - 2s_{21})K_1(q_{21}r) \cos(\phi + 2\varphi_0) + \\
&\quad + (1 + 2s_{21})K_3(q_{21}r) \cos(3\phi + 2\varphi_0)] \exp[i(\omega t - \beta_{21}z)] \\
E_y(r, \phi, z, t) &= A_{21} \frac{\beta_{21}}{2q_{21}} \frac{J_2(h_{21}a)}{K_2(q_{21}a)} [(1 - 2s_{21})K_1(q_{21}r) \sin(\phi + 2\varphi_0) - \\
&\quad - (1 + 2s_{21})K_3(q_{21}r) \sin(3\phi + 2\varphi_0)] \exp[i(\omega t - \beta_{21}z)] \\
E_z(r, \phi, z, t) &= -iA_{21} \frac{J_2(h_{21}a)}{K_2(q_{21}a)} K_2(q_{21}r) \cos(2(\phi + \varphi_0)) \exp[i(\omega t - \beta_{21}z)]
\end{aligned} \tag{2.45}$$

where,

$$s_{21} = \left[\frac{1}{(h_{21}a)^2} + \frac{1}{(q_{21}a)^2} \right] \left[\frac{J_2'(h_{21}a)}{h_{21}aJ_2(h_{21}a)} + \frac{K_2'(q_{21}a)}{q_{21}aK_2(q_{21}a)} \right]^{-1} \tag{2.46}$$

$$h_{21} = \sqrt{k_0^2 n_1^2 - \beta_{21}^2} \tag{2.47}$$

$$q_{21} = \sqrt{\beta_{21}^2 - k_0^2 n_2^2} \tag{2.48}$$

Again, φ_0 gives the polarisation direction of the transverse electric field $\vec{E}_\perp = (E_x, E_y)$, with $\varphi_0 = 0$ and $\varphi_0 = \pi/4$ resulting in two orthogonal polarisation states. The electric field distribution for $\vec{E}_\perp = (E_x, E_y)$ of the linearly polarised HE₂₁ mode with $\varphi_0 = 0$ for $t = 0$ and $z = 0$ is displayed in figure 2.14. Here, due to the local dependence of the field vectors, there are four locations each for the field vectors perpendicular and parallel to the surface. This defines the appearance of the intensity distribution of the field.

With the electric field components the intensity distribution for the linearly polarised HE₂₁ mode in a vacuum-clad fibre can be calculated. The result is shown for a polarisation parameter $\varphi = 0$ in figure 2.15. As with the HE₁₁ mode, one finds a strong azimuthal dependence of the intensity due to the discontinuity of the electric field components perpendicular to the fibre surface (compare to equation 2.39). In contrast to the HE₁₁ mode, the HE₂₁ mode has a donut-shaped intensity profile (see figure 2.16).

Figures 2.17 and 2.18 show the intensity profile for the HE₂₁ mode, where the electric field is parallel to the fibre surface ($\phi = \pi/4$) or perpendicular ($\phi = 0$) respectively (compare to figure 2.14). Note that in the first case the transition of the intensity is continuous at $r = a$ and discontinuous in the second. The fibre surface is indicated by the dashed grey line. The evanescent field drops off with a decay constant of $\Lambda_{21} = 1/q_{21} = 420$ nm for these parameters.

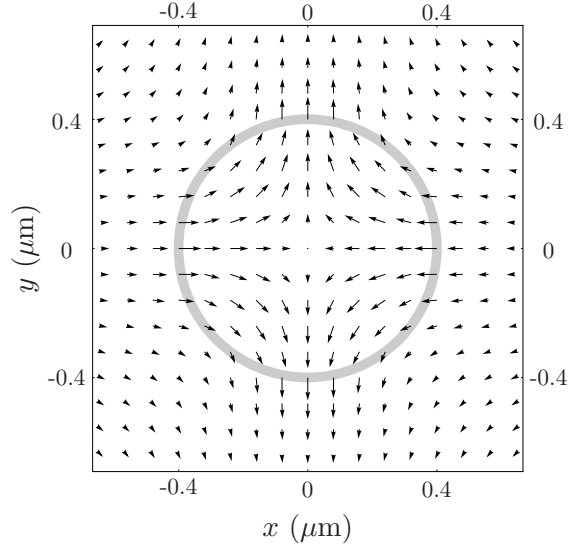


FIGURE 2.14: Field plot of the electric field component perpendicular to the fibre axis $\vec{E}_\perp = (E_x, E_y)$ for the HE_{21} mode at $t = 0$, $z = 0$ and for $\varphi_0 = 0$ (see equations (2.44) and (2.45)). The fibre is indicated by the grey circle. The parameters are identical to figure 2.9.

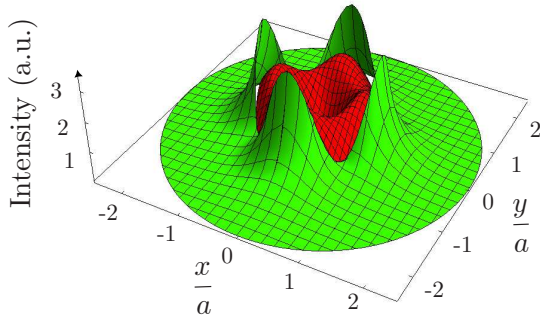


FIGURE 2.15: Intensity distribution of the HE_{21} mode inside (red) and outside (green) of a 400 nm fibre and a wavelength $\lambda = 850$ nm. The intensity shows an azimuthal dependence due to the different behaviour of the electric field components perpendicular and parallel to the fibre surface.

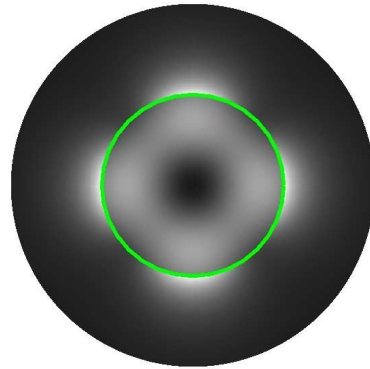


FIGURE 2.16: Intensity distribution of the HE_{21} mode. The green circle indicates the fibre surface. The fibre parameters are identical to figure 2.15.

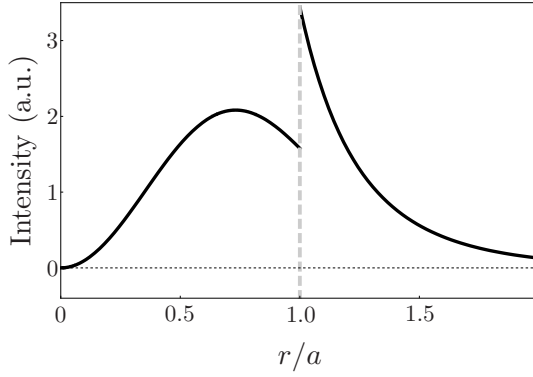


FIGURE 2.17: Radial intensity distribution of the HE_{21} mode in the x -direction. At the fibre-vacuum transition (dashed grey line), the electric field is perpendicular to the surface (compare to figure 2.14), so the intensity shows a discontinuity.

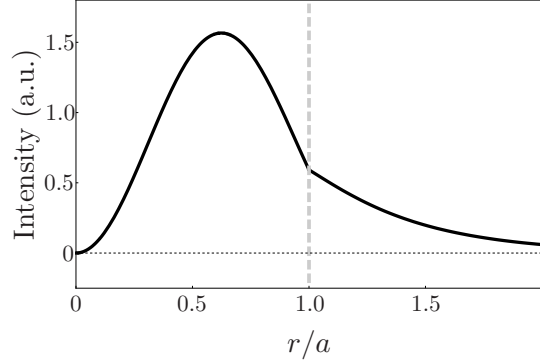


FIGURE 2.18: Radial intensity distribution of the HE_{21} mode in the y -direction. At the fibre-vacuum transition (dashed grey line), the electric field is parallel to the surface (compare to figure 2.14), so the intensity is continuous.

2.4.3 The TE_{01} mode

The first higher order mode that can propagate in a fibre after the fundamental HE_{11} is the TE_{01} . This section will discuss the properties of this mode. As discussed earlier, the radial and axial components of the electric field vanish. The field equations for the TE_{01} mode are thus given by [22] for the core ($r < a$) as

$$\begin{aligned} E_\phi(r, \phi, z, t) &= -\frac{i\omega\mu}{h_{01}} B_{01} J_1(h_{01}r) \exp[i(\omega t - \beta_{01}z)] \\ E_z(r, \phi, z, t) &= E_r(r, \phi, z, t) = 0 \end{aligned} \quad (2.49)$$

and for the cladding ($r > a$)

$$\begin{aligned} E_\phi(r, \phi, z, t) &= \frac{\omega\mu}{q_{01}} \frac{J_0(h_{01}a)}{K_0(q_{01}a)} B_{01} K_1(q_{01}r) \exp[i(\omega t - \beta_{01}z)] \\ E_z(r, \phi, z, t) &= E_r(r, \phi, z, t) = 0, \end{aligned} \quad (2.50)$$

where

$$h_{01} = \sqrt{k_0^2 n_1^2 - \beta_{01}^2} \quad (2.51)$$

$$q_{01} = \sqrt{\beta_{01}^2 - k_0^2 n_2^2}. \quad (2.52)$$

Figure 2.19 shows the electric field $\vec{E} = (E_x, E_y, 0)$ of the TE_{01} mode for $t = 0$ and $z = 0$. The directions of the field vectors depend on the azimuthal angle such that the field vectors on the fibre surface are always parallel to the border. Since the radial and axial components of the electric field of the TE_{01} mode vanish, the mode is linearly polarised. The intensity distribution inside and outside the fibre for a TE_{01} mode in a vacuum-clad fibre is shown in figure 2.20. The intensity forms a donut-shaped pattern, as can be seen

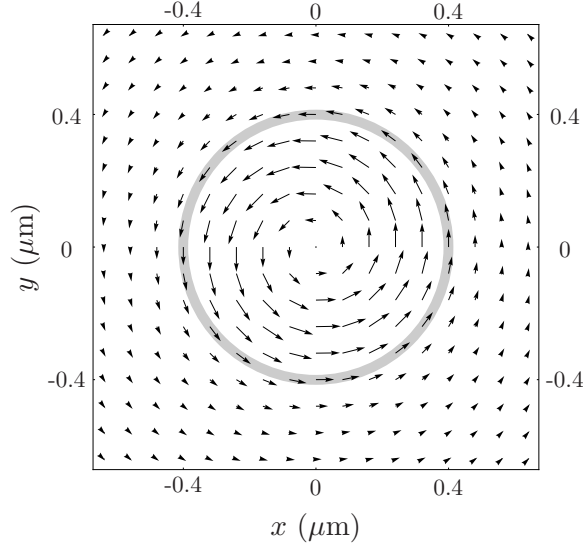


FIGURE 2.19: Field plot of the electric field \vec{E} for the TE_{01} mode at $t=0$ and $z=0$ (see equations (2.49) and (2.50)). The fibre is indicated by the grey circle. The parameters are identical to figure 2.9.

in figure 2.21. The field components of the TE_{01} mode are parallel to the fibre surface at any position, therefore they are all continuous at the fibre-vacuum boundary, so there is no azimuthal dependency of the intensity (compare to equation 2.39). Figure 2.22 shows the intensity profile for the TE_{01} mode for any azimuthal angle ϕ . The evanescent field decays quasi-exponentially with a decay constant of $\Lambda_{01} = 1/q_{01} = 277$ nm for these parameters.

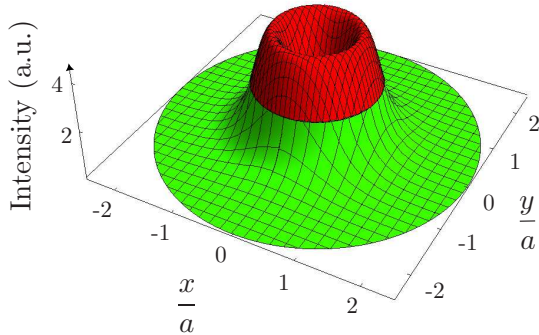


FIGURE 2.20: Intensity distribution of the TE_{01} mode inside (red) and outside (green) of a 400 nm fibre and a wavelength $\lambda=850$ nm.

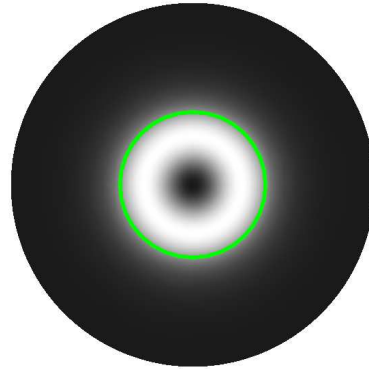


FIGURE 2.21: Intensity distribution of the TE_{01} mode. The green circle indicates the fibre surface. The fibre parameters are identical to figure 2.20.

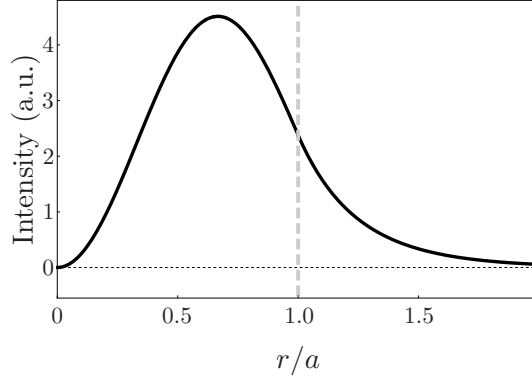


FIGURE 2.22: Radial intensity distribution of the TE_{01} mode. At the fibre-vacuum transition (dashed grey line), the electric field is parallel to the surface (compare to figure 2.19), so the intensity is continuous for all angles.

2.4.4 The TM_{01} mode

The discussion of the properties of the modes concludes with the orthogonal polarisation state to the TE_{01} mode, the TM_{01} mode. Here, the radial component of the electric field vanishes. The field equations for the TM_{01} mode are thus given by [22] for core propagation ($r < a$)

$$\begin{aligned} E_r(r, \phi, z, t) &= \frac{i\beta}{h_{TM}} A_{TM} J_1(h_{TM}r) \exp[i(\omega t - \beta_{TM}z)] \\ E_\phi(r, \phi, z, t) &= 0 \\ E_z(r, \phi, z, t) &= A_{TM} J_0(h_{TM}r) \exp[i(\omega t - \beta_{TM}z)] \end{aligned} \quad (2.53)$$

and for cladding propagation ($r > a$):

$$\begin{aligned} E_r(r, \phi, z, t) &= -\frac{i\beta}{q_{TM}} \frac{J_0(h_{TM}a)}{K_0(q_{TM}a)} A_{TM} K_1(q_{TM}r) \exp[i(\omega t - \beta_{TM}z)] \\ E_\phi(r, \phi, z, t) &= 0 \\ E_z(r, \phi, z, t) &= \frac{J_0(h_{TM}a)}{K_0(q_{TM}a)} A_{TM} K_0(q_{TM}r) \exp[i(\omega t - \beta_{TM}z)], \end{aligned} \quad (2.54)$$

where

$$h_{TM} = \sqrt{k_0^2 n_1^2 - \beta_{TM}^2} \quad (2.55)$$

$$q_{TM} = \sqrt{\beta_{TM}^2 - k_0^2 n_2^2}. \quad (2.56)$$

Figure 2.23 shows the electric field components $\vec{E}_\perp = (E_x, E_y)$ of the linearly polarised TM_{01} mode for $t = 0$ and $z = 0$. As the TM_{01} is in the orthogonal polarisation state to the TE_{01} , all the field vectors point in radial direction, so at the surface all field vectors are perpendicular to the border. Figure 2.24 shows the intensity distribution for the TM_{01} mode inside (dark, red) and outside (bright, green) an ultra thin fibre surrounded by vacuum. As in the HE_{11} mode, the intensity distribution exhibits a bell-shaped distribution (see figure 2.25). Figure 2.26 shows the intensity profile for the TM_{01}

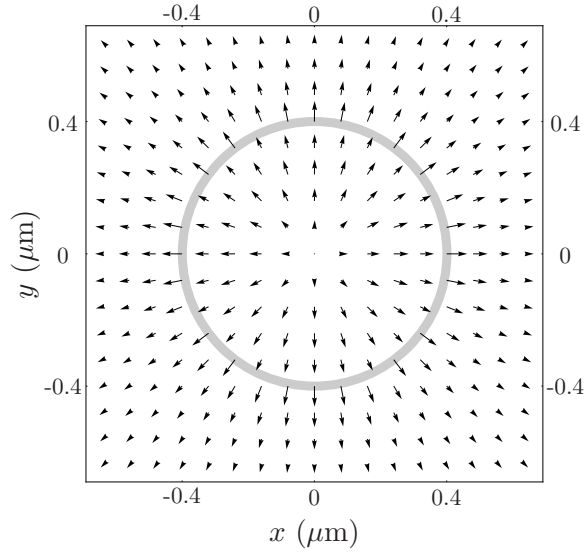


FIGURE 2.23: Field plot of the electric field component perpendicular to the fibre axis $\vec{E}_\perp = (E_x, E_y)$ for the TM_{01} mode at $t=0$ and $z=0$ (see equations (2.53) and (2.54)). The fibre is indicated by the grey circle. The parameters are identical to figure 2.9.

mode. As with the TE_{01} mode, there is no azimuthal dependency of the field. As the field is perpendicular to the vacuum-fibre border, the intensity is discontinuous at the transition from fibre to vacuum for any azimuthal angle ϕ . The evanescent field decays quasi-exponentially with a decay constant of $\Lambda_{\text{TM}} = 1/q_{\text{TM}} = 352 \text{ nm}$ for these parameters.

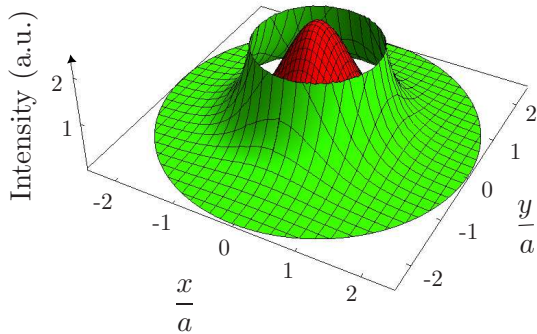


FIGURE 2.24: Intensity distribution of the TM_{01} mode inside (red) and outside (green) of a 400 nm fibre and a wavelength $\lambda=850 \text{ nm}$.

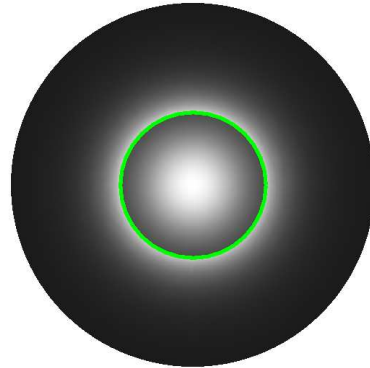


FIGURE 2.25: Intensity distribution of the TM_{01} mode. The green circle indicates the fibre surface. The fibre parameters are identical to figure 2.24.

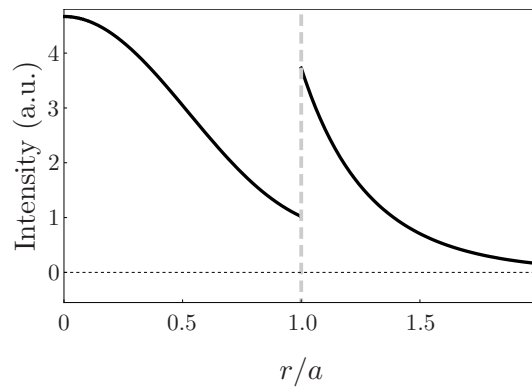


FIGURE 2.26: Radial intensity distribution of the TM_{01} mode. At the fibre-vacuum transition (dashed grey line), the electric field is perpendicular to the surface (compare to figure 2.23), so the intensity shows a discontinuity for any angle.

3 Mode Interference Traps

Ultra thin fibres and their evanescent fields discussed in chapter 2 have found various applications in optics, for example for coupling light in and out of microresonators [30] or for spectroscopy of atoms [31]. Furthermore, a trap for cold atoms using two laser wavelengths propagating in an ultra thin fibre has been proposed [18] and has just recently been experimentally realised in our research group [19].

The basic principle of this trap is to use the superposition of two light fields in an ultra thin single-mode fibre, one blue-detuned and the other red-detuned with respect to the excitation transition of the atoms used, in this case Caesium. When an atom is placed in the evanescent light fields, it experiences the optical dipole force [32]. Red-detuned light creates an attractive and blue-detuned light a repulsive potential. The decay length of the fields outside the fibre is wavelength dependent, with the red-detuned field (longer wavelength) decaying over a longer distance than the blue-detuned field (shorter wavelength). The superposition of a long ranged attractive potential and a short ranged repulsive potential can thus create a potential well, where laser cooled cesium atoms can be trapped [18]. The two-colour trap with linearly polarised light confines the atoms in azimuthal and radial direction. To confine the atoms in three dimensions the evanescent field distribution is modulated along the fibre by creating a standing wave pattern with the red-detuned light field. Furthermore, the two-color trap traps the atoms in regions with high red light intensity, which shifts the transition frequencies to those of the *dressed states* [32] due to the AC stark shift. As a consequence, for example in a spectroscopy experiment one would have to readjust the frequency of the probing light to match the transition frequency. Another experimentally challenging issue of the two-colour trap is the fact, that it is created by two large potentials, that partially compensate each other to form a relatively small well. Therefore, the trap depth is very susceptible to even small relative fluctuations in the power of one of the light fields: small relative fluctuations in the field power result in a large absolute fluctuation of the trap depth.

In this chapter, a similar idea is presented, that is, to create a potential minimum in the evanescent field of an ultra thin fibre, but with only a blue-detuned laser propagating in two different transversal modes (see chapter 2). If two modes co-propagate in the fibre, they form an interference pattern along the fibre because of their different propagation constants. As the main atom photon interaction here is the optical dipole force, which creates a repulsive potential for blue-detuned light, the atoms are confined in regions of low light intensity, that is, locations where the interference is maximally destructive. Furthermore, due to the different decay constants of the modes, one can displace the potential minimum in radial direction from the fibre by choosing the appropriate intensity distribution between the modes. Finally, by choosing the right polarisation direction, the azimuthal position of the trapping minima can be chosen. As a result, an array of traps, that confine the atoms in all three dimensions can be created.

The multimode trap circumvents the discussed drawbacks of the two-color trap. The interference of two co-propagating modes offers three dimensional confinement due to their

intensity and polarisation characteristics. Furthermore, as the atoms are caught in regions with zero or low light intensity, the transition frequency of the atoms are not shifted. It will also be shown that the multimode trap is robust against typical power fluctuations that occur in experimental setups.

This chapter will give three possible trap configurations which arise from the following combinations of the first four modes in the fibre: HE₁₁+TE₀₁, HE₁₁+HE₂₁ and HE₂₁+TE₀₁. Also, a short analysis of why the TM₀₁ cannot be used to create a good trap will be presented.

3.1 The optical potential

The discussion is started with a treatment of the optical potential experienced by an atom in the evanescent field around an TOF. There are two main contributions, that are considered here: The optical dipole force on the one hand, which creates either an attractive or repulsive potential, depending on the detuning of the guided light and the van der Waals surface potential on the other hand, that attracts atoms to the fibre surface.

First, the contribution of the optical dipole force to the potential is examined. For an atom in the ground state in an off-resonance field the optical potential is given by [25]:

$$U_{\text{opt}} = -\frac{1}{4}\alpha|E|^2, \quad (3.1)$$

Where $\alpha = \alpha(\omega)$ is the real part of the atomic polarisability at the optical frequency ω . Consider a multilevel atom with a number j of dipole transitions from the ground state to the excited states. Here, $\alpha(\omega)$ is given by

$$\alpha(\omega) = 2\pi\epsilon_0 c^3 \sum_j \frac{2J'+1}{2J+1} \frac{(\omega_j^2 - \omega^2)\Gamma_j/\omega_j^2}{(\omega_j^2 - \omega^2)^2 + \Gamma_j^2(\omega^3/\omega_j^2)^2}, \quad (3.2)$$

where ω_j is the angular frequency of the transition j from the energy state E_g to state E_j , $\omega_j = (E_j - E_g)/\hbar$, ω is the angular frequency of the light field and J and J' denotes the total electronic angular momentum of the transition. Γ_j is the decay rate of transition j . The values for this transitions can be found in [33].

Equations (3.1) and (3.2) correspond to a semiclassical interpretation of the atom-field-interaction [25]. In a quantum-mechanical interpretation, the dipole force arises from the position dependent shifts of the energy levels of the atoms in the presence of an external field. Consider a two-level atom with ground state $|g\rangle$ and excited state $|e\rangle$ and an optical transition frequency ω_a in field free space, as displayed in figure 3.1. In the presence of a light field, the energy levels are shifted due to the AC Stark effect. In the case of a far detuned light field, the lower level is shifted by [34]:

$$U_1 = \frac{\Omega^2}{4\Delta} \quad (3.3)$$

and the upper level is shifted by:

$$U_2 = -\frac{\Omega^2}{4\Delta}, \quad (3.4)$$

where $\Delta = \omega - \omega_a$ is the detuning of the field frequency ω from the atomic transition frequency ω_a . Ω is the Rabi frequency $\Omega = d|E|/2\hbar$, with d being the projected dipole

moment onto the axis of the field $|E|$. The process is shown in figure 3.1. For red detuned light ($\Delta < 0$), the ground state $|g\rangle$ is lowered and the excited state $|e\rangle$ is raised in energy. This causes atoms in the ground state to move towards regions of higher intensity (b). This can be used for example in optical tweezers [35].

In the case of a blue detuned field ($\Delta > 0$), the ground state is raised and the excited state is lowered in energy, so ground state atoms will be repelled by the light field (c). This has found applications, for example in atomic mirrors [7].

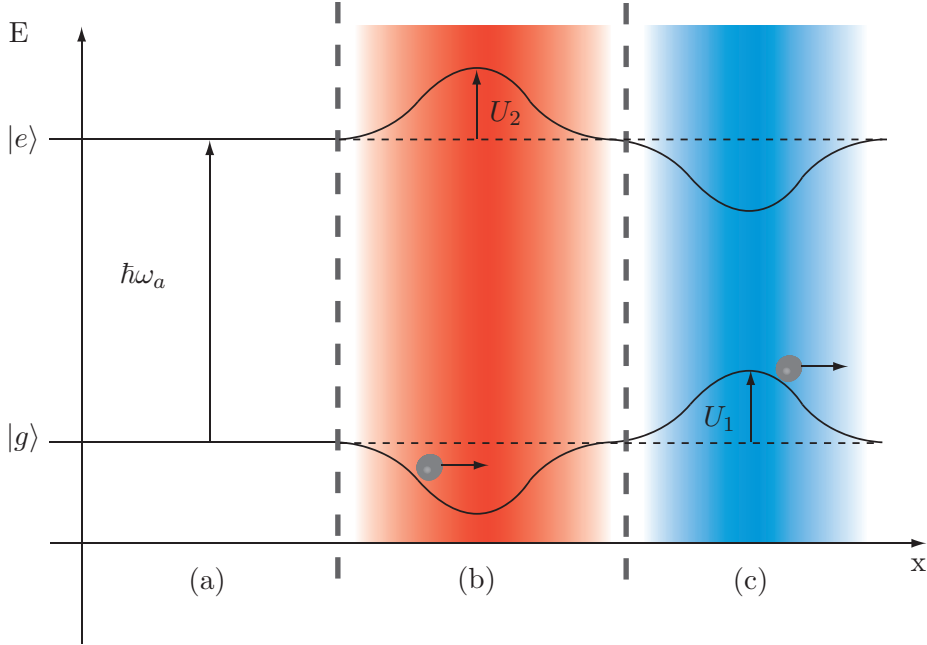


FIGURE 3.1: Schematic of the AC-Stark-Shift in a two-level system with ground state $|g\rangle$ and excited state $|e\rangle$. In the absence of a light field (a) the atomic transition frequency is $\hbar\omega_a$. In the presence of a red-detuned light field (b), the atomic ground state $|g\rangle$ is lowered in energy by U_1 and the excited state $|e\rangle$ increases in energy by U_2 , proportional to the intensity of the light field. Darker regions indicate locations of higher intensity. For a blue-detuned light field (c), the ground state $|g\rangle$ increases in energy, whereas the excited state $|e\rangle$ is lowered.

When the atoms are placed at the vicinity of a dielectric, the van der Waals potential also has to be taken into account. This is given by [36] as

$$V_{\text{vdW}}(r) = \frac{\hbar}{2\pi^3\epsilon_0} \sum_{l=-\infty}^{\infty} \int_0^{\infty} (k^2 K_l'^2(kr) + (k^2 + l^2/r^2) K_l^2(kr)) \times \left(\int_0^{\infty} \alpha(i\xi) G_l(i\xi) d\xi \right) dk, \quad (3.5)$$

where

$$G_l(\omega) = \frac{(\epsilon(\omega) - \epsilon_0) I_l(ka) I_l'(ka)}{\epsilon_0 I_l(ka) K_l'(ka) - \epsilon(\omega) I_l'(ka) K_l(ka)}. \quad (3.6)$$

Here, ϵ_0 is the dielectric constant in vacuum, k the wave number in vacuum, $I_l(x)$ is the modified Bessel function of first kind of order l and $K_l(x)$ is the modified Bessel function

of second kind of order 1, with $I'_l(x)$ and $K'_l(x)$ denoting their derivatives with respect to x . Instead of calculating the potential of a cylindrical surface, the fibre can be approximated as an infinite planar surface for very small distances. It can be shown that for an atom-fibre distance of fewer than 100 nm, the difference in the van der Waals potential of a silica fibre V_{fibre} and a infinite planar surface approximation V_{planar} is less than 10% [37]. This accuracy is sufficient for the configurations considered here, as the evanescent field induced dipole force is the stronger effect at larger distances and the van der Waals potential only becomes dominant at very short distances from the fibre. In this approximation the van der Waals potential is given by

$$V_{\text{vdW}} = -\frac{C_3}{r^3}, \quad (3.7)$$

where r is the distance between the atom and the surface and

$$C_3 = \frac{\hbar}{16\pi^2\varepsilon_0} \int_0^\infty \alpha(i\xi) \frac{\varepsilon(i\xi) - \varepsilon_0}{\varepsilon_0 + \varepsilon(i\xi)} d\xi, \quad (3.8)$$

given by [18]. For a caesium atom in the ground state C_3 is found to be $C_3 = 5.6 \times 10^{-49} \text{ J m}^3$ [37].

The total potential is thus given by equations (3.1) and (3.7) as:

$$U_{\text{tot}} = U_{\text{opt}} + V_{\text{vdW}}. \quad (3.9)$$

Equation (3.9) has been used for the calculation of the multimode traps presented in the following sections.

3.2 HE₁₁+TE₀₁ trap

This section introduces the different multimode traps, that can be created by two co-propagating modes in an ultra thin fibre. The general process of trap creation is discussed for the example of the trap of the quasi-linearly polarised fundamental mode HE₁₁ and the TE₀₁ mode. Then the features of this trap are investigated. Two other traps, formed by the HE₁₁+TE₀₁ and the TE₀₁+HE₂₁ modes are then analysed and finally a short comparison of the results will be given.

This section gives the basic creation process for the HE₁₁+TE₀₁ trap for caesium atoms with a kinetic energy corresponding to 100 μK , that can be analogously applied to the other multimode traps and introduces the leading arising quantities.

Creation of the trap

In this section the basic trap formation process for multimode traps is discussed for the example of the HE₁₁+TE₀₁ trap. However, it can be transferred analogously to any of the multimode traps discussed in this chapter. For the formation of the trap a tapered optical fibre with a radius of 400 nm and a propagating light field with a wavelength of about 850 nm is considered. This wavelength is blue-detuned with respect to the D₂ transition line in caesium from the 6²P_{3/2} to the 6²S_{1/2} state with a transition wavelength of 852.113 nm, which has been used as a model system (see appendix A.1). According to equation (2.28), this configuration results in a V parameter of $V = 3.11$. This parameter was chosen, so that only the four lowest order modes can propagate in the fibre as can

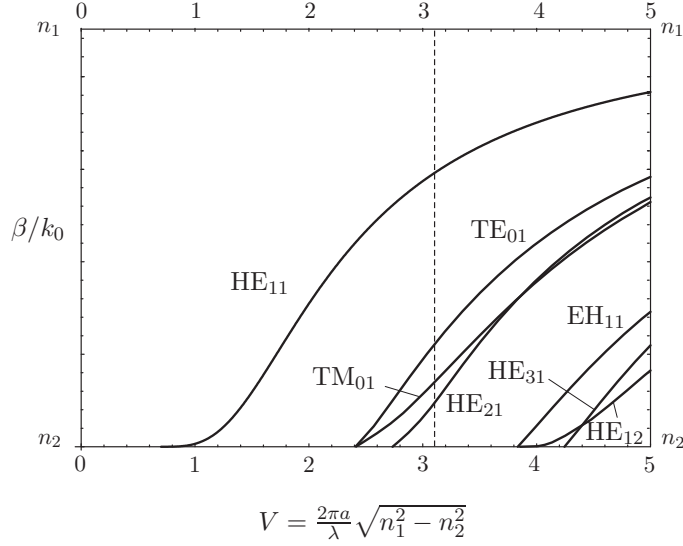


FIGURE 3.2: Normalised propagation constant β/k_0 over the V parameter for the first seven modes in a fibre. The dashed vertical line is located at $V=3.11$ which corresponds to the three trapping configurations around a pure silica fibre with radius $a = 400$ nm and a laser wavelength of 850 nm considered in this chapter.

be seen in figure 3.2. At this V parameter the HE₁₁ and TE₀₁ differ significantly in their propagation constant. Since the electric fields of the modes vary with $\vec{E} \propto e^{\omega t - \beta z}$ (compare to equation (2.6)), a difference in the propagation constant β thus causes a shift of the relative phase between the modes. This creates an interference pattern along the fibre axis, as shown in figure 3.3.

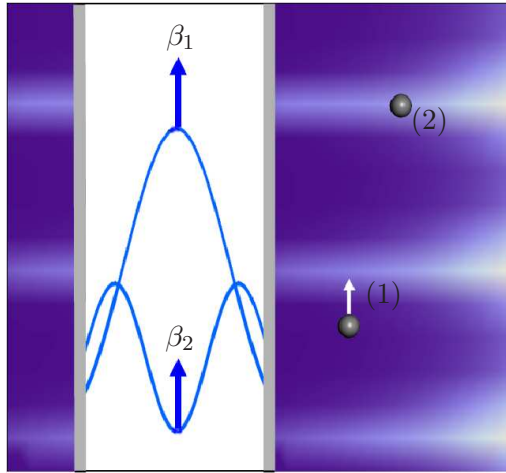


FIGURE 3.3: Intensity distribution of two co-propagating modes along the fibre axis. Due to the different propagation constants β_1 and β_2 an interference pattern occurs. Dark blue regions indicate regions of high blue-detuned intensity, light regions show regions of destructive interference and therefore low intensity. The grey spheres display atoms. In the high intensity region (1) they move towards regions of lower intensity due to the optical dipole force and settle in the minimum that is created along the radial direction (2).

Due to the repulsive optical dipole potential (compare to section 3.1), atoms in the evanescent field are confined axially in regions of low blue detuned light intensity. Azimuthal confinement is achieved by the different electric field distribution of the modes. The fields can only cancel where the field vectors point to opposite directions. For the superposition of the HE_{11} (figure 2.9) and the TE_{01} (figure 2.19) the location where both fields cancel is at $\phi = \pi/2$ (compare to figures 2.9 and 2.19). For the fields to completely cancel, the direction of the field vectors has to be opposed, but the absolute value has to be the same. Along the radial direction the evanescent fields of the different modes decay differently. This is depicted in figure 3.4 for the superposition of the HE_{11} and the TE_{01} , with 72% of the field's power in the HE_{11} mode and 28% in the TE_{01} mode. The parameter τ is defined as the fraction of total laser power P travelling in the HE_{11} mode, so here $\tau = 0.72$. As the HE_{11} mode carries more intensity but decays quicker than the TE_{01} mode ($\Lambda_{11} = 1/q_{11} = 164$ nm, $\Lambda_{01} = 1/q_{01} = 277$ nm), about 200 nm from the fibre surface, the intensity curves intersect. Here, the fields can optimally cancel, if the field vectors point into opposite directions.

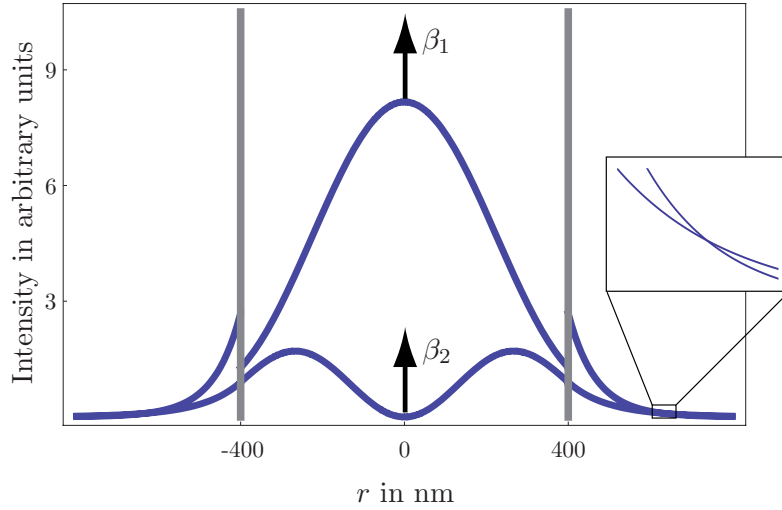


FIGURE 3.4: Two co-propagating modes in the fibre. The grey lines indicate the fibre surface. Note, that due to the different decay lengths of the modes, there is one location, where the intensities of both modes are equal. This is where the fields can optimally cancel.

In summary: Potential minima arise where the electric field components cancel each other due to the difference in the polarisation, propagation constant and decay length of the two modes. The periodicity of the interference pattern created by two modes with the propagation constants β_1 and β_2 is determined by the beat length between the modes

$$z_0 = \frac{2\pi}{\beta_1 - \beta_2}. \quad (3.10)$$

That way an array of microtraps is created along the fibre waist with a trapping site distance of z_0 . For the HE_{11} and the TE_{01} in this configuration the beat length is found to be $z_0 = 4.61$ μm , leading to an array of about 1000 potential trapping sites per side for a typical waist length for the tapered fibre of about 5 mm.

Trapping lifetime

One of the defining attributes of any atom trap is the trapping lifetime, that is, how long trapped atoms will remain inside the trap. Atoms leave the trap due to background collisions with the surrounding gas atoms, photon scattering and tunneling. As will be shown, the trap parameters are chosen such that atom loss due to tunneling can be neglected. The trapping lifetime is therefore restricted by the gas pressure of the experimental setup and the average light intensity the atoms experience. It has been shown by [38], that for a vacuum of 2×10^{-10} Torr, the lifetime due to background scattering is about 100 s.

The HE₁₁+TE₀₁ trap traps atoms in regions with low intensity. As will be shown, the field at the trapping minimum is zero. However, laser cooled atoms have a typical kinetic energy corresponding to several ten μK . Thus they will still move in the trap. This oscillation is depicted schematically in figure 3.5. Using a harmonic potential approximation,

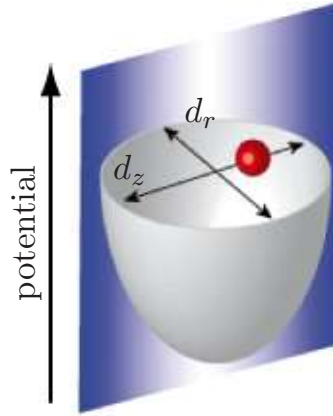


FIGURE 3.5: Harmonic approximation of the trap potential, here in the r - z -plane. The atom oscillates in the trap with amplitudes d_r and d_z . At the center of the trap the intensity is minimal, indicated by the white background. However, when the atom is displaced from the centre, it is affected by the field (darker blue region). The confinement in ϕ -direction is not depicted.

the atom oscillates in each direction with an amplitude d_i ($i \in \{r, \phi, z\}$) of the trap extension in the respective direction. The corresponding frequency is $\omega_i = \sqrt{k_i/m_{\text{atom}}}$ with k_i the spring constant for the respective direction and m_{atom} the mass of the atoms to be trapped. The trap minimum is located at minimal intensity. As soon as the atom leaves the centre of the trap, it experiences a non-zero field intensity. Here, heating by photon scattering occurs and causes the atoms to leave the trap. In order to calculate the trapping time, the rate of atom-photon scattering in the region of oscillation is calculated by fitting the minimum of the potential with a parabola. By determining the mean intensity the atom experiences by oscillating in the trap E_{mean} , one finds the scattering rate R_s per trap depth U by integrating over all oscillation modes [18]:

$$\frac{R_s}{U} = \frac{\kappa E_{\text{mean}}^2}{4\hbar U}, \quad (3.11)$$

where κ is the imaginary part of the atomic polarisability and \hbar is Planck's constant. With

every photon absorbed the atom gains energy in the form of recoil energy E_{rec}

$$E_{\text{rec}} = \frac{(\hbar k_0)^2}{2m_{\text{atom}}}. \quad (3.12)$$

The trapping lifetime t_t due to recoil heating is therefore given by

$$t_t = \frac{U}{2E_{\text{rec}}R_s}. \quad (3.13)$$

The parameters for the multimode traps are chosen to result in a trapping lifetime of $t_t \approx 100$ s and a trap depth of $U \approx 1$ mK.

Properties of the HE₁₁+TE₀₁ trap

The formulas derived in the previous sections are now applied to the HE₁₁+TE₀₁ configuration. The used laser power is 50 mW at a wavelength of 850.5 nm in a fibre of pure silica ($n_1 = 1.452$) with a waist radius of 400 nm surrounded by vacuum ($n_2 = 1$). This is well below the damage threshold for such a fibre: It has been experimentally shown that appropriately produced fibres with an even smaller radius of 250 nm can carry more than 300 mW of power even in vacuum without fusing [31]. With 72% of the power propagating in the HE₁₁ mode and 28% in the TE₀₁ mode, a trap for cold caesium atoms with a trapping minimum at 134 nm from the fibre surface is created. The parameters are chosen, so that the depth of the trap is about 1 mK and the trapping lifetime resulting from heating due to spontaneous scattering of photons exceeds 100 seconds for caesium atoms with an initial kinetic energy corresponding to 100 μ K.

Figure 3.6 shows a contour plot of the trapping potential including the van der Waals surface potential [39] in the plane of the potential minimum at the axial position $z = 4.61 \mu\text{m}$, where $z = 0$ denotes the beginning of the fibre waist. For the calculations, the van der Waals potential of an infinite planar silica surface is used [18]. The trapping minimum in azimuthal direction is located at $\phi = \pi/2$, $r = 534$ nm and $z = 4.61 \mu\text{m}$ (compare to figures 2.9 and 2.19). Here, the polarisation of the two modes matches and the interference is maximally destructive. Note that while destructive interference takes place at an azimuthal angle $\phi = \pi/2$, there is constructive interference at $\phi = 3\pi/2$. When varying the polarisation angle (parameter φ_0 in equations (2.34) and (2.35)), the azimuthal position of the trap can be varied because the potential has a $\cos^2(\phi - \varphi_0)$ dependence. Using a harmonic potential approximation, the azimuthal oscillation frequency is calculated to be $\omega_\phi/2\pi \approx 1.07$ MHz. The extension of the trap volume in the azimuthal direction for caesium atoms with a kinetic energy corresponding to 100 μ K is $d_\phi = 34$ nm.

A contour plot of the trapping potential in the plane $x = 0$ is shown in figure 3.7. The interference between the modes creates an array of traps in the axial direction with a periodicity given by the beat length of the two co-propagating modes, $z_0 = 4.61 \mu\text{m}$. In addition, there is a second array of traps on the opposite side of the fibre with same periodicity which is shifted by $z_0/2$, that is created when the linearly oscillating electric field components cancel each other, with one of the fields phase-shifted by $\phi = \pi$ with respect to the superposition at $z = 0$. The potential has a $\sin^2((\beta_{11} - \beta_{01})z)$ dependence in the axial direction. The axial trapping frequency is calculated to be $\omega_z/2\pi \approx 528$ kHz. The extension of the trap volume in this direction for caesium atoms with a kinetic energy corresponding to 100 μ K is $d_z = 68$ nm.

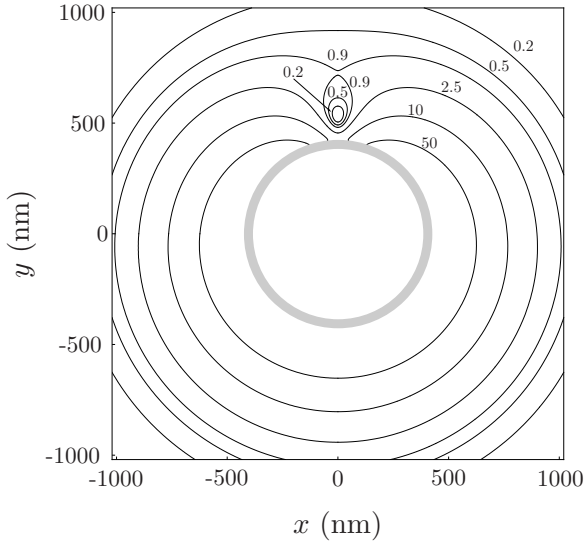


FIGURE 3.6: Contour plot of the HE₁₁+TE₀₁ trap in the plane $z = 4.61 \mu\text{m}$ for the following parameters: $P = 50 \text{ mW}$, $\tau = 0.72$, $\lambda = 850.5 \text{ nm}$, $a = 400 \text{ nm}$, $n_1 = 1.452$, and $n_2 = 1$. The fibre surface is indicated by the grey circle and the equipotential lines are labelled in mK.

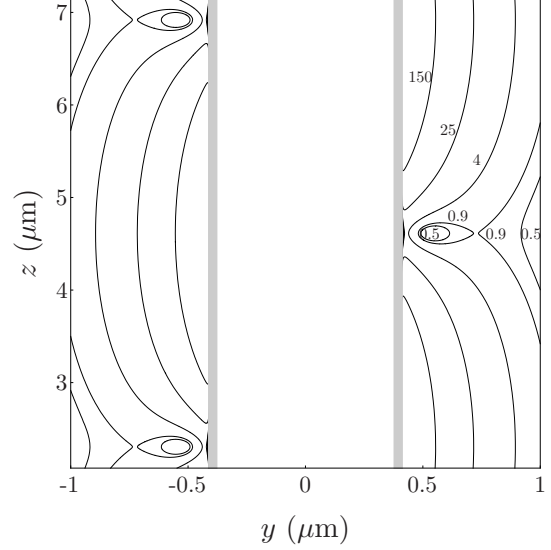


FIGURE 3.7: Contour plot of the HE₁₁+TE₀₁ trap in the plane $x = 0$ for the same parameters as in figure 3.6. The fibre surface is indicated by the two vertical grey lines and the equipotential lines are labelled in mK.

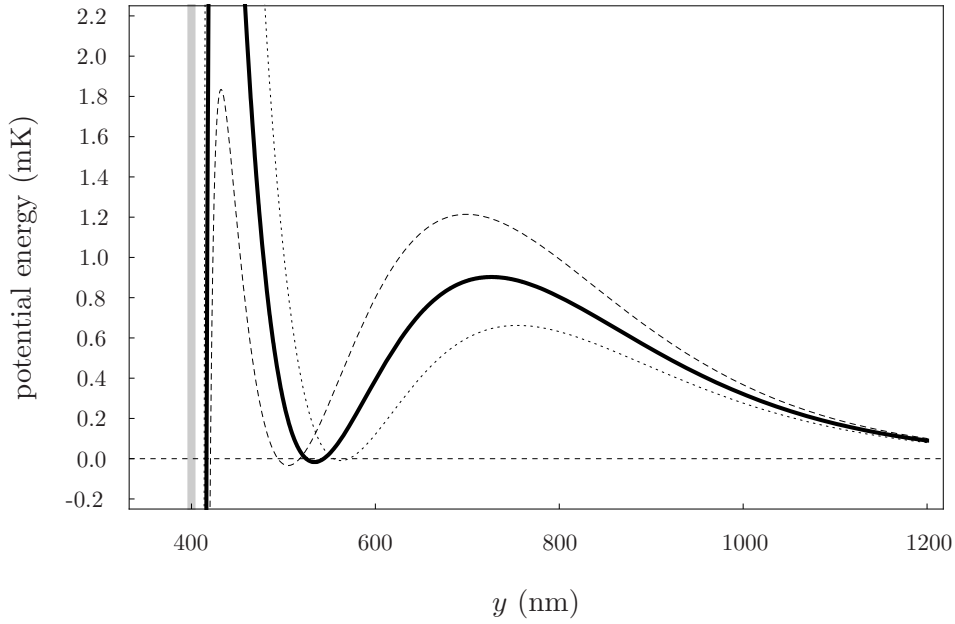


FIGURE 3.8: Plot of the trapping potential versus the position along the y axis for $P_{11} = \tau_0 P$ (solid line), $P_{11} = (\tau_0 + \sigma)P$ (dotted line) and $P_{11} = (\tau_0 - \sigma)P$ (dashed line). The parameters are the same as in figure 3.6. The fibre surface is indicated by the vertical grey line.

The trapping potential along the y -axis is depicted in figure 3.8. The solid black line corresponds to the sum of the light-induced potential and the van der Waals potential when 72% of the power propagates in the HE_{11} mode. The dashed and dotted lines correspond to the same potential assuming slightly different power distributions between the modes: The fraction of the total laser power P that is transmitted through the fibre by the HE_{11} mode is described by the parameter τ , such that $P_{11} = \tau P$ and $P_{01} = (1 - \tau)P$, where P_{11} denotes the power propagating in the HE_{11} mode, and P_{01} the power propagating in the TE_{01} mode. Let us now assume, that the power distribution between the modes has experimental uncertainties. For this purpose, the standard deviation σ of a binomial distribution is used. Assuming $\tau = \tau_0 \pm \sigma$ can be controlled with a precision of $\sigma = 0.05\sqrt{\tau_0(1 - \tau_0)}$, that is, $\sigma = 0.025$ for $\tau_0 = 0.5$. For the case of $\tau_0 = 0.72$, the power distribution between the modes τ would then be controlled within ± 0.022 . This value is considered to be a conservative assumption for the precision of the power distribution between the two modes. For the case of $P_{11} = (\tau_0 + \sigma)P$ the trap is 27% shallower compared to the trap for $P_{11} = \tau_0 P$, whereas for the case of $P_{11} = (\tau_0 - \sigma)P$ the trap is 30% deeper. However, while the trap depth increases when decreasing τ , the trapping minimum is also shifted towards the fibre. When the trapping minimum is shifted too close towards the fibre surface, the van der Waals potential, that is negligible further out is the dominant effect and the potential barrier in the direction towards the fibre decreases rapidly. Furthermore, the potential barrier also becomes narrower which would eventually lead to tunnelling of the atoms out of the trap. The parameters presented here have been chosen in such a way that even with realistic experimental uncertainties the trap remains sufficiently deep and the tunnelling is negligible compared to the trapping lifetime. Note that the total potential is negative at its minimum due to the influence of the van der Waals potential. Since the z -component of the electric field in the HE_{11} mode vanishes at $\phi = \pi/2$, the polarisation in the two modes perfectly matches at the intensity minimum and the van der Waals potential at this position is the only influence on the atoms. The radial trapping frequency is calculated to be $\omega_r/2\pi \approx 770$ kHz and the extension of the trapping volume in the radial direction for caesium atoms with a kinetic energy corresponding to a temperature of $100 \mu\text{K}$ is $d_r = 47$ nm.

The calculations of the lifetime have been performed assuming caesium atoms with an initial kinetic energy equivalent to $100 \mu\text{K}$. Since the trap is not perfectly symmetric along the y -axis (see figure 3.8), one has to account for this by biasing the oscillation amplitude in this direction. Using this method, the scattering rate is found to be 39 photons/second and the trapping lifetime is 108 seconds (see equations (3.11) to (3.13)).

3.3 $\text{HE}_{11} + \text{HE}_{21}$ trap

This section introduces the trap arising from HE_{11} and the HE_{21} mode. It is created using $P = 25$ mW of light at a wavelength of $\lambda = 849.0$ nm and a pure silica fibre of 400 nm radius. The polarisation orientation of the modes has been chosen such that the trap forms at $\phi = 0$. This corresponds to $\varphi_0 = \phi_0 = 0$ in equations (2.34), (2.35), (2.44) and (2.45), respectively. With 84% of the power propagating in the HE_{11} mode, that is, $\tau = 0.84$, a trap at 152 nm from the fibre surface is formed. The depth of the trap is $U = 1.2$ mK and the trapping lifetime resulting from spontaneous scattering of photons exceeds $t_t = 100$ seconds for caesium atoms with a kinetic energy corresponding to $100 \mu\text{K}$.

A contour plot of the trapping potential in the x - y -plane at the axial position of the potential minimum, $z=3.45 \mu\text{m}$ is shown in figure 3.9. As the direction towards minimal barrier is not in r -direction, the two dashed lines with their origin at the center of the trap indicate the two directions with minimal potential barrier which, by consequence, determine the depth of the trap (see figure 3.12). The trapping minimum is at $\phi = 0$, $r = 552 \text{ nm}$ and $z = 3.45 \mu\text{m}$. It lies on the x -axis because here the polarisation of the two modes matches and the interference is maximally destructive (compare figures 2.9 and 2.14). However, unlike the HE₁₁+TE₀₁ trap considered in section 3.2, the polarisation matching between the two modes is not perfect. This is due to the fact that the ratio $E_z/|E_{\perp}|$ at the trapping minimum is different for the two modes and, therefore, the electric fields never cancel completely. This stems from the orientation of \vec{E}_{\perp} at the position of the trap: When the transverse electric field is perpendicular to the fibre surface, a non-vanishing z -component of the electric field arises [40]. This polarisation configuration results in a more intense evanescent field allowing the creation of a trap comparable to the one presented in section 3.2 with only 50% of the power. As a drawback, the intensity at the trapping minimum is not zero. When varying the polarisation angles (parameters φ_0 and ϕ_0 in equations. (2.34), (2.35), (2.44) and (2.45)), the azimuthal position of the trap can be varied. The azimuthal oscillation frequency is $\omega_{\phi}/2\pi \approx 330 \text{ kHz}$. The extension of the trapping volume in the azimuthal direction for caesium atoms with a kinetic energy corresponding to $100 \mu\text{K}$ is $d_{\phi} = 104 \text{ nm}$.

Figure 3.10 shows the contour plot of the trapping potential in the plane $y=0$. Like in the HE₁₁+TE₀₁ trap, the interference between the modes creates an axial array of traps with a periodicity given by the beat length of the two co-propagating modes, $z_0 = 3.45 \mu\text{m}$. Again, there is a second array of traps at the opposite side of the fibre with the same periodicity and shifted by $z_0/2$. The potential has a $\sin^2((\beta_{11} - \beta_{21})z)$ dependency in the axial direction plus the offset due to the unbalanced z -components of the electric fields of the two modes. The axial trapping frequency is calculated to be $\omega_z/2\pi \approx 610 \text{ kHz}$. The extension of the trapping volume in the axial direction for caesium atoms with a kinetic energy corresponding to $100 \mu\text{K}$ is $d_z = 58 \text{ nm}$.

The trapping potential versus the position along the x -axis is shown in figure 3.11 for $P_{11} = \tau_0 P$, $P_{11} = (\tau_0 - \sigma)P$, and $P_{11} = (\tau_0 + \sigma)P$, with $\tau_0 = 0.84$ and $\sigma = 0.018$. P denotes the total power propagating through the fibre and P_{11} the power propagating in the HE₁₁ mode. Again, τ is assumed to be controlled with a precision of $\sigma = 0.05\sqrt{\tau_0(1 - \tau_0)}$. The light-induced potential does not vanish at the minimum due to the mismatch in the polarisation between the two modes. This leads to a higher scattering rate of 57 photons/second compared to the HE₁₁+TE₀₁ trap. The radial trapping frequency is $\omega_r/2\pi \approx 970 \text{ kHz}$. The extension of the trapping volume in the radial direction for caesium atoms with a kinetic energy corresponding to $100 \mu\text{K}$ is $d_r = 37 \text{ nm}$. Note, that the depth of the potential shown in figure 3.11 does not correspond to the depth of the trap because, as mentioned above, the direction with minimal potential barrier for the atoms is not radial. Figure 3.12 therefore shows the trapping potential against the position along the direction with minimal potential barrier. The solid, dashed and dotted lines have been calculated for the same values of τ as in figure 3.11. The direction with minimal potential barrier l is indicated as the straight line that connects the potential minimum in the trap with the lowest local potential maximum. Since l depends on τ and has, per definition, its origin at the trapping minimum, the three minima of the potential profiles shown in figure 3.12 are located at $l = 0$. The trap depth is then found to be $U = 1.2 \text{ mK}$. For the case of

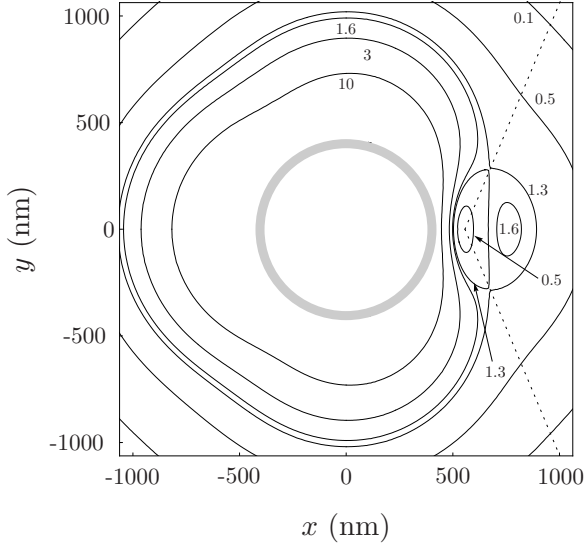


FIGURE 3.9: Contour plot of the $\text{HE}_{11}+\text{HE}_{21}$ trap in the plane $z = 3.45 \mu\text{m}$ for the following parameters: $P = 25 \text{ mW}$, $\tau = 0.84$, $\lambda = 849.0 \text{ nm}$, $a = 400 \text{ nm}$, $n_1 = 1.452$, and $n_2 = 1$. The fibre surface is indicated by the grey circle and the equipotential lines are labelled in mK.

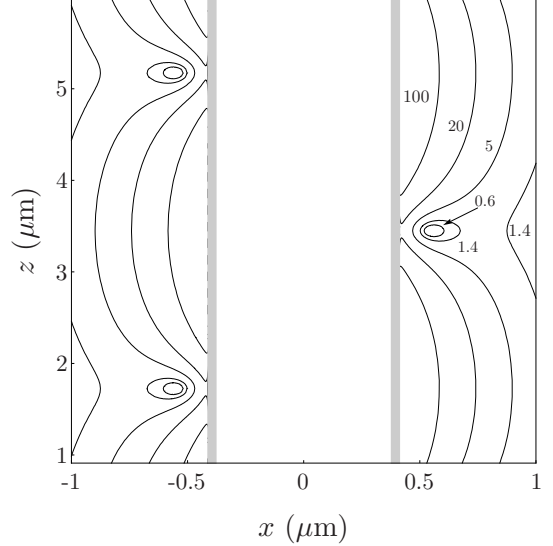


FIGURE 3.10: Contour plot of the $\text{HE}_{11}+\text{HE}_{21}$ trap in the plane $y = 0$ for the same parameters as in figure 3.9. The fibre surface is indicated by the two vertical grey lines and the equipotential lines are labelled in mK.

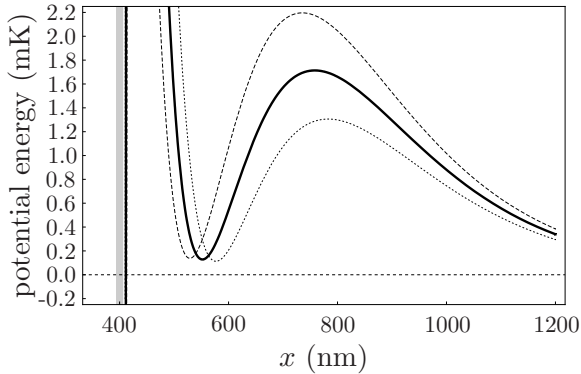


FIGURE 3.11: Plot of the trapping potential versus the position along the x axis for $P_{11} = \tau_0 P$ (solid line), $P_{11} = (\tau_0 + \sigma)P$ (dotted line) and $P_{11} = (\tau_0 - \sigma)P$ (dashed line). The parameters are the same as in figure 3.9. The fibre surface is indicated by the vertical grey line.

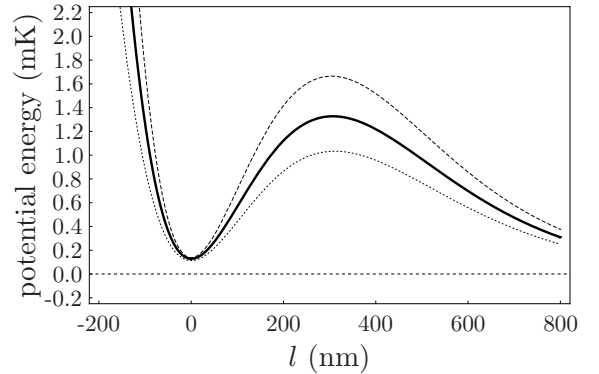


FIGURE 3.12: Plot of the trapping potential versus the position along the direction of minimal potential barrier $l(\tau)$ for $P_{11} = \tau_0 P$ (solid line), $P_{11} = (\tau_0 + \sigma)P$ (dotted line) and $P_{11} = (\tau_0 - \sigma)P$ (dashed line). The parameters are the same as in figure 3.9.

$P_{11} = (\tau_0 + \sigma)P$ (dotted line) the trap is 33% shallower compared to the trap for $P_{11} = \tau_0 P$ (solid line), whereas for the case of $P_{11} = (\tau_0 - \sigma)P$ (dashed line) the trap is 17% deeper. Finally, a trapping lifetime of 106 seconds is calculated for caesium atoms with an initial kinetic energy corresponding to 100 μK . Again, the tunnelling through the potential barrier in the radial direction towards the fibre (see figure 3.11) is negligible compared to the lifetime of the atoms in the trap.

3.4 HE₂₁+TE₀₁ trap

Finally, the trap arising from the interference between the TE₀₁ and the HE₂₁ mode is introduced. It can be created using 30 mW of light at a wavelength of 851.0 nm and the same fibre parameters as in the above sections. The polarisation orientation of the modes has been chosen such that the trap forms at $\phi = 3\pi/4$ and at $\phi = -\pi/4$. This trapping configuration has two trapping minima in the same z -plane, whereas in the traps discussed before there is only one trapping minimum per z -plane. The polarisation orientation corresponds to $\phi_0 = 0$ in equations (2.44) and (2.45) for the HE₂₁ mode. With 68% of the power propagating in the TE₀₁ mode, that is, $\tau = 0.68$, a trap for cold caesium atoms with its trapping minimum at 184 nm from the fibre surface is formed. The depth of the trap is $U = 1.4$ mK and, like in the above cases, the trapping lifetime resulting from spontaneous scattering of photons exceeds 100 seconds for caesium atoms with an initial kinetic energy corresponding to 100 μK .

The trap in the x - y -plane at the position of minimal potential $z = 13.67$ μm is depicted in figure 3.13. Here, the trapping minima are shown to be at $\phi = 3\pi/4$, $r = 584$ nm and at $\phi = -\pi/4$, $r = 584$ nm, because the polarisation in the two modes matches at these positions (compare to figures 2.14 and 2.19). Like for the HE₁₁+TE₀₁ case, the polarisation matching between the two modes is perfect because the z -component of the electric field in the HE₂₁ mode vanishes at the position of the trap. The azimuthal oscillation frequency is calculated to be $\omega_\phi/2\pi \approx 2.60$ MHz. The extension of the trapping volume in the azimuthal direction for caesium atoms with a kinetic energy corresponding to 100 μK is $d_\phi = 14$ nm. This strong confinement in the azimuthal direction stems from the behaviour of the polarisation of the electric field in the two modes at the position of the trap. When increasing ϕ , the polarisation of the HE₂₁ mode rotates clockwise, whereas the polarisation of the TE₀₁ mode rotates counterclockwise. This produces a fast polarisation mismatch between the two fields when displacing the position along the azimuthal direction and thereby a steep increase of the potential.

A contour plot of the trap in the z - d -plane, where $d = (y - x)/\sqrt{2}$ is the radial direction from the fibre that passes through the trapping minima is shown in figure 3.14. The interference between the modes creates four axial arrays of traps with a periodicity of $z_0 = 13.67$ μm . The two trapping minima shown in figure 3.13 show the azimuthal positions of one pair of arrays. The second pair is shifted with respect to the first one by $\phi = \pi/2$ and $z = z_0/2$. We calculate the axial trapping frequency to be $\omega_z/2\pi \approx 204$ kHz. The extension of the trapping volume in the axial direction for caesium atoms with a kinetic energy corresponding to 100 μK is $d_z = 174$ nm. This elongation of the trap compared to the traps presented in sections 3.2 and 3.3 stems from the large beat length between the TE₀₁ and the HE₂₁ mode.

Figure 3.15 depicts the radial trapping potential in the above defined z - d -plane for

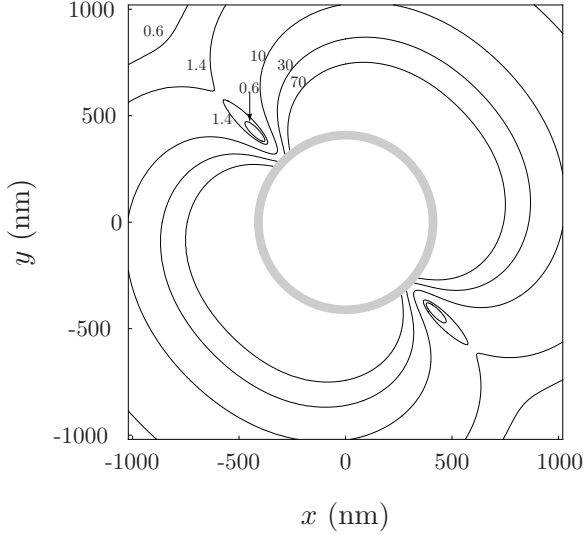


FIGURE 3.13: Contour plot of the $TE_{01}+HE_{21}$ trap in the plane $z = 13.67 \mu\text{m}$ for the following parameters: $P = 30 \text{ mW}$, $\tau = 0.68$, $\lambda = 851.0 \text{ nm}$, $a = 400 \text{ nm}$, $n_1 = 1.452$, and $n_2 = 1$. The fibre surface is indicated by the grey circle and the equipotential lines are labelled in mK. The dashed line gives the direction of minimal potential barrier.

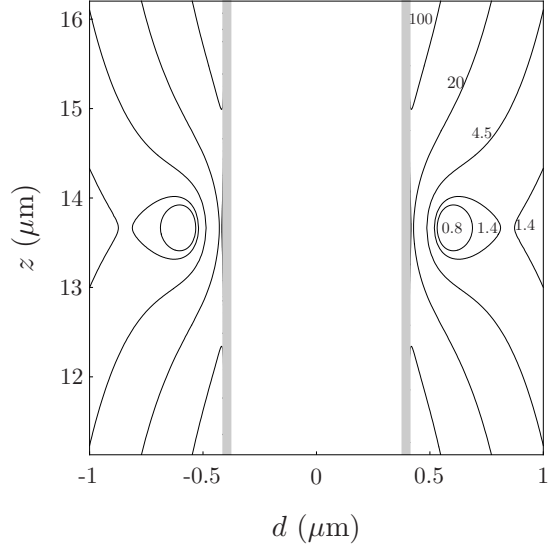


FIGURE 3.14: Contour plot of the $TE_{01}+HE_{21}$ trap in the z - d -plane, where $d = (y - x)/\sqrt{2}$ for the same parameters as in figure 3.13. The fibre surface is indicated by the two vertical grey lines and the equipotential lines are labelled in mK.

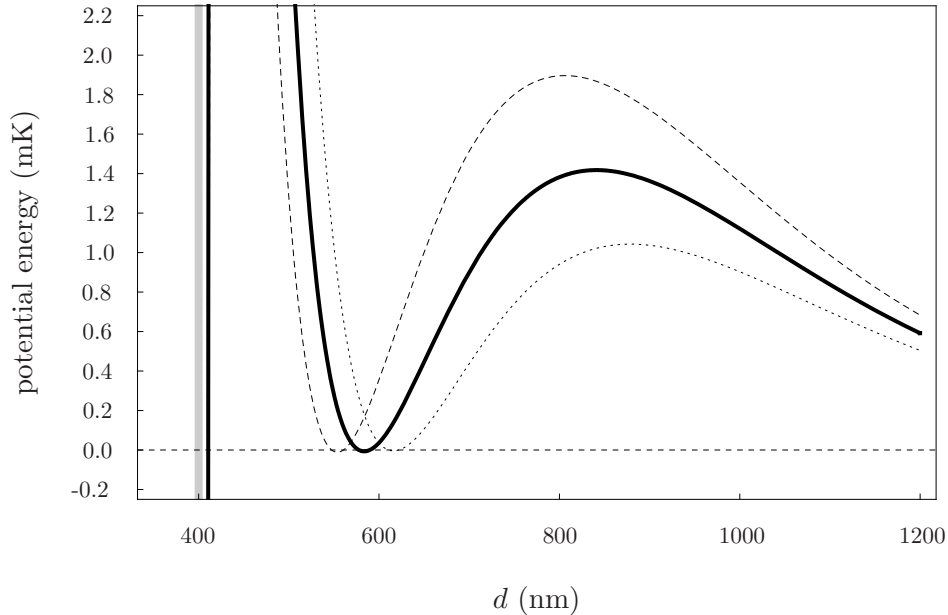


FIGURE 3.15: Plot of the trapping potential versus the position along the $d = (y - x)/\sqrt{2}$ axis for $P_{11} = \tau_0 P$ (solid line), $P_{11} = (\tau_0 + \sigma)P$ (dotted line) and $P_{11} = (\tau_0 - \sigma)P$ (dashed line). The parameters are the same as in figure 3.13. The fibre surface is indicated by the vertical grey line.

$P_{01} = \tau_0 P$, $P_{01} = (\tau_0 - \sigma)P$, and $P_{01} = (\tau_0 + \sigma)P$, with $\tau_0 = 0.68$ and $\sigma = 0.023$. Again, τ is assumed to be controlled with a precision of $\sigma = 0.05\sqrt{\tau_0(1-\tau_0)}$. For the case of $P_{11} = (\tau_0 + \sigma)P$ the trap is 25% shallower compared to the trap for $P_{11} = \tau_0 P$, whereas for the case of $P_{11} = (\tau_0 - \sigma)P$ the trap is 36% deeper. Despite the vanishing light-induced potential at the trapping minimum, the total potential does not become significantly negative because the influence of the van der Waals potential at this distance from the fibre surface is negligible. The radial trapping frequency is calculated to be $\omega_r/2\pi \approx 770$ kHz. The extension of the trapping volume in the radial direction for caesium atoms with a kinetic energy corresponding to $100 \mu\text{K}$ is $d_r = 47$ nm. Since the beat length between the TE₀₁ and the HE₂₁ mode is large compared to the beat length in the other two traps, one would expect the radial size of the trap to be large as well. However, the difference in the decay lengths $\Lambda_{21} - \Lambda_{01}$ is not the only factor that influences the radial profile of the trap. It is also determined by the exact functional dependence of the evanescent field for the different modes which results in a similar radial confinement compared to the HE₁₁+TE₀₁ and HE₁₁+HE₂₁ configurations. Finally, the scattering rate and the trapping lifetime for caesium atoms with an initial kinetic energy corresponding to $100 \mu\text{K}$ is calculated to be 62 photons/second and 114 seconds, respectively.

3.5 Traps using the TM₀₁ mode

The TM₀₁ mode cannot be used to create an effective blue-detuned interference trap in combination with the other considered modes, because of its large z -component of the electric field. Hence the electric field cancellation that depends on the polarisation matching between the co-propagating modes is only partial and the trap created is inefficient. Figure 3.16 exemplary shows the TE₀₁ + TM₀₁ trap, using 20 mW of total laser power at a wavelength of 849.5 nm. The τ -parameter gives the fraction of laser power in the TE₀₁ mode. The features of the the TM₀₁ trap will not be examined further here.

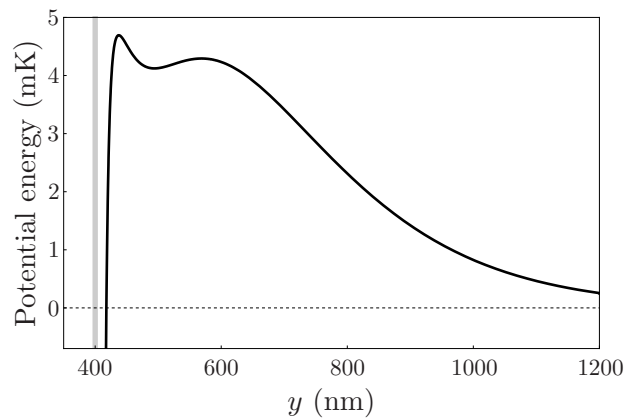


FIGURE 3.16: Plot of the trapping potential for the TM₀₁+TE₀₁ trap along the y -axis for the following parameters: $P = 20$ mW, $\tau = 0.57$, $\lambda = 849.5$ nm, $a = 400$ nm, $n_1 = 1.452$, and $n_2 = 1$. The fibre surface is indicated by the vertical grey line.

3.6 Loading the traps

This section will give an experimental scheme to load cold caesium atoms into the traps. As can be seen in figures 3.8, 3.12 and 3.15, the atoms cannot enter the traps due to the repulsive barrier on both sides of the trap. One possibility is therefore to create the traps abruptly, when the atoms are cooled next to the fibre. The cooling could be done with a magneto-optical trap (MOT) [41] at the fibre waist. Atoms cooled this way have a typical kinetic energy corresponding to a temperature of about 100 mK when creating the trap. The trap volume for the HE₁₁+TE₀₁ trap for this energy can be determined by assuming an ellipsoid with equatorial radii d_r, d_ϕ and d_z , as they have been determined in sections 3.2 to 3.4. This would yield a trap volume of $V_{\text{trap}} = 4/3\pi d_r d_\phi d_z = 1.1 \times 10^{-16} \text{ cm}^3$. So with a typical MOT density of $\rho = 10^{10} \text{ atoms/cm}^3$ [42] one would expect an average of 2.2×10^{-6} trapped atoms per trapping site or a total of 2.2×10^{-3} for 1000 trapping sites. This is an inefficient scheme.

A different possibility has been examined by [43]. Here it is shown that for a small trap size and high loading rates (that is, number of atoms per second entering the dipole trap) there exists a so-called *collisional blockade regime*. If the loading rate R is large enough, every trap site would be occupied by an atom. When another atom enters the trap, the atoms collide due to the small trapping volume. One atom emits a photon and is subsequently lost. The other atom absorbs the emitted photon. This would cause both atoms to leave the trap [43], resulting in an average trap occupation of 0.5 atoms per trap site. To continuously load the traps, the potential barrier has to be lowered to zero, so the atoms can be cooled into the trap. As has been experimentally shown, a MOT can be operated normally in the vicinity of an ultra thin fibre [31]. To continuously load the trap, the potential barrier is lowered by using a red-detuned laser during the loading process, as is shown in figure 3.17(a). Here a wavelength of $\lambda = 970 \text{ nm}$ with a power of $P = 9.2 \text{ mW}$ is used at a starting τ parameter of 0.89. Starting from the loading rate of 100 s^{-1} assumed in [43] and taking into account our smaller trap size and the smaller angle under which the atoms are allowed into the trap, an estimated loading rate of $R = 0.3 \text{ s}^{-1}$ is achieved. This loading rate exceeds the loss rate of 0.1 s^{-1} due to background gas collisions at a pressure of 10^{-9} Torr [32]. According to [43] the trap would then operate in the collisional blockade regime, resulting in a trap occupancy of 0.5 atoms per site or a total of 200-300 trapped atoms along a 5 mm waist for a MOT with a $1/\sqrt{e}$ -radius of 0.6 mm. The original configuration can be restored in two steps: First, the τ parameter is returned to its original value as is shown in figure 3.17(b) and then the red-detuned laser is turned off (figure 3.17(c)). This way it is possible to trap 200-300 atoms in the then purely blue-detuned trap.

3.7 Summary

The traps discussed in this chapter have different features that distinguishes one from the other. Their characterising quantities are arranged in table 3.1. The values for the detuning of the wavelength and the distribution of laser power is chosen such that the trap depth and trapping lifetime is comparable. Note, that while the HE₁₁+TE₀₁ trap is created with more laser power than the other traps, the minimum of the trap is at zero light intensity, like in the case of the HE₂₁+TE₀₁ trap, whereas in the HE₁₁+HE₂₁

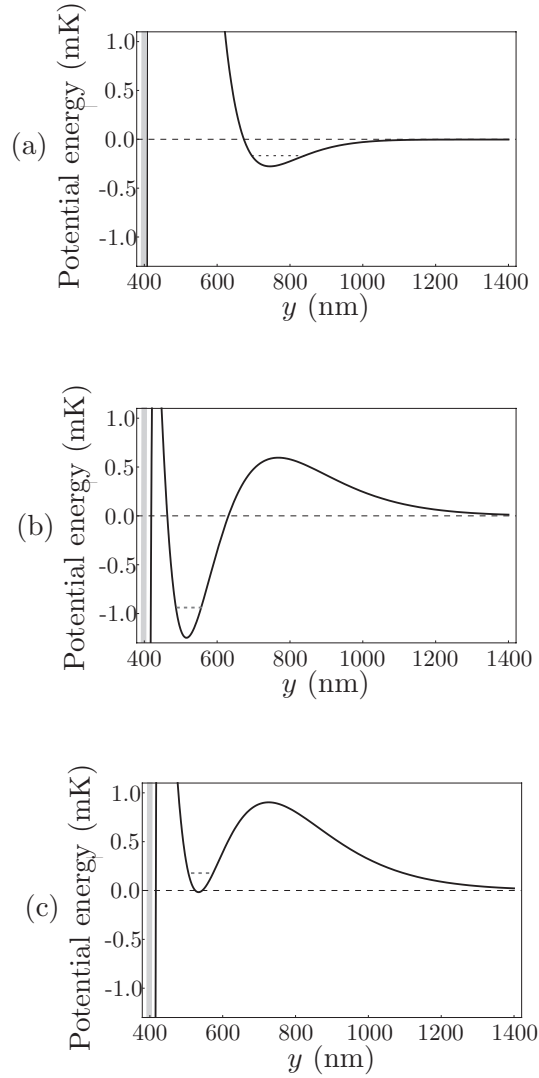


FIGURE 3.17: Scheme for loading the $\text{HE}_{11}+\text{TE}_{01}$ trap. In (a) a plot of the trapping potential for the $\text{HE}_{11}+\text{TE}_{01}$ trap along the y -axis is shown for a τ parameter of 0.89. In the presence of a red-detuned light field of $P = 9.2$ mW laser power at a wavelength of $\lambda = 970$ nm, the potential barrier is lowered, so the atoms can be cooled into the trap from the far side of the fibre. Step two of the trap loading scheme is shown in (b). The τ parameter is restored to 0.72, no more loading takes place. In (c), the red-detuned light has been turned off and the trap has returned to the final state as in figure 3.8. The fibre surface is indicated by the vertical grey line. The grey dotted line represents the energy of the atoms.

trap, there is a finite intensity at the potential minimum. However, the $\text{HE}_{11}+\text{TE}_{01}$ trap has its minimum close to the fibre surface, making it interesting for the examination of atom-surface interactions.

	$\text{HE}_{11}+\text{TE}_{01}$	$\text{HE}_{11}+\text{HE}_{21}$	$\text{HE}_{21}+\text{TE}_{01}$
used power P in mW	50	25	30
light wavelength λ in nm	850.5	849.0	851.0
trap volume V in 10^{-16} cm^3	1.1	9.3	4.8
trapping time t_t in s	108	106	114
τ parameter	0.72	0.84	0.68
trap depth U in mK	0.92	1.20	1.40
beat length z_0 in μm	4.61	3,45	13.67

TABLE 3.1: Comparison of the trapping parameters for the multimode traps.

Note, that there is also a striking difference in the beat length of the multimode traps. This is based on the fact, that the higher order modes HE_{21} and TE_{01} have a similar propagation constant at the given parameters, whereas the difference in the propagation constants with the higher order modes to the fundamental mode HE_{11} is larger (see figure 3.2). The beat length is inversely proportional to the difference in propagation constants (equation 3.10), resulting in a larger beat length. Therefore, this particular trap creates an array with less trapping sites along the fibre waist compared to the $\text{HE}_{11}+\text{TE}_{01}$ trap and the HE_{11} and HE_{21} trap.

As a final remark, one would expect the experimental realization of a trap involving the fundamental mode to be advantageous, as the HE_{11} mode is theoretically and experimentally well studied, whereas the creation and control of higher order modes is relatively unexplored.

4 Investigation of modes in ultra thin optical fibres

In order to experimentally examine the theoretical predictions of chapter 3, a setup to study the behaviour of the modes during the tapering process has been developed. Using a CCD camera, the interference of several co-propagating modes in the same fibre during the fibre tapering process is investigated.

In addition, a second setup to examine the evanescent field arising around an ultra thin fibre has been designed and realised. It features two subwavelength diameter fibres, whose relative angle can be chosen and whose relative distance can be controlled with an accuracy of a few tens of nanometres. One fibre carries a light field and thus possesses an evanescent field. Instead of using a scanning near field optical microscope (SNOM), as has been done for example in [44], the field is probed by bringing a second TOF near the waist of the field fibre. Depending on the relative angle between the fibres and polarisation of the field, light is coupled into the probe fibre and can be detected using a photodiode detection setup. The setup is used to examine the azimuthal dependence of the fundamental HE_{11} mode's evanescent field, to determine its radial decay length and to measure the longitudinal modulation of a standing wave pattern. The fibres used are standard commercial optical fibres, that are heated and tapered to the desired waist diameter with the fibre tapering machine situated in our laboratory [27].

This Chapter briefly introduces the basic steps of the fibre tapering process and specifies the fibre taper profile used throughout the experiments. Then, the experimental setups are introduced and the measured results are given and analysed.

4.1 Fibre tapering

In this section the fibre tapering process will be described. For a more detailed treatment, see [27].

The tapering setup is shown in figure 4.1. To pull a fibre to a given waist diameter the acrylate jacket has to be removed first. The fibre is fixed on the translation stages with holding magnets. The uncoated part of the fibre is then heated with an hydrogen-oxygen flame. The heated part of the fibre melts and is subsequently stretched to the desired waist radius: The translator stage moves the fibre relative to the flame to increase the effective width of the flame along the fibre. This allows better control over the taper profile than in the case of a static flame. The stretcher stage is mounted on the translation stage and stretches the fibre. Since the fibre melts, when heated by the burner, it is elongated by the stretching, leading to a reduction of the fibre radius. The “pulling” of the fibre with the positioning stages is computer controlled, this way the desired fibre radii can be reached with an a priori precision of about $\pm 5\%$ [27].

The profile of the tapered fibre is crucial for its transmission properties. Consider the fundamental mode that is guided in the core of the untapered part of the fibre. In the

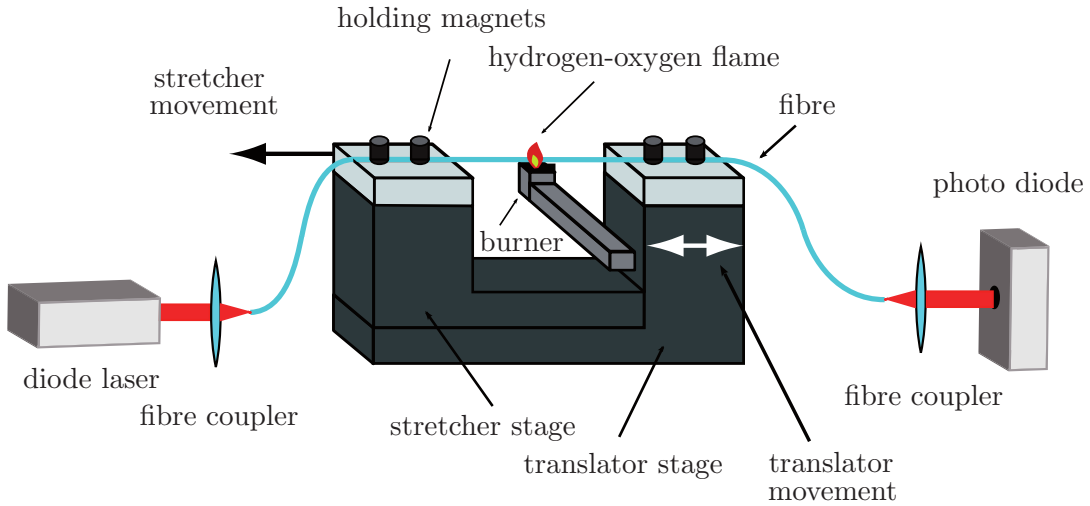


FIGURE 4.1: Schematic of the fibre tapering setup. The fibre is heated by a stationary hydrogen-oxygen flame. The translator stage moves the fibre relative to the flame while the stretcher stage moves to elongate the fibre, as indicated by the arrows. During the tapering process, the transmission of the fibre can be monitored.

taper, this mode is constantly transformed due to the fibre radius alteration. If the change in radius is significant only over a distance of several wavelengths, the mode changes adiabatically, that is, there is no coupling to higher modes, that exist in the tapered region of the fibre. To allow for an adiabatic transition, the taper of the fibre is divided in three sections as shown in figure 4.2. According to [45], the optimal taper profile for low transmission losses is a rotated “s-shape”. This profile is approximated by the three linear sections. For each section a slope angle and a final diameter is specified, so the parameters

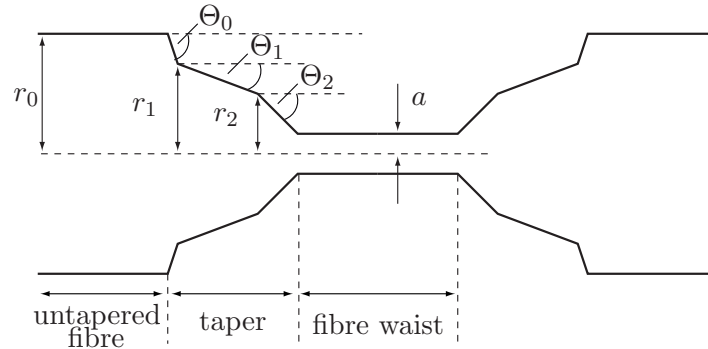


FIGURE 4.2: Schematic of the diameter profile for an ultra thin fibre consisting of the untapered fibre ends, the taper and the waist. The taper profile is determined by the starting, intermediate and end radii r_0 , r_1 , r_2 , a as well as the slope angles Θ_0 , Θ_1 and Θ_2 .

of the tapering process are the starting radius r_0 , the intermediate radii r_1, r_2 and the final waist radius a , as well as the according angles Θ_0 , Θ_1 and Θ_2 . The most crucial angle is the intermediate angle Θ_1 . Most light is lost by the coupling of the fundamental HE_{11} mode to the HE_{21} mode [27] at the transition from core to cladding. This effect is strongest in the region of a fibre radius of about $20 \mu\text{m}$, therefore the angle here should be chosen

small enough to minimize the mode coupling. It is possible to monitor the transmission of the fibre during the tapering process. To this end, laser light is coupled into the fibre and the power of the transmitted light is measured by the photodiode located at the fibre output (see figure 4.1).

The parameters used in the experiment are $r_0 = 62.5 \mu\text{m}$ (radius of the cladding), $r_1 = 45 \mu\text{m}$, $r_2 = 10 \mu\text{m}$, $a = 0.2 \mu\text{m}$ as well as $\Theta_0 = \Theta_1 = \Theta_2 = 2 \text{ mrad}$ unless mentioned otherwise. Although there is no difference in the slope angles, the transmission of the created fibres was satisfactory for our purposes.

4.2 Examination of the modes during the fibre pulling process

In order to observe the modification of the modes during the tapering process an experimental setup has been realised. It enables us to excite different modes in a fibre and to observe them during the pulling process. Since the fibre radius is altered, the propagation constants of the modes change. This is examined by observing the interference pattern of the modes during the tapering process.

Figure 4.3 shows a schematic of the setup used for the investigation of the modes during the pulling process. A linearly polarised diode laser at a wavelength of 852 nm is coupled into the fibre with a fibre coupler (ThorLabs *MAX303*). The fibre is placed onto the tapering stages (compare with figure 4.1) and the light at the fibre output is collimated via a fibre collimator (Schäfter-Kirchhoff *60FC-4-M12-10*). The modes are then observed with a CCD camera (PixeLink *PL-B741*) which is linked to a computer.

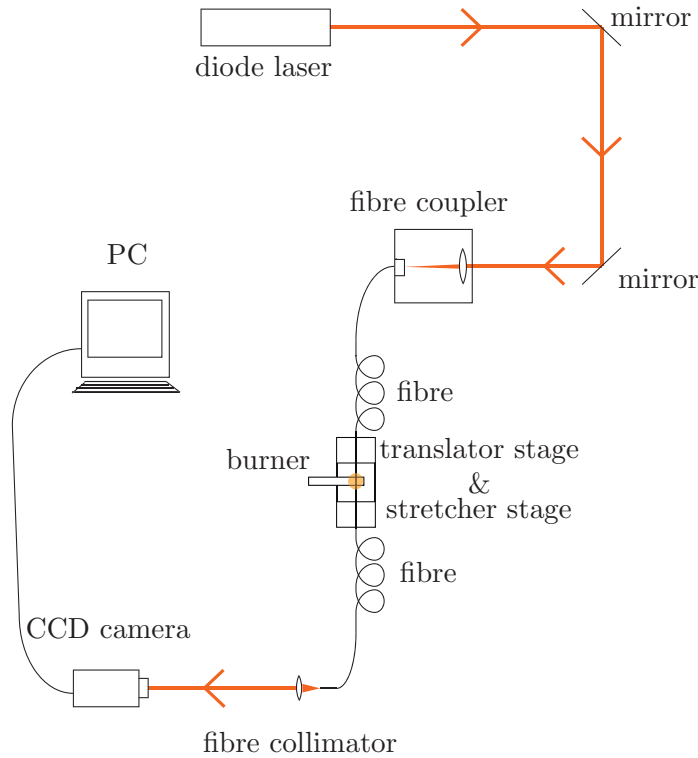


FIGURE 4.3: Schematic of the experimental setup for the examination of the fibre modes during the pulling process.

4.2.1 Intensity distribution between the different modes

In order to examine the mode propagation during the tapering process, a fibre that is multimode for the used wavelength is necessary. In the experiments a single mode fibre for light of a wavelength of 1300 nm (J-Fiber *S1260607FA*) was used. The fibre has a V parameter of $V = 2.33$ for $\lambda = 1300$ nm in the untapered part, so only the fundamental HE_{11} can propagate for this wavelength. However, as V is dependent on the wavelength (see equation 2.28), this results in a V parameter of 3.57 for a wavelength of 852 nm. Therefore, the HE_{11} , TE_{01} , TM_{01} and HE_{21} can propagate in the fibre (see figure 3.2). The relative intensity of the modes can be controlled to some extent by tilting the incident beam, when coupling light into the fibre. This stems from the fact, that optical fibres can guide light which is coupled within a range of incidence angles $\pm\gamma/2$, given by the numerical aperture NA of the fibre

$$NA = \sin\left(\frac{\gamma}{2}\right), \quad (4.1)$$

where γ is the divergence angle of the mode of highest order that can propagate through the fibre. This is depicted in figure 4.4. Modes of higher order have a larger divergence (γ_2) than modes of lower order (γ_1).

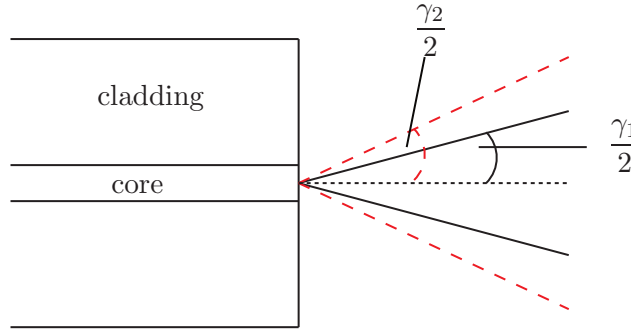


FIGURE 4.4: Divergence of two different modes at the fibre output. Shown is the core and the cladding of the fibre as well as the exit angles of two modes. Higher order modes have larger exit angles (red dashed line with exit angle γ_2) in comparison to those of a lower order (black solid line with exit angle γ_1).

If one slightly tilts the incident beam when coupling into the fibre so that the overlap with the lower order modes gets smaller, the overlap with the higher order modes increases. This results in an increased probability of exciting the higher order modes. If the polarisation directions between the incident and guided modes match, one can excite different modes almost independently. This is shown schematically in figure 4.5 for the case of the fundamental HE_{11} mode and the TE_{01} mode. Consider situation (a): The incident light beam is focussed at the centre of the core, with the optical axis as its symmetry axis, so primarily the fundamental HE_{11} mode with the respective polarisation direction will be excited (b), since the overlap of the beam with the coupling angle of the HE_{11} is maximal. In situation (c) the incident beam is coupled into the fibre under an angle. This reduces the overlap with the coupling angle for the fundamental mode which is subsequently excited less. As a result, most intensity will be guided by the higher order modes or a combination of them (d). It is important to note that this is not an exclusive process. In situation (a) the higher order modes can also be created, but with less intensity. Accordingly, in situation (b) also the HE_{11} can be created, but with significantly less intensity.

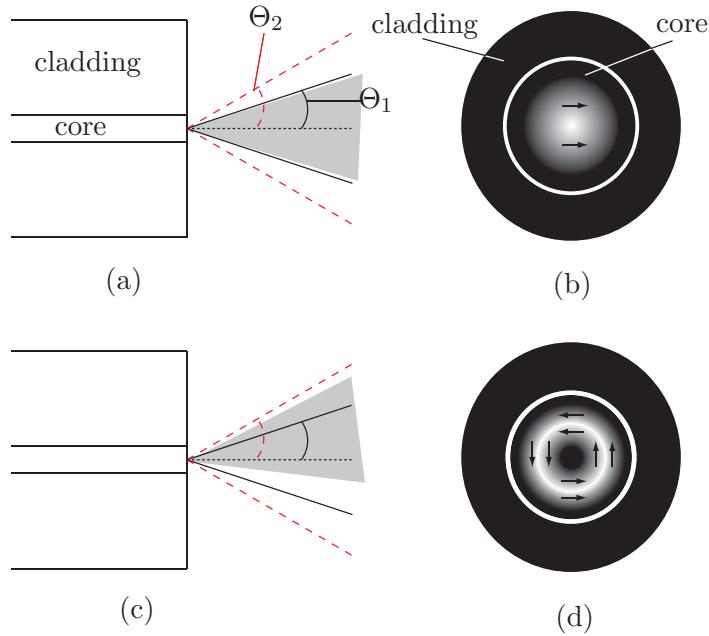


FIGURE 4.5: Excitation of higher order modes by tilting the laser beam coupled into the fibre. Depending on the polarisation direction (black arrows in (b) and (d)), different modes will be excited by focussing the light beam (grey area in (a) and (c)) under different angles.

4.2.2 Mode interference during the tapering process

Under certain circumstances, a so-called "butterfly mode" can be excited in the fibre. This butterfly mode is created, when several modes are superimposed in the fibre in such a way, that the fields cancel each other at a certain axis. For example, the linearly polarised HE_{21} mode and the TE_{01} mode (as shown in figures 2.14 and 2.19) cancel each other at the axis, that is rotated by $\pi/4$ from the vertical axis, as the field vectors point in different directions, thus creating a butterfly mode. A measurement of such an intensity pattern is displayed in figure 4.6. The presence of a butterfly mode thus proves that at least two



FIGURE 4.6: The superposition of higher order modes in a fibre creates a butterfly-shaped mode.

modes are propagating. Note, that the HE_{11} cannot form a butterfly mode with only one more mode propagating, as it does not have vanishing intensity at the centre. During the tapering process, when the core becomes too small to guide the light and the modes leave

the core and are guided by the cladding. Now, the radius of the cladding defines the V parameter (equation (2.28)) and therefore the propagation constants of the modes. When the modes are guided in the cladding, the cladding radius is still large, so the V parameter is also large. Considering figure 4.7, this means, that the propagation constants of the modes are similar and do not vary much with decreasing V parameter in region (a).

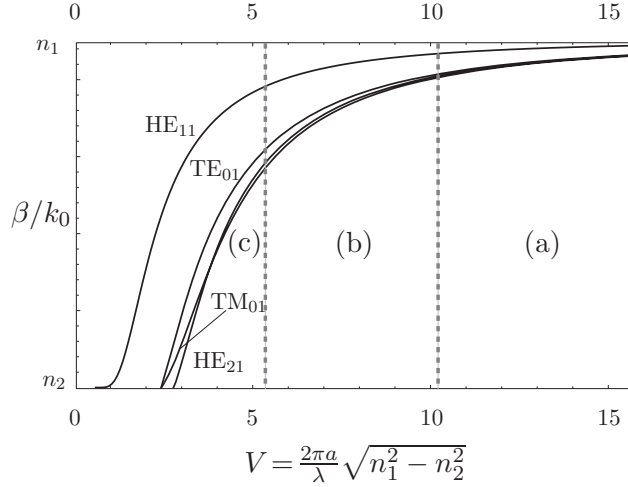


FIGURE 4.7: Propagation constants of the HE_{11} , TE_{01} , TM_{01} and HE_{21} modes. The regions (a), (b) and (c) are regions of almost no, small and large variation in the propagation constants.

During the tapering process, the V parameter decreases and the propagation constants of the modes change (regions (b) and (c) in figure 4.7). This changes their relative phase and thus the interference pattern. This is displayed for three configurations in figure 4.8. Here, the interference of the higher order modes HE_{21} , TE_{01} and TM_{01} is shown. Since the

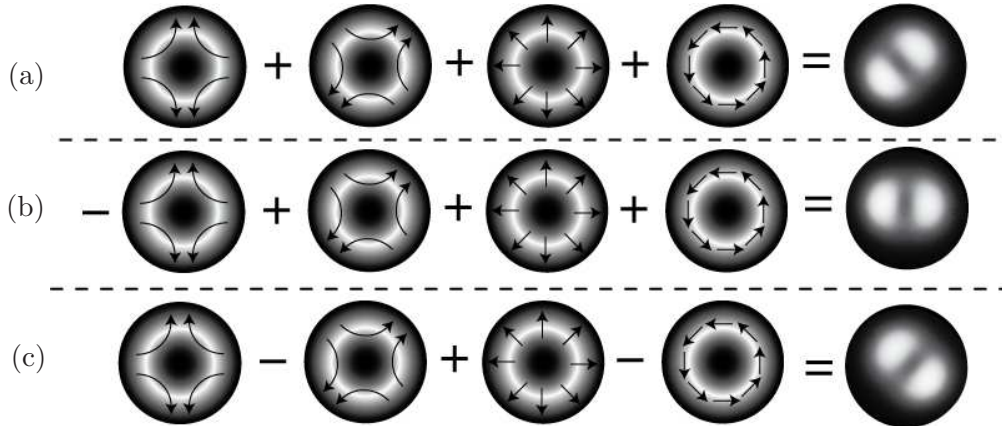


FIGURE 4.8: Superposition of modes. The arrows indicate the polarisation direction of the individual modes, bright regions indicate regions of higher intensity. The “-” signs mark a phase shift by π . The relative phase shifts causes a rotation of the resulting butterfly mode.

HE_{21} mode has two orthogonal polarisation states, both are considered. When the fibre

is tapered to radii smaller than $a \approx 1.3 \mu\text{m}$, the propagation constants of the modes for a light field of wavelength $\lambda = 852 \text{ nm}$ differ significantly (see region (b) in figure 4.7) leading to a relative phase shift of the modes. This results in a modification of the interference pattern while stretching the fibre. The butterfly mode rotates with time.

Figure 4.9 shows the modes during the tapering process of a fibre (J-Fiber *S1260607FA*) down to a waist radius of 700 nm with corresponding angles $\alpha_0 = 2 \text{ mrad}$, $\alpha_1 = 1 \text{ mrad}$ and $\alpha_2 = 1 \text{ mrad}$. Note that this is a smooth tapering that should allow to adiabatically transfer the fundamental mode into the waist [27].

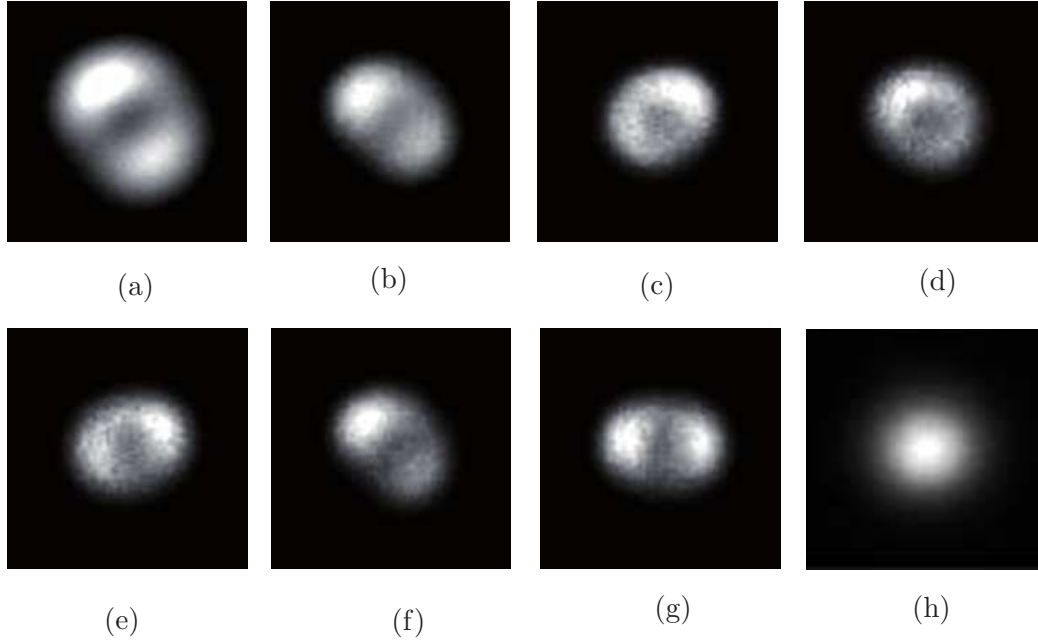


FIGURE 4.9: Pictures taken during the fibre tapering process. Note how the butterfly mode created in (a) rotates in (b) and (c) and (e)-(g). In (d), the modes interfere to form a donut-shaped mode. After completing the tapering process, only the bell-shaped fundamental mode remains (h).

The starting point is the butterfly mode in an untapered fibre (a). Picture (b) is taken after the modes have left the core and propagate in the cladding at the waist. The cladding radius is still very large, so the propagation constants of the higher order modes are thus almost constant. When the fibre radius reaches a value, where the propagation constants start to change, the butterfly mode begins to rotate (c). In (d), a donut-shaped mode is visible. The rotation is repeated (for example in (e)-(g)). The rotation is relatively slow at the beginning, but gets faster over time. This is because the smaller the fibre radius, the larger the difference between the propagation constants. Finally, the butterfly mode vanishes and only the fundamental bell-shaped mode HE_{11} is guided by the fibre waist (h). After the pulling process, when altering the polarisation of the light field, the appearance of the bell shaped mode remains unchanged, indicating that the fibre now only guides a single mode.

4.2.3 Fibre diameter examination

The results obtained from the previous section indicate, that the higher order modes are expelled from the fibre, because the V parameter becomes so small, that the fibre cannot guide them any more. However, this should happen at $V \approx 2.4$ (compare to figure 4.7), which corresponds to a fibre radius of about 300 nm for $\lambda = 852$ nm. This is the lowest fibre radius that is theoretically able to guide the light in higher modes, so reasonable propagation of the higher modes can be expected for a fibre radius of about 400 nm, that is $V = 3.1$. However, when tapering the fibre to a radius of 400 nm, the higher order modes are not guided any more. By varying the slope angles, intermediate and end radii, the modes were found to leave the fibre, when the radius was smaller than 800 nm. The variation of the slope angles does seem to have a minor affect on the modes leaving the fibre. To find the cause for this unexpected behaviour, the fibre waist radii were examined to ensure, that the fibres were tapered to the specified waist radius. This was done with a *transmission electron microscope* (TEM) [46] at the “Institut für Physikalische Chemie” at the University of Mainz and a *scanning electron microscope* (SEM) [47] at the “Center of Advanced European Studies And Research” (*caesar*), Bonn. In both cases fibres that were tapered to a waist radius a of 800 nm were examined. The results are shown in figure 4.10. The diameter of the fibre in figure 4.10(a) is determined to be (1655 ± 10) nm or a radius of (827.5 ± 5) nm. The error stems from the fact, that the image of the edge of the fibre is not sharp, so there is some inaccuracy in determining the diameter from the pictures.

The examination of the fibre at the *caesar* yields similar results. Here the fibre diameter is found to be (1579 ± 20) nm from figure 4.10(b), that is, a radius of (789.5 ± 5) nm. The larger error results again from the diffuse image of the edges of the fibre. However, the magnification is less than in figure 4.10(a), thus, the error is larger. Both results are in good agreement with the accuracy of $\pm 5\%$ of the waist radius in the fibre tapering process, mentioned in section 4.1.

In conclusion, the fibre radius seems not to be responsible for the expulsion of the modes. As a variety of fibres were used (J-Fiber *S1260607FA*, *SL270982DA* and *UL270872KA* as well as ThorLabs *1550BHP*), all yielding the same result, a manufacture error of the fibre, resulting, for example, in an altered refractive index can thus also be ruled out.

4.2.4 Minimum fibre radius for light propagation

Another approach to understand why the modes leave the fibre at such a radius is to examine the surface intensity of the TE_{01} mode with varying radius. This was already done for the fundamental HE_{11} mode [37]. It has been shown that, while the HE_{11} mode has no cutoff radius, the intensity will drop significantly when the fibre radius falls below a certain value. This is shown in figure 4.11 (a) for a light field with a wavelength of $\lambda = 852$ nm. For a large radius, the surface intensity is very low, as almost all of the intensity is guided inside the fibre, there is only a small evanescent field. When the fibre radius is comparable to the wavelength of the light, an increasing amount of power is guided in the evanescent field. However, when the fibre radius becomes too small, the mode diameter increases rapidly, so the same power is spread over a larger area. This reduces the intensity at the fibre surface. The mode is now weakly guided by the fibre as only a small fraction of the intensity is guided inside the fibre. Note the drastic decrease

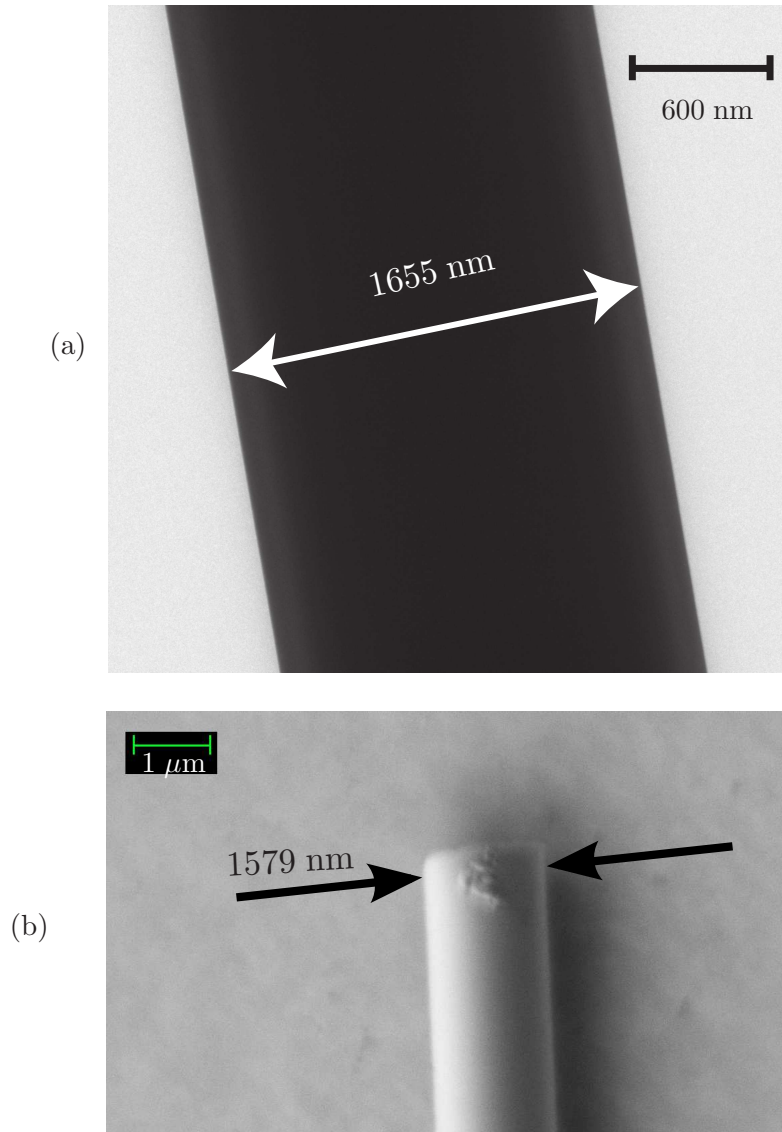


FIGURE 4.10: Electron microscope pictures of two fibre waists, that were both specified to be 1600 nm in diameter. Picture (a) was taken at the "Institut für Physikalische Chemie", Johannes Gutenberg-Universität, Mainz. Picture (b) was taken at *caesar* in Bonn.

in the surface intensity for $a < 250$ nm. To examine if this weak guiding of modes could be responsible for the loss of the higher order modes, the same calculation was carried out for the TE_{01} mode at the same wavelength. The results for this simulation are shown in figure 4.11 (b). Although the drop in surface intensity occurs at $a = 360$ nm, where the cutoff radius for the TE_{01} mode is at about $a = 300$ nm, this does not explain the observed loss of modes.

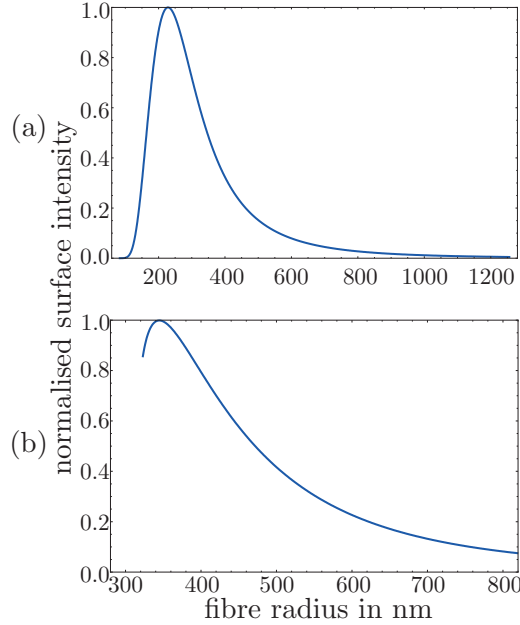


FIGURE 4.11: Normalised surface intensity over radius for the HE_{11} mode (a) and TE_{01} mode (b)

A possible explanation for the experimentally observed loss of the higher order modes was recently developed by [48]. It was shown using the theory of nonadiabatic transition [49], that for a TOF there exists a lower limit for the fibre waist diameter, which allows the fundamental mode to be adiabatically transferred from the untapered fibre into the waist. These losses are due to the presence of a nonuniformity in the fibre and the critical radius is almost independent of the length of the taper, that is, the smoothness of the transition. For a wavelength of 850 nm and a taper length $L = 10$ mm, the minimal diameter is found to be 300 nm for the fundamental mode. Experimental results obtained by [27, 50] support the theoretical predictions. However, the application of this approach to the higher order modes is not trivial and further theoretical investigation is necessary to find the cause for the loss of modes at such a fibre radius. Hence, at the present state of my research, the traps discussed in chapter 3 cannot be realised as described: A fibre with a radius of 800 nm carries a very small evanescent field, so the traps discussed in chapter 3 cannot be created with a reasonable laser power.

4.3 Investigation of the evanescent field of the HE_{11} mode

Parallel to the examination of the modes during the pulling process, an experimental setup to measure the radial, longitudinal and azimuthal variations of an evanescent field

distribution has been developed. As a first step towards examining the multimode traps discussed in chapter 3 the evanescent field of a quasi-linearly polarised HE₁₁ mode in a fibre has been examined. Instead of using a scanning near-field microscope (SNOM) [44], a setup that allows to place two fibres at a fixed relative position to each other with a precision of a few of ten nanometres has been realised. This allows to learn about the coupling mechanisms between two fibres. One fibre is used to guide the light and thus to create the evanescent field, the other fibre is used as a probe. When placed inside the evanescent field of the field fibre, some light is transferred into the probe fibre and subsequently detected at the fibre output. This section presents the experimental setup used for the evanescent coupling between two fibres and the experimental results are discussed.

4.3.1 Evanescent coupling between two fibres

In this section the process for the coupling of two fibres is briefly described. Yet the case of fibres at an angle that couple via their evanescent fields has not yet been theoretically studied. Hence, the basic process of two parallel fibres is given and the case of two fibres under an angle is qualitatively described. The power transfer between two TOFs is the result of *optical tunneling* of photons from one fibre to another. Consider the case of two identical fibres. The two fundamental solutions of the *composite waveguide* Ψ_+ and Ψ_- of the scalar wave equation are then given by the superposition of the fundamental solutions of each fibre in isolation, Ψ_1 and Ψ_2 [40]:

$$\Psi_+ = \Psi_1 + \Psi_2; \quad \Psi_- = \Psi_1 - \Psi_2 \quad (4.2)$$

with the corresponding propagation constants β_+ and β_- . In the case of unit power in fibre 1 and zero power in fibre 2 at $z=0$, the power flow in each fibre along the propagation direction $P_1(z)$ and $P_2(z)$ is given by:

$$P_1(z) = \cos^2\left(\frac{2\pi z}{z_b}\right); \quad P_2(z) = \sin^2\left(\frac{2\pi z}{z_b}\right), \quad (4.3)$$

where the beat length z_b , that is, the distance in z -direction, where the power oscillates from fibre 1 to fibre 2 and back is given by:

$$z_b = \frac{4\pi}{\beta_+ - \beta_-}. \quad (4.4)$$

For identical fibres and increasing distance, the propagation constants of the composite waveguide tend to the propagation constant of the individual fibres, $\beta_+, \beta_- \rightarrow \beta$, and thus the beat length increases. In the case of nonidentical fibres, the power flow along the propagation direction becomes:

$$P_1(z) = 1 - F^2 \sin^2\left(\frac{2\pi}{z_b F} z\right); \quad P_2(z) = F^2 \sin^2\left(\frac{2\pi}{z_b F} z\right), \quad (4.5)$$

where $F=1$ for identical fibres and $F \rightarrow 0$ for significantly differing fibres. So for nonidentical fibres, only the fraction F^2 of power is transferred, whereas for identical fibres the full power oscillates between the two fibres.

When tilting the fibres, the distance over which the fibres can couple is reduced. If the length of interaction is smaller than half of the beat length, then only a fraction of the power can be transferred from one fibre to the other. Additionally, the difference of the wave vectors in the fibres further decreases the coupling efficiency. Since the coupling efficiency depends strongly on the distance of the fibres, the main contribution to the coupling comes from the location where both fibres are closest. When two ideal fibres are in contact under an angle, they only touch at one point. Due to deviations from the perfectly cylindrical form and coupling contributions from adjacent fibre locations the coupling occurs over a small region. This can be regarded a sub-lambda source for the light coupled into the second fibre. Diffraction leads to a large divergence of the coupled beam and while most of the diffraction is in forward direction, some wave vectors match the wave vectors in the fibre, so some light is guided in the second fibre. The light that is coupled into the second fibre with a non-matching wave vector is scattered out of the fibre.

Also, the polarisation of the modes affect the coupling efficiency. In figure 4.12 the coupling of the fundamental HE_{11} mode from one fibre to another depending on the angle under which they are brought next to each other is depicted. In case (a), the polarisation direction of the HE_{11} mode is parallel to the surface at the side, where both fibres face each other. In case (b), the polarisation in the field fibre is perpendicular to the fibre surface at this side. Recall from chapter 2, that perpendicular field components show a discontinuity, increasing the evanescent field for the corresponding angle.

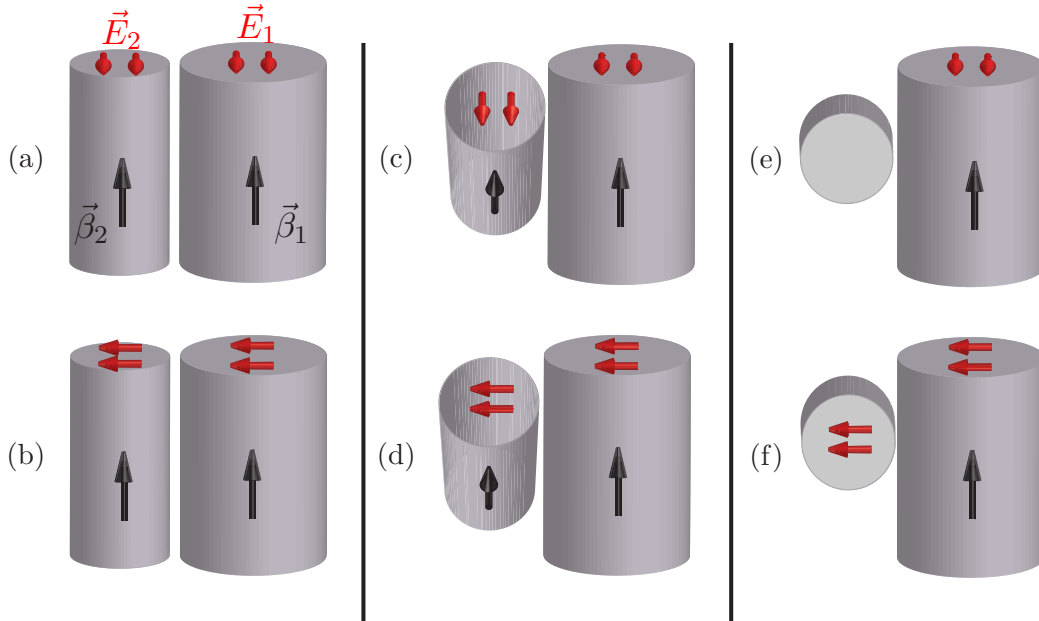


FIGURE 4.12: Coupling of the HE_{11} mode with propagation constants β_1 and β_2 and polarisation indicated by the field vectors \vec{E}_1 and \vec{E}_2 from fibre 1 to fibre 2. The coupling is dependent on the angle between the fibres.

Consider situations (a) and (b). The fibres are parallel to each other, so in both cases, the polarisation and the propagation constants can be perfectly matched and the coupling efficiency is maximal for both polarisation directions. However, $F \neq 1$, as both fibres have different diameters, so only a part of the total power is transferred.

In situations (c) and (d), the probe fibre is tilted by an angle of 45°. Now, the propagation directions do not match, resulting in a reduced coupling efficiency from fibre 1 to fibre 2. Only the light that is diffracted into the propagation direction is guided by the second fibre. This reduces the coupling between the two fibres with increasing angle. However, the polarisation direction of the field remains unchanged. In (c), the polarisation direction of the HE₁₁ in the field fibre does not match the polarisation direction of the HE₁₁ in the probe fibre. As the HE₁₁ has almost no component in its electric field along the propagation axis, the component of the polarisation of the field fibre pointing in this direction cannot cross over to the probe fibre. This further reduces the coupling efficiency for this particular polarisation direction. In (d), the polarisation direction of the mode in the probe fibre is matched with the polarisation direction in the field fibre, so no further reduction of the coupling efficiency takes place.

Increasing the coupling angle further decreases the coupling efficiency due to the decreased fraction of diffracted light along the propagation direction of the field in fibre 2. In the extreme case of a tilting angle of 90°, the propagation directions in both fibres are perpendicular. This is shown in situations (e) and (f). As a result of diffraction, light may still couple from the field fibre to the probe fibre. However, this is much more likely in (f), as again, the polarisation directions in both fibres coincide. In (e), the polarisation direction is in propagation direction of the probe fibre, so the light transition from one fibre to the other is suppressed.

4.3.2 Experimental setup

The examination of the evanescent field components of the fundamental HE₁₁ mode has been carried out using the experimental setup shown in figure 4.13. A grating-stabilised diode laser (external cavity diode laser (ECDL)) provides a laser beam at a wavelength of 851 nm with a power of up to 30 mW, that can be controlled by regulating the laser current. External feedback is avoided by using a Faraday isolator with an isolation of more than 60 dB (Linos *DLI-1*).

About 4% of the laser power is then diverted into the Fabry-Pérot arm (highlighted region (a) in figure 4.13) by a glass plate. A lens with a focal length of 100 mm improves the injection into the Fabry-Pérot cavity. The cavity transmission signal is measured by a photo diode (PD1) and displayed on an oscilloscope. The Fabry-Pérot cavity length is scanned with a piezo driven by a waveform generator at a frequency of 40 Hz. The Fabry-Pérot arm monitors if the laser diode emits at a single longitudinal laser mode. When the laser diode temperature drifts or the laser current is varied, the output may consist of more than one longitudinal mode, thus destroying the beam's coherence.

The main beam is then split up at another glass plate and about 4% of its power is guided into the Michelson-Morley interferometer [20] (highlighted region (b) in figure 4.13). The interferometer monitors the displacement of the positioning stages by superimposing the beam that gets reflected from the back of the stage with a stationary beam and detecting the modulation of the interference pattern. This is done to measure the total distance covered by the translation stage and to monitor a potential drift in the piezo.

The main beam is then coupled into the field fibre by a nanopositioning stage (Thorlabs *MAX303*). The polarisation direction of the beam can be altered via a zero order half wave plate (Lens Optics *W2Z15-852*).

The fibre couple setup (highlighted region (c) in figure 4.13) is depicted in more detail

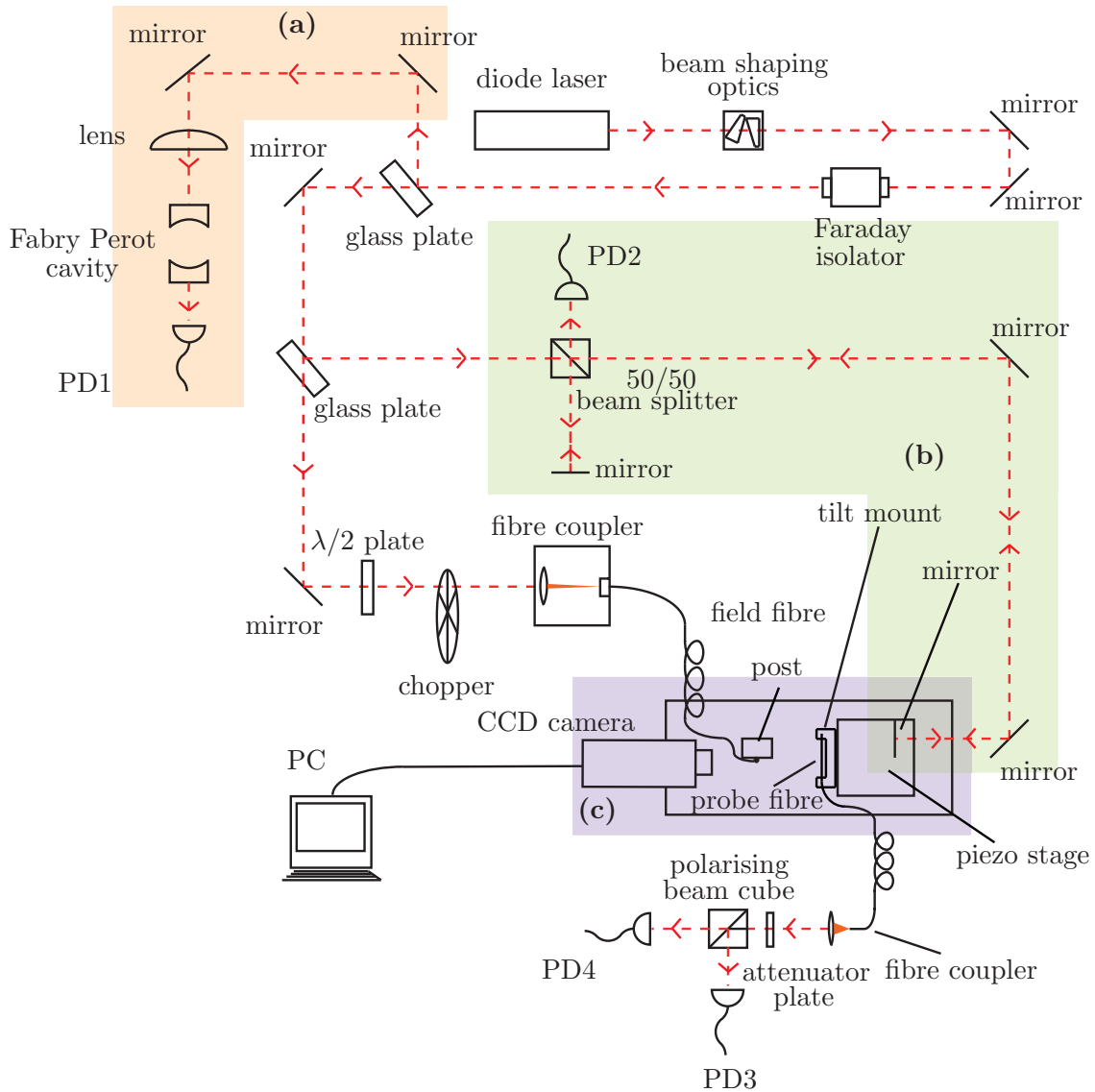


FIGURE 4.13: Schematic of the experimental setup for the examination of the azimuthal and radial component of the evanescent field of the linearly polarised HE_{11} mode.

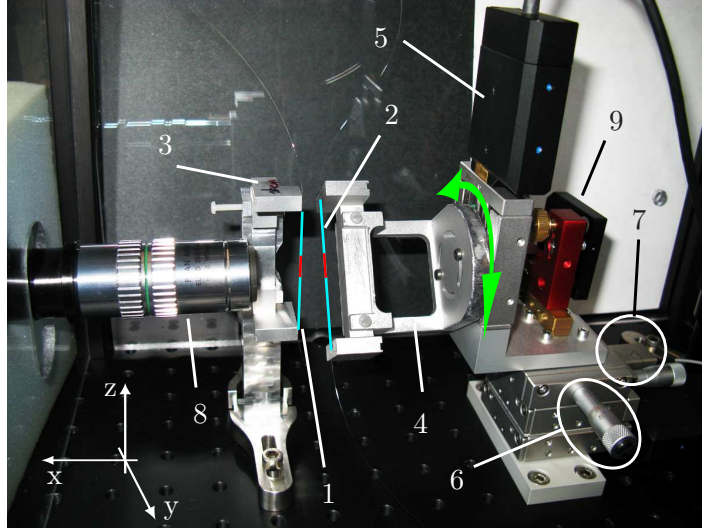


FIGURE 4.14: Fibre coupling setup. Field fibre (1) and couple fibre (2) are held by a post (3) and a specifically designed tilting holder (4) that rests on a three-dimensional translation stage. The translation in z -direction is controlled by a stepper motor (5), in y -direction via a micrometre screw (6) and in x -direction alternatively by a piezo drive for fine adjustment (7). The fibres can be monitored via a microscope setup (8). The mirror (9) is mounted on the translation stage and is part of the Michelson-Morley setup.

in figure 4.14. Field fibre (1) (Newport $F-SF$) and couple fibre (2) (Newport $F-SF$) are held by a holding post (3) and a specifically designed tiltable holder (4). The field fibre, indicated by the blue line, is tapered to a diameter of 400 nm. The fibre waist (highlighted red) is located at the center of the fibre holder. Note, that this fibre is single mode for the wavelength used here in the untapered part and the waist, hence the light in the fibre propagates in the HE_{11} mode. The probe fibre is tapered to a diameter of 300 nm and mounted on a fibre holder that can be tilted to any desired angle. The fibre holder is fixed on a positioning stage setup consisting of three translation stages (PI $M-105$), that allows the three-dimensional displacement of the fibre. For the measurements, the fibre waists have to be at a submicrometre distance. The translation in z -direction is controlled by a stepper motor (5) (PI $M-232$), in y -direction via a micrometre screw (6) (PI $M-655.00$). Both directions do not require very much accuracy, as the fibre waist is 3 mm in length, so the accuracy reached by the micrometre screw ($0.1 \mu\text{m}$) and the stepper motor (minimal step size: $0.05 \mu\text{m}$) are sufficient. The movement in x -direction is more critical, as the evanescent field decays quasi-exponentially within a few hundred nanometres. Thus a piezo driven positioning stage (PI $P-854.00$) (the piezo is highlighted in 4.14 (7)) is used to approach the field fibre with the probe fibre. The piezo stage is connected to a piezo controller (PI $E-503$ piezo amplifier) and has a total travel range of $25 \mu\text{m}$ at a resolution in the subnanometre regime. The fibres can be monitored with a microscope setup (8), consisting of an infinity-corrected microscope objective (Edmund Optics $M PLAN APO 100\times ULWD$) that images the fibres via a tube (Infinity Photo-Optical *Infinitube Standard*) on a monochrome CCD camera (PixeLink $PL-B741$). The mirror (9) is mounted on the translation stages (PI $M-105$) and is part of the Michelson-Morley setup. When the probe fibre is placed inside the evanescent field of the field fibre, the light can be transferred from

the field fibre to the probe fibre and is guided to a detection setup. The detection setup here consists of a polarising beam splitter cube and two photo diodes (PD3 and PD4), so the polarisation of the light coupled into the probe fibre can be analysed. However, this particular feature has not been used throughout the experiments, only the sum of the two signals is used. To improve the signal, the beam is sent through a chopper and the oscilloscope that displays the diode signals is operated in AC mode. This creates a rectangular voltage output, with the amplitude of the signal corresponding to the probed intensity.

4.3.3 Azimuthal investigation of an evanescent light field

First, the azimuthal component of the evanescent field of the linearly polarised HE_{11} is examined. As previously discussed (compare figure 2.10), the intensity distribution of the quasi-linearly polarised HE_{11} mode depends on the azimuthal angle. In order to examine this dependence, the two fibres are brought into contact. This offers two advantages: Firstly, the distance remains constant during the measurement. The fibres oscillate due to air movement or sounds and hence change their relative distance. When brought into contact, the fibres stay together due to the van der Waals force and thus the fluctuation in the coupling is minimal. Secondly, the evanescent field is strongest on the surface of the fibre, so by bringing the fibres in contact, the output signal of the probe fibre is maximised.

The azimuthal dependence of the field can be examined by rotating the polarisation direction of the guided mode. This is achieved by rotating the half-wave plate in front of the fibre couple stage (compare with figure 4.13). A rotation of the wave plate by $\pi/4$ results in a rotation of the polarisation by $\pi/2$. The measurement has been performed for two different coupling angles α_1 and α_2 , that is, two different tilt angles of the probe fibre with respect to the field fibre. The angles can be determined from figure 4.15.

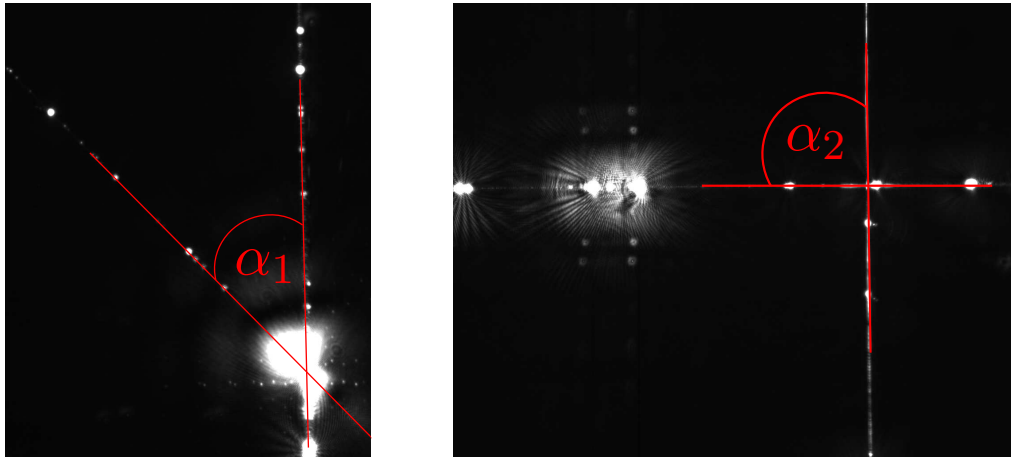


FIGURE 4.15: Angle between the field fibre (vertical) and the probe fibre. The angles are determined to $\alpha_1 = 43^\circ \pm 1^\circ$ and $\alpha_2 = 90^\circ \pm 1^\circ$.

Here, the fibres are visible by light scattering at impurities (for example dust particles) on the fibre surface along the fibre waist. In figure 4.15 the bright spot, where the fibres cross is caused by coupled light. If the light tunneling from the field into the probe fibre has no matching propagation constant for the probe fibre, it is scattered out of the fibre.

That this is indeed an evanescent effect and not caused by the disturbance at the surface of the field fibre is evident from the fact, that the bright region appears, before the fibres touch. There is no bright spot in the figure with a coupling angle of 90°, as the fibres are separated by several hundred nanometres. The probe fibre is visible, because light from a laser pointer is propagating in the waist and scattered at the impurities.

The solid lines highlight the fibre axes and are used for determining the coupling angle, which are measured to be $\alpha_1 = 43^\circ \pm 1^\circ$ and $\alpha_2 = 90^\circ \pm 1^\circ$.

The results of the polarisation dependent coupling measurements are shown in figure 4.16. The indicated errors result from reading the display of the oscilloscope and is

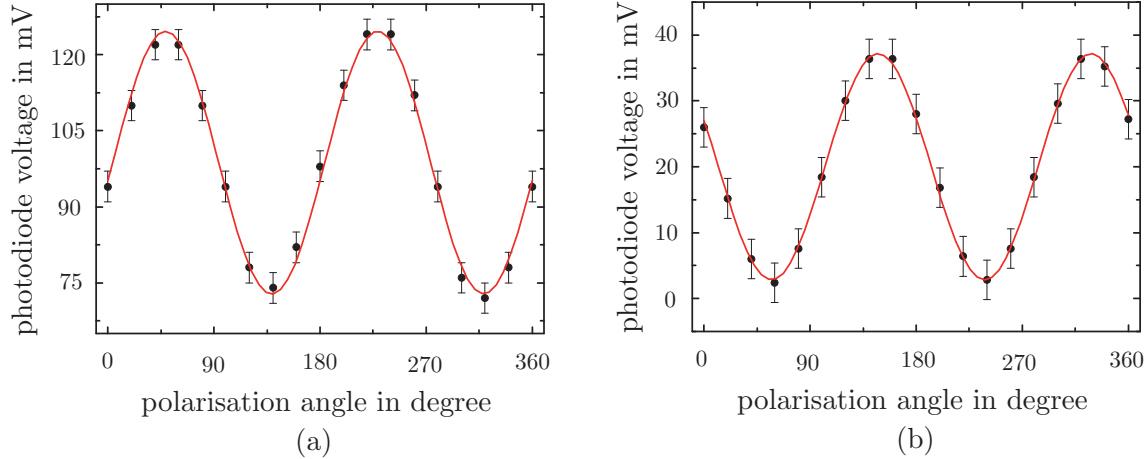


FIGURE 4.16: Measured signal by the photodiode at the fibre output versus the polarisation angle for a coupling angle of $\alpha_1 = 43^\circ$ (a) and $\alpha_2 = 90^\circ$ (b). The solid lines are fits with a sinusoidal function.

estimated to be ± 3 mV. However, this assumption overestimates the error, as almost all of the data points are on the fit curve. The expected sinusoidal modulation is verified by fitting a sine function of the form

$$f(x) = A \sin\left(\frac{\pi(\phi - \phi_c)}{\omega}\right) + B, \quad (4.6)$$

where A constitutes the amplitude of the modulation, ϕ_c is a phase, ω describes the modulation and B denotes the voltage offset. The fit parameters in the case $\alpha_1 = 43^\circ$ are found to be $A = (86.41 \pm 1.87)$ V, $\phi_c = 2.13 \pm 0.53$, $w = 44.93 \pm 0.23$ and $B = (329.01 \pm 1.29)$ V. The fit parameters for the second case $\alpha_2 = 90^\circ$ are $A = (17.16 \pm 0.18)$, $\phi_c = 51.25 \pm 0.17$, $w = 45.18 \pm 0.12$ and $B = (20.00 \pm 0.13)$. The signal in the perpendicular case $\alpha_2 = 90^\circ$ is much weaker than in the case of $\alpha_1 = 43^\circ$, as the wave vector of the field in the field fibre is almost perpendicular to that in the probe fibre, which supports the previously discussed considerations. The minimal voltage is almost zero, as in this case, the polarisation of the light field does not match the polarisation of the guided modes in the probe fibre. The values for the nonperpendicular case were taken by using a 30% transmission filter to avoid saturation effects of the photodiodes PD3 and PD4. Therefore the voltage values in figure 4.16 have been multiplied by 10/3. The shift of the maxima and minima is not an effect of the different coupling angle, but is based on the fact that the data was taken several weeks apart. During this time, the setup was modified and the fibre was replaced,

so the polarisation direction of the beam changed. In the case of a coupling angle of $\alpha_1 = 43^\circ$, the maximum signal is found for a polarisation angle of 50° and the minimum at 140° accordingly. Analogously the maximal and minimal signal for the perpendicular coupling angle α_2 is obtained for a polarisation angle of 150° and 60° , respectively. Note, that these polarisation angles are not absolute values, but are given with respect to the scale on the half-wave-plate that is used to rotate the polarisation.

4.3.4 Radial investigation of the evanescent light field

The examination of the field in azimuthal direction can be utilised to examine the radial decay of the evanescent field. By selecting the polarisation direction of maximal couple output, the photodiode signal can be optimised. In this subsection, the measurement of the evanescent field and the experimental determination of the decay length of a linearly polarised HE_{11} mode is presented. Two approaches have been used, the advantages and disadvantages of which are discussed.

The first possibility is to reduce the distance between the probe fibre and the field fibre by manually varying the piezo voltage while running the oscilloscope in AC mode. The chopper is used during the execution of this scheme. The voltage that corresponds to the coupling is taken manually by using the oscilloscope cursors.

The second approach uses the oscilloscope in DC mode without the chopper. Now, the position of the probe fibre is varied using a triangular voltage signal created by a function generator that drives the piezo. This constantly increases and decreases the distance between the fibres and thus the acquired photodiode signal decays proportionally to the quasi-exponential decay of the evanescent field. The measured data is then saved using a digital storage oscilloscope and evaluated with a computer.

The manual method has the disadvantage that it takes longer than the triangular voltage method. As the piezo is subject to drifts, the distance of the fibres change during measurement. On the other hand, the total scanned distance and in particular the location of fibre contact can be determined with good accuracy.

The triangular voltage method swaps the advantages and disadvantages. As the movement of the fibre is much quicker than the piezo drift, the change in the relative distance between the fibres during one measurement is negligible. On the other hand, the probe fibre cannot be placed too close to the field fibre, since the fibres must not touch during the measurement, otherwise the van der Waals forces between the fibres cause them to stick together until separated manually. This larger distance between the fibres reduces the coupling efficiency. This is especially problematic since in this scheme the region of highest intensity is the spot, where the piezo changes its direction of movement. This leads to the largest signal being the least reliable.

The manual method has been used to determine the propagation constant in the case of the coupling angle $\alpha_1 = 43^\circ$, while both approaches were tested for the measurement with $\alpha_2 = 90^\circ$. The coupling efficiency in the latter case seems to be too low for the manual method, that is, the piezo drifts too quickly, as the fibres touch almost instantaneously when receiving a signal, so the acquisition of data was difficult: The manual approach requires a longer measurement time, which is difficult to realize due to the piezo drift. Moreover, the 90° configuration requires that the fibres are very close to each other to have a good signal. This increases the probability that the fibres stick together. Such a configuration would thus require a higher magnification of the photodetector signal.

First, the determination of the decay length via the manual method for a coupling angle of $\alpha_1 = 43^\circ$ is presented. The piezo voltage is converted into translation by using the calibration of the piezo movement (see appendix B). The measurement was done for the polarisation direction that results in maximal and minimal coupling, $\phi_1 = 50^\circ$ and $\phi_2 = 140^\circ$, respectively (compare to figure 4.16). The evanescent decay for ϕ_1 is shown in figure 4.17. The errors are estimated from the fluctuations of the signal on the oscilloscope. The data is fitted with a curve of the form

$$f_{\text{fit}} = g_{\text{out}} K_0^2(qr), \quad (4.7)$$

where g_{out} corresponds to the coupling strength of the fibres, r is the distance of the probe fibre's surface to the centre axis of the field fibre, K_0 is the modified Bessel function of second kind of order zero and $1/q$ is the decay constant of the evanescent field. Equation (4.7) corresponds to the intensity of the LP₀₁ mode, which is an approximation to the HE₁₁ mode [18].

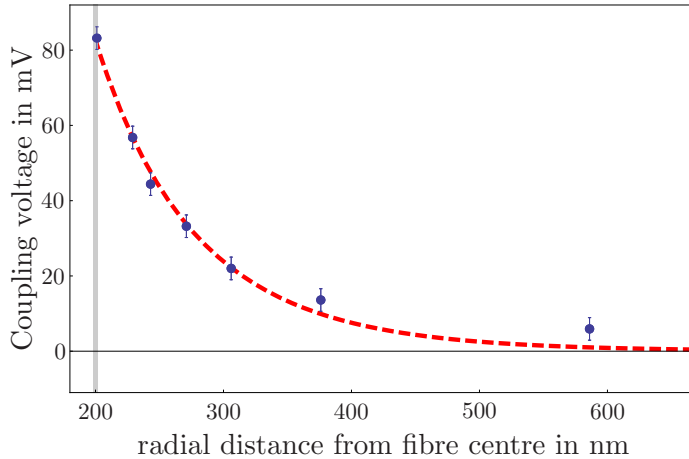


FIGURE 4.17: Evanescent coupling of two fibres with the manual method at the polarisation angle $\phi_1 = 50^\circ$ and a coupling angle of $\alpha_1 = 43^\circ$. The dots are the experimental data, the dashed line is the fitting curve. The fitting parameters are calculated to be $1/q = 224$ nm and $g_{\text{out}} = 0.34$ V.

The decay constant is found to be $1/q = 224 \pm 25$ nm. The error is estimated by visual judgement, when varying the parameter q . Note, that the photodiode voltage has been multiplied with $10/3$ to compensate for the attenuator plate in the setup. When comparing the voltage at the fibre surface in figure 4.17 to that in figure 4.16 (a) at the polarisation angle $\phi_1 = 50^\circ$, it decreased by almost a factor of two. This is due to the contamination of the fibre waist with dust. At these locations light is scattered out of the fibre, decreasing the transmission of the fibre.

Figure 4.18 shows the decay of the evanescent field for a polarisation angle $\phi_2 = 140^\circ$ that results in minimal coupled intensity between the couple and the probe fibre. After applying a fit of the form equation 4.7, the decay length is found to be $1/q = 383 \pm 25$ nm, and again, the photodiode voltage has been multiplied with $10/3$ to compensate for the attenuator plate. Again, the field strength is decreased in comparison to 4.16 (a), due to dust particles on the fibre. A comparison of the results is given after the discussion of the triangular voltage method.

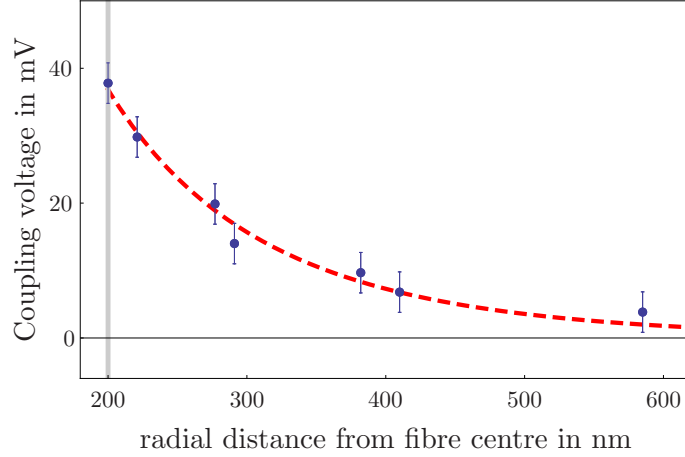


FIGURE 4.18: Decay of the evanescent field of a linearly polarised HE_{11} mode with the manual method at the polarisation angle of minimal coupling $\phi_2 = 140^\circ$ at a coupling angle of $\alpha_1 = 43^\circ$. The data is fitted with the dashed line. The fitting parameters are calculated to be $1/q=383$ nm and $g_{\text{out}}=0.15$ V.

Now, the results for the triangular voltage method for a coupling angle of $\alpha_2 = 90^\circ$ are presented. The time dependence of the photo diode signal has to be converted into a dependence of the radial distance between the two fibres. The total distance covered by the piezo movement can be calculated by taking the amplitude of the frequency generator output voltage and convert it into displacement by using the piezo calibration (equation B.2). The relative position between the two fibres is determined by bringing both fibres in contact by manually regulating the piezo voltage and then convert this voltage into distance. Let the amplitude of the piezo voltage be A , the static piezo voltage without running the frequency generator U_{stat} , the piezo voltage at fibre contact U_{cont} and the conversion coefficient k . Thus the point of smallest distance between the fibres d (that is, the turning point of the piezo) is determined by

$$d = (U_{\text{stat}} - A - U_{\text{cont}}) k \quad (4.8)$$

Experimentally, the fibres are farthest apart at the maximal piezo voltage. When the voltage is decreased, the probe fibre is brought nearer to the field fibre. Thus the amplitude A has to be subtracted from the static voltage U_{stat} to get the voltage when the fibres are closest. Note also that U_{cont} is the biggest source for errors in equation (4.8). As the piezo is subject to drifts over the course of the whole measurement the error for this quantity has to be chosen large enough. The measurement has been executed for the polarisation direction of largest and smallest evanescent field, using the polarisation angles $\phi_3 = 150^\circ$ and $\phi_4 = 60^\circ$, respectively (compare with figure 4.16).

The measurement for $\phi_3 = 150^\circ$ is presented in figure 4.19. Here, the detected signal at the fibre output is plotted versus the radial distance from the fibre centre. The solid line shows the experimental data, the dashed line depicts the fitted function given by equation (4.7). With $U_{\text{stat}} = 49.82$ V, $A = 2.2$ V and $U_{\text{cont}} = 47$ V, d is computed to be 156 ± 30 nm. The decay length is then found to be $1/q = 258 \pm 6$ nm. The error for the distance of the fibres Δd takes into account the piezo drift, which is the largest error source for the experiment. The error for $1/q$ is obtained by calculating the values for the

maximal and minimal distance $d + \Delta d$ and $d - \Delta d$.

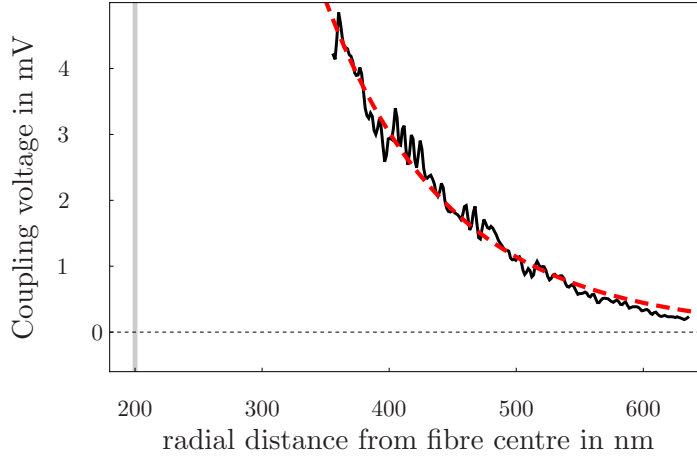


FIGURE 4.19: Evanescent coupling of two fibres with the triangular voltage method at $\phi_3 = 150^\circ$ and a coupling angle of $\alpha_2 = 90^\circ$. The solid line is the measured data, the dashed line is the fitting curve. The grey line indicates the fibre surface. The decay length is calculated to be $1/q = 258 \pm 6$ nm.

The measurement for $\phi_4 = 60^\circ$ is presented in figure 4.20. Again, the coupling voltage is plotted versus the radial distance from the fibre core. With $U_{\text{stat}} = 48.68$ V, $A = 2.2$ V and $U_{\text{cont}} = 45.8$ V, d is calculated to be 221 ± 40 nm. The decay length is found to be $1/q = 292 \pm 7$ nm. The error is obtained as before.

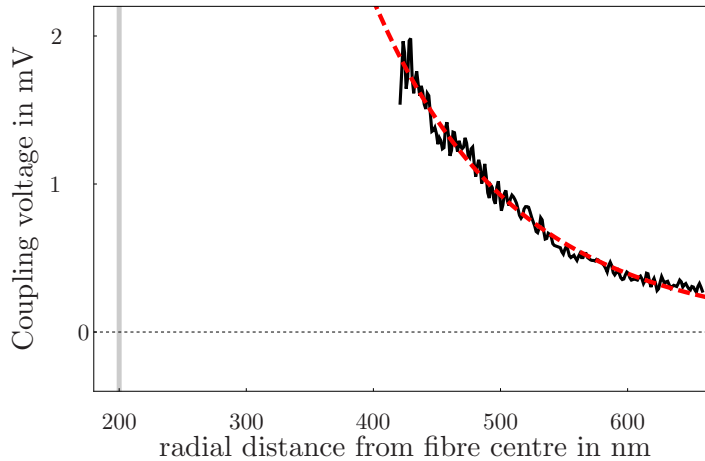


FIGURE 4.20: Evanescent coupling of two fibres with the triangular voltage method at a polarisation angle $\phi_4 = 60^\circ$ and a coupling angle of $\alpha_2 = 90^\circ$. The jagged line is the measured data, the dashed line is the fitting curve. The fitting parameters are calculated to be $1/q = 292 \pm 7$ nm and $g_{\text{out}} = 0.035 \pm 0.015$ V.

During the measurement, the detected signal is not constant, but fluctuates in irregular intervals. This can be attributed to the piezo drift and movement of the field fibre waist caused by air motion. To make the two discussed measurement comparable, the photodiode signal was monitored over a longer period of time. The data shown in figures 4.19

and 4.20 was taken when the signal returned to the initial value that was obtained when regulating the piezo voltage. Here, it is assumed, that the piezo drift is then negligible. Since the value was estimated by visual judgement, this is another error source.

The absolute value of the quantity g_{out} is not relevant for our purposes, as it is dependent on the coupling between the fibres, which is not theoretically known. Also, the laser was not temperature stabilised, so between measurements, the laser current had to be adjusted to ensure that the laser was running at a single longitudinal mode. Changing the laser current affects the laser intensity and thus g_{out} . Therefore the fitting values are not given.

The decay constant $1/q$ is independent of the laser intensity and of the coupling efficiency. The determined decay constants of the evanescent field of the HE_{11} using the two methods are given in table 4.1. The comparison between the theoretical and experimental values of the decay length $1/q$ of a quasi-linear HE_{11} mode in a fibre of 200 nm radius ($1/q = 355 \pm 40$ nm) shows, that the values have a maximal deviation of 40% from the theoretical value. The error for the theoretical value is estimated by calculating the decay length for fibre radii with a 5% deviation from 200 nm. The magnitude of the error can be attributed to the fact, that the radius of the fibre is in a regime, where a small variation results in a steep increase or decrease in the diameter of the HE_{11} mode (compare to figure 4.11(a)). The manual method works best for large output signals, but is tedious for small signals. Here, the triangular voltage method is the better option.

	$\alpha_1 = 43^\circ$		$\alpha_2 = 90^\circ$		theoretical value
	manual method		triangular voltage method		
$1/q$ in nm	$\phi_1 = 50^\circ$	$\phi_1 = 140^\circ$	$\phi_3 = 150^\circ$	$\phi_4 = 60^\circ$	
	224	383	258 ± 6	292 ± 7	355 ± 40

TABLE 4.1: Comparison of the decay constant of the evanescent field of a HE_{11} mode for different measurement methods at different contact angles α and different polarisation angles ϕ .

4.3.5 Longitudinal investigation of the evanescent light field

The traps discussed in chapter 3 offer confinement in azimuthal, radial and axial direction. While sections 4.3.3 and 4.3.4 deal with the investigation of the azimuthal and radial component of the evanescent field, this section will examine the modulations of the field in axial direction.

For this purpose the setup shown in figure 4.13 is modified to accommodate a standing wave in the fibre. When two beams of the same frequency and the same amplitude counter-propagate in the fibre, they form a standing wave pattern. For a one-dimensional propagation along the z -axis the electric field $E(z, t)$ resulting from the superposition of two fields with amplitude E_0 , propagation constant β and frequency ω is given by

$$E(z, t) = 2E_0 \sin(\beta z) \cos(\omega t). \quad (4.9)$$

Hence, the intensity distribution along the z -axis is modulated as

$$I \propto E^2 \propto E_0^2 \sin^2(\beta z). \quad (4.10)$$

Note that this only strictly holds, when the z -component of the electric field is negligible. This is the assumption used in the following. The light fields form a standing wave pattern in the field fibre. When the probe fibre is brought next to the field fibre, the coupling between the two fibres depends on the probe fibre position along the field fibres waist. This is shown in figure 4.21. When the probe fibre is located at the position of an antinode in the coupling fibre (figure 4.21 (a)), the intensity has a finite value and some light will be coupled into the probe fibre. In case figure 4.21 (b), the probe fibre is placed on a node in the field fibre. In these locations, the intensity is zero, so no light is coupled into the probe fibre.

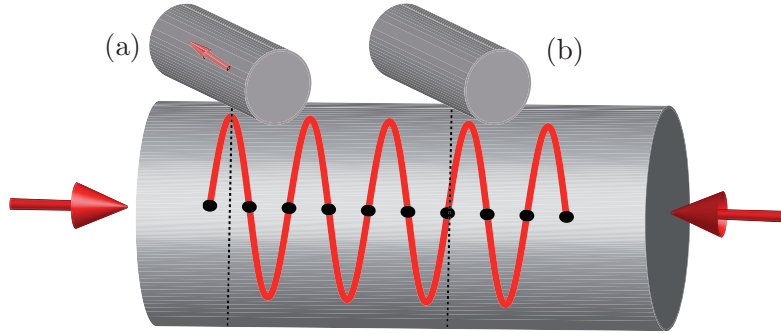


FIGURE 4.21: Coupling of light from the standing wave pattern in the field fibre. In situation (a), the probe fibre is located at an anti-node of the fibre, thus the outcoupled intensity is at a maximum. In situation (b), the probe fibre is placed on a node, so no light is coupled into the probe fibre.

The modification of the setup can be seen in figure 4.22. The dark highlighted area is the standing wave setup. The incident beam is split and the both beams are brought into the same field fibre by two fibre couple stages (Thorlabs MAX303). The rest of the setup remains unchanged as shown in figure 4.13.

As both arms of the standing wave pattern are not actively phase stabilised, the standing wave pattern moves along the fibre waist, due to phase shifts resulting from vibrations or drifts of the optical setup. However, this drift happens on the scale of a few seconds, so the standing wave pattern can be analysed, as long as the signal is acquired on a shorter time scale than the drift. In this setup the fibre is squeezed by a razor blade that is mounted on a moving membrane that is driven up and down by a triangular voltage signal of frequency $f = 5$ Hz. The squeezing of the fibre modifies the refractive index in this part of the fibre thereby changing the optical path length of the light coming in from this side. This causes a phase shift between the two counter-propagating beams that displaces the standing wave. To observe the effect of the squeezing, the probe fibre is brought into contact with the field fibre. This is again to maximise the coupling efficiency and has the additional advantage, that both fibres stay at a fixed distance and have a fixed relative position. The result is shown in figure 4.23. In (a), both beams are coupled into the fibre and create the standing wave pattern. The alteration of the signal stems from the compression and release of the fibre. When the optical path length is varied, one would expect a sinusoidal modulation of the signal, however, the modulation caused by squeezing the fibre is highly non-linear leading to a non-sinusoidal pattern. In (b) the

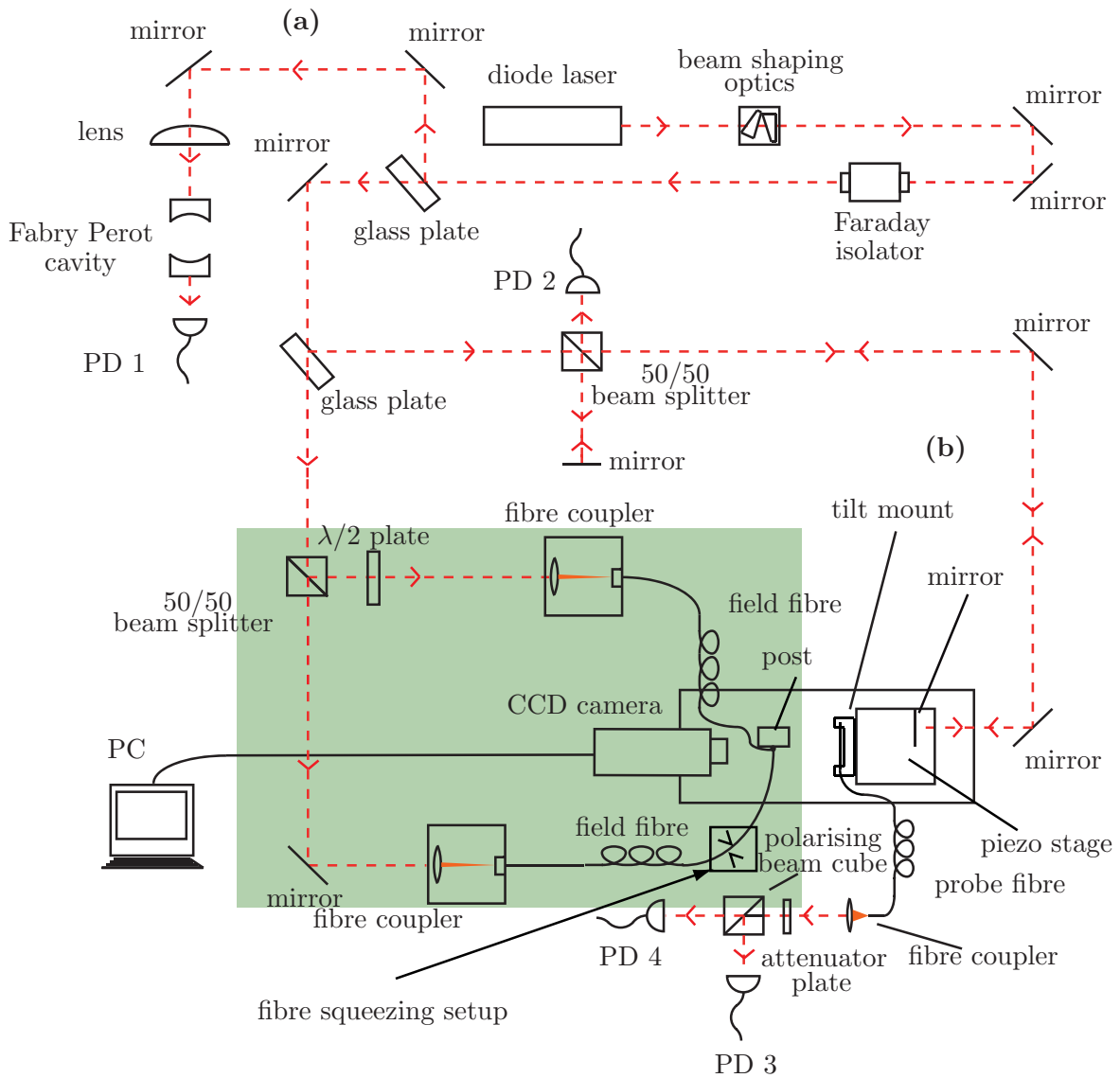


FIGURE 4.22: Schematic of the experimental setup for the longitudinal examination of an evanescent field. The darker highlighted region shows the setup's modification in comparison to figure 4.13 to create a standing wave.

same signal is depicted, but this time with either one of the arms blocked from entering the field fibre. The signal is constant, confirming, that the modulation of the signal is indeed caused by the interference of two counter-propagating beams.

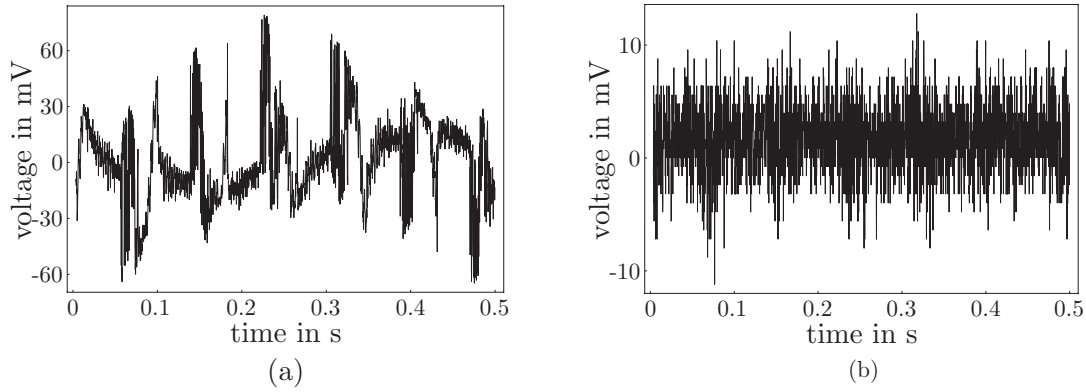


FIGURE 4.23: Collected data from the standing wave setup in AC mode. In (a), both arms are coupled into the fibre. In (b) one beam is blocked from the fibre. The coupling angle between the fibres is 43° .

This measurement offers a qualitative proof, that the setup is able to observe modulations of the field along the axial direction. Preparations for a more precise characterisation of the field in axial direction have been made and are discussed in chapter 5.

5 Summary and Outlook

Throughout the course of this thesis it has been theoretically shown that an array of microtraps for cold neutral atoms outside of the waist of an ultra thin fibre can be created by the interference of the evanescent fields of the pairwise co-propagating transverse fibre modes HE_{11} , TE_{01} and HE_{21} . The three possible trap configurations offer confinement along the axial direction due to the difference in the propagation constants, radial confinement due to different decay constants and azimuthal confinement due to the different polarisations of the modes. The trapping sites offer a trap depth of 1 mK at about 150 nm from the fibre surface. For the example of caesium atoms with a kinetic energy corresponding to 100 μ K the trapping lifetime exceeds 100 s for any of the discussed traps.

To verify the theoretical predictions concerning the mode interference, a setup to examine the evanescent field around an ultra thin fibre has been developed and realised. It was shown that the azimuthal, radial and axial dependencies of the evanescent field can be resolved. A quantitative measurement of the axial dependence of the evanescent field could be done by moving a standing wave pattern via a frequency offset in the counter-propagating beams and to evaluate the signal with a two phase lock-in amplifier. Most critical during the measurement is controlling the radial distance of the two fibers, that move due to air motion and drifts. The oscillations due to acoustic noise could be minimized by providing the fibre holders with piezo elements, that tighten the fibre and thus tune the resonance frequencies away from the ambient noise sources. Additionally, the piezo drift could be minimised by a closed loop scheme, that controls the piezo voltage to compensate the piezo motion.

To examine the behaviour of higher order modes in a fibre, an experimental setup for monitoring the modes during the tapering process has been developed. It was found that the higher order modes could not be efficiently transmitted through tapered fibres with a waist radius exceeding the theoretical cutoff radius by a factor of two. This behaviour has to be investigated more. One possible theoretical approach might be the extension of the nonadiabatic transition model discussed in [48] for higher order modes. Experimentally, further variation of the fibre profile could improve the transmission of higher order modes.

An additional challenge in the process of creating the multimode traps is the excitation of the higher order modes. In this thesis it has been demonstrated that by tilting the incident beam with respect to the fibre axis, the intensity distribution between the modes can be influenced. However, with this scheme the relative intensity between the modes inside the fibre cannot be controlled accurately. A more promising alternative is to create the modes outside of the fibre with a given intensity. For this purpose, the Gauss-Laguerre modes, that correspond to the desired fibre modes would have to be created and then coupled into the fibre. The controlled creation of arbitrary Gauss-Laguerre modes was demonstrated in [51]. Another method of mode generation was recently discovered in our group. Fibre-based microresonators can be tuned to transmit only the desired mode. These modes could then be coupled into the tapered fibre with a controlled intensity distribution.

Controlling single atoms is a key interest in many fields, for example quantum infor-

mation processing. The realisation of the multimode trap could provide a tool to trap single atoms very close to the fibre surface in low or zero intensity regions. This might allow to overcome an important experimental drawback traps using red detuned light, that is, the light shift of the energy levels, that has to be considered in red detuned dipole traps [19, 52]. This would also open the route towards studying the atom-surface interaction, as for example the van der Waals interaction in a controlled environment.

A Energy level diagram for Caesium

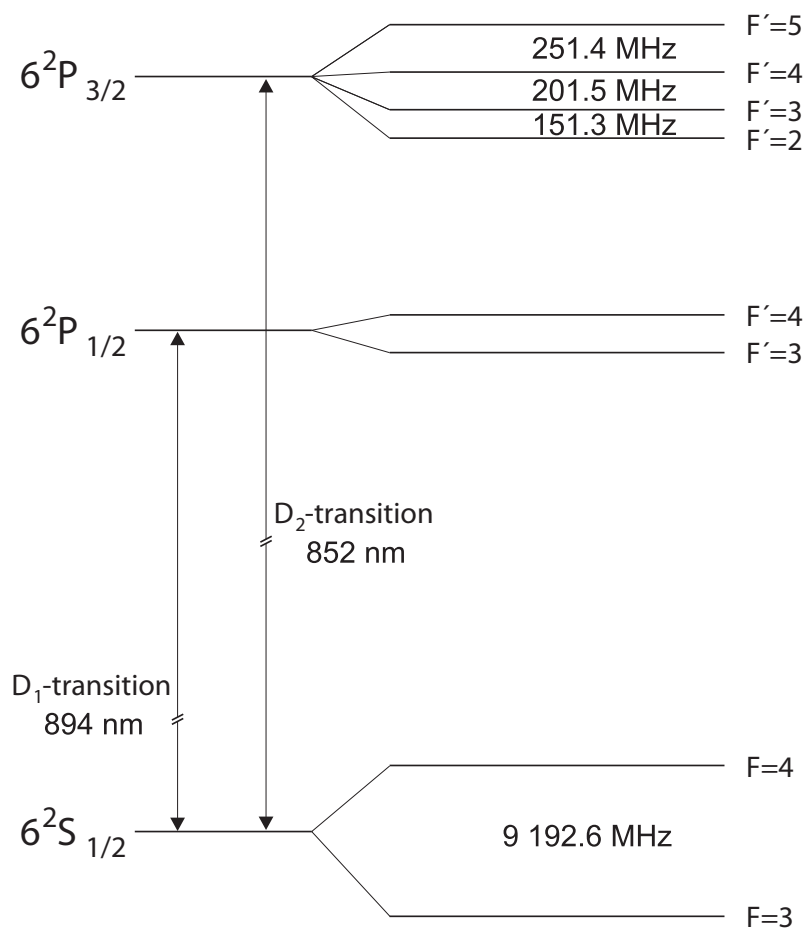


FIGURE A.1: Energy level scheme for ^{133}Cs

B Piezo calibration

The fine adjustment of the fibre's distance is controlled by a piezo translation stage. In order to determine the travel distance as a function of the piezo voltage, the Michelson-Morley interferometer setup is used (highlighted region (b) in figure 4.13). The piezo stage is driven by a function generator, lengthening and shortening the corresponding interferometer arm. The condition for constructive interference of both arms is that the optical path difference has to be an integer multiple of the used wavelength. As the beam is reflected onto itself, the distance that is covered between two occurring maxima is half the wavelength. This yields for the output intensity I at the location of interference:

$$I \propto \cos^2\left(\frac{4\pi\Delta d}{\lambda}\right), \quad (\text{B.1})$$

where $2\Delta d$ is the optical path difference between the two beams and λ is the wavelength of the light.

For the calibration, the piezo is driven by a triangular voltage of known amplitude ΔV from a frequency generator with a given frequency f . From equation (B.1) follows, that the periodicity of the output signal is $\lambda/2$, so by counting the number of intensity maxima N that occur during the time period $T = 1/f$ the distance that is covered is $s = N\lambda/2$. The result is shown in figure B.1. The translation as a function of applied voltage is found by fitting a line to the linear part of the curve. The errors result from the fact, that the voltage signal does not start and end with a maximum, so there is an error in the number of intensity maxima of $\Delta N = 1$. The voltage data is evaluated electronically, so the errors in voltage and frequency are limited by the accuracy of the oscilloscope and the frequency generator ($\delta V = 0.1$ V, $\Delta f = 1$ Hz). The error in wavelength is estimated to be $\Delta\lambda = \pm 0.1$ nm). This yields a conversion coefficient of $k = 270 \pm 4$ nm/V. This is in good agreement with the manufacturers specifications for the total travel range of the translation axis of $25 \mu\text{m}/100$ V. The remaining difference can be attributed to the non-linear translation regime of the piezo.

As long as one operates in the linear regime from figure B.1, the distance Δs covered by the piezo is thus given by

$$\Delta s = k\Delta V. \quad (\text{B.2})$$

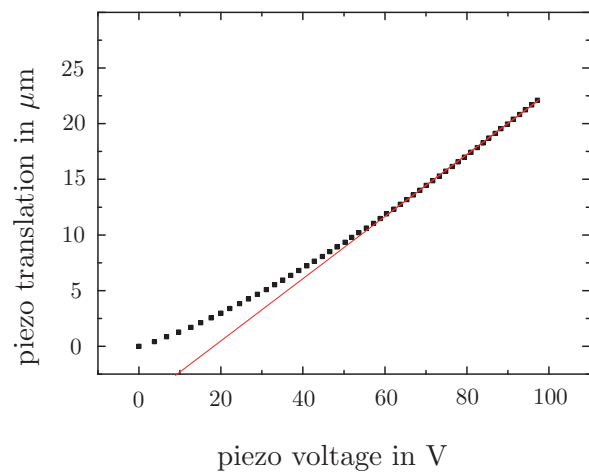


FIGURE B.1: Piezo calibration curve. Shown is the piezo translation per applied voltage. The solid line is a fit to the linear part with a slope of $k = (270 \pm 4) \text{ nm/V}$. The error bars are concealed by the data points.

List of Figures

2.1	Schematic of a telecommunication step index fibre	3
2.2	Plot of the Bessel functions of first and second kind	5
2.3	Plot of the modified Bessel functions of first and second kind	5
2.4	Schematic step-index fibre profile	6
2.5	Graphical solution for the TE and TM modes	10
2.6	Propagation constant β/k_0 over the V parameter	10
2.7	Graphical solution for the EH and HE modes	11
2.8	Evanescent field schematic for the HE_{11} mode	12
2.9	Perpendicular field components for the HE_{11}	14
2.10	Intensity distribution of the HE_{11} mode	15
2.11	Intensity distribution of the HE_{11} mode (Density Plot)	15
2.12	Radial intensity distribution of the HE_{11} mode at $\phi=0$	15
2.13	Radial intensity distribution of the HE_{11} mode at $\phi=\pi/2$	15
2.14	Perpendicular field components for the HE_{21}	17
2.15	Intensity distribution of the HE_{21} mode	17
2.16	Intensity distribution of the HE_{21} mode (density plot)	17
2.17	Radial intensity distribution of the HE_{21} mode in the x -direction	18
2.18	Radial intensity distribution of the HE_{21} mode in the y -direction	18
2.19	19
2.20	Intensity distribution of the TE_{01} mode	19
2.21	Intensity distribution of the TE_{01} mode (density plot)	19
2.22	Radial intensity distribution of the TE_{01} mode	20
2.23	Perpendicular electric field components for the TM_{01} mode	21
2.24	Intensity distribution of the TM_{01} mode	21
2.25	Intensity distribution of the TM_{01} mode (density plot)	21
2.26	Radial intensity distribution of the TM_{01} mode	22
3.1	AC-Stark-Shift in a two-level system	25
3.2	Normalised propagation constant β/k_0 over the V parameter for the first seven modes	27
3.3	Intensity distribution of two co-propagating modes	27
3.4	Decay length of the co-propagating HE_{11} and TE_{01} modes	28
3.5	Harmonic potential approximation of the trap potential	29
3.6	Azimuthal dependence of the potential of the $HE_{11}+TE_{01}$ trap	31
3.7	Longitudinal dependence of the potential of the $HE_{11}+TE_{01}$ trap	31
3.8	Radial dependence of the potential of the $HE_{11}+TE_{01}$ trap	31
3.9	Azimuthal dependence of the potential of the $HE_{11}+HE_{21}$ trap	34
3.10	Longitudinal dependence of the potential of the $HE_{11}+HE_{21}$ trap	34

3.11	Radial dependence of the potential of the $\text{HE}_{11}+\text{HE}_{21}$ trap	34
3.12	Potential of the $\text{HE}_{11}+\text{HE}_{21}$ trap along the direction of minimal potential barrier	34
3.13	Azimuthal dependence of the potential of the $\text{TE}_{01}+\text{HE}_{21}$ trap	36
3.14	Longitudinal dependence of the potential of the $\text{TE}_{01}+\text{HE}_{21}$ trap	36
3.15	Radial dependence of the potential of the $\text{HE}_{11}+\text{HE}_{21}$ trap	36
3.16	Radial dependence of the potential of the $\text{TE}_{01}+\text{TM}_{21}$ trap	37
3.17	Scheme for loading the $\text{HE}_{11}+\text{TE}_{01}$ trap	39
4.1	Schematic of the fibre tapering setup	42
4.2	Schematic of the diameter profile for an ultra thin fibre	42
4.3	Schematic of the experimental setup for the examination of the fibre modes during the pulling process.	43
4.4	Divergence of two different modes at the fibre output	44
4.5	45
4.6	Picture of a butterfly mode	45
4.7	Propagation constants of the HE_{11} , TE_{01} , TM_{01} and HE_{21} modes for a high V parameter	46
4.8	Superposition of higher order modes	46
4.9	Modulation of the butterfly mode during the fibre tapering process	47
4.10	Electron microscope pictures of two fibre waists	49
4.11	Surface intensity over radius for the HE_{11} and TE_{01} mode	50
4.12	Coupling of two fibres dependent on the coupling angle	52
4.13	Schematic of the experimental setup for the examination of the azimuthal and radial component of the evanescent field of the linearly polarised HE_{11} mode.	54
4.14	Fibre coupling setup	55
4.15	Angle between field fibre and probe fibre	56
4.16	Azimuthal dependence of the evanescent field around an ultra thin optical fibre	57
4.17	Decay of the evanescent field at the polarisation angle $\phi_1 = 50^\circ$ and a coupling angle of $\alpha_1 = 43^\circ$	59
4.18	Decay of the evanescent field at the polarisation angle $\phi_2 = 140^\circ$ and a coupling angle of $\alpha_1 = 43^\circ$	60
4.19	Decay of the evanescent field at the polarisation angle $\phi_3 = 150^\circ$ and a coupling angle of $\alpha_2 = 90^\circ$	61
4.20	Decay of the evanescent field at the polarisation angle $\phi_4 = 60^\circ$ and a coupling angle of $\alpha_2 = 90^\circ$	61
4.21	Standing wave coupling	63
4.22	Schematic of the experimental setup for the longitudinal examination of an evanescent field	64
4.23	Standing wave modulation measurement	65
A.1	Energy level scheme for ^{133}Cs	69
B.1	Piezo calibration curve	72

List of Tables

3.1	Comparison of the trapping parameters for the multimode traps.	40
4.1	Comparison of the decay constant of the evanescent field of a HE_{11} mode for different measurement methods	62

Bibliography

- [1] Newton I, *Opticks*, (Printed for W. Innys), 1730.
- [2] Quincke G, *Ann. Phys. Chem.* **127** 1, 1866.
- [3] Shewell J R and Wolf E, *Inverse Diffraction and a new Reciprocity Theorem*, J. Opt. Soc. Am. **58** 12, 1968.
- [4] Carniglia C K and Mandel L, *Quantization of evanescent electromagnetic waves*, Phys. Rev. D **2** 2, 1971.
- [5] Orucevic F, Lefèvre-Seguin V and Hare J, *Transmittance and near-field characterization of sub-wavelength tapered optical fibers*, Optics Express **15** 21, 2007.
- [6] Chu S, Bjorkholm J E, Ashkin A, Gordon J P, and Hollberg L W, *Proposal for optically cooling atoms to temperatures of the order of 10⁻⁶ K*, Physical Review A **11** 2, 1980.
- [7] Cook R J and Hill R K, *An electromagnetic Mirror for neutral atoms*, Opt. Commun. **43** 3, 1982.
- [8] Ovchinnikov Y B, Manek I and Grimm R, *Surface Trap for Cs atoms based on Evanescent-Wave Cooling*, Physical Review Letters **79** 12, 1997.
- [9] Ito H, Nakata T, Sakaki K and Ohtsu M, *Laser Spectroscopy of Atoms guided by evanescent waves in micron-sized hollow optical fibers*, Physical Review Letters **76** 24, 1996.
- [10] Tong L, Gattass R R, Ashcom J B, He S, Lou J, Shen M, Maxwell I and Mazur E, *Subwavelength-diameter silica wires for low-loss optical wave guiding*, Nature (London) **426** 816, 2003.
- [11] Ward J M, O'Shea D G, Shortt B J, Morrissey M J, Deasy K, and Nic Chormaic S G, *Heat-and-pull rig for fiber taper fabrication*, Rev. Sci. Instrum. **77** 083105, 2006.
- [12] Nayak K P, Melentiev P N, Morinaga M, Le Kien F, Balykin V I, and Hakuta K, *Optical Nanofiber as an efficient tool for manipulating and probing atomic fluorescence*, Opt. Express **15** 5431-5438, 2007.
- [13] Warken F, Rauschenbeutel A and Bartholomäus T, *Fiber Pulling Profits from Precise Positioning*, Photonics Spectra **42**(3) 73, 2008.
- [14] Patnaik A K, Liang J Q and Hakuta K, *Slow light propagation in a thin optical fiber via electromagnetically induced transparency*, Physical Review A **66** 063808, 2002.

- [15] Simhony S, Schnitzer I, Katzir A and Kosower E M, *Evanescent wave infrared spectroscopy of liquids using silver halide optical fibers*, J. Appl. Phys. **64** 7, 1988.
- [16] Messica A, Greenstein A and Katzir A, *Theory of fiber-optic, evanescent-wave spectroscopy and sensors*, Applied Optics **35** 13, 1996.
- [17] Dowling J P and Gea-Banacloche J, *Evanescent Light-Wave Atom Mirrors, Resonators, Waveguides, and Traps*, in Adv. At. Mol. Opt. Phys. **37** 1, 1996.
- [18] Le Kien F, Balykin V I, and Hakuta K, *Atom trap and waveguide using a two-color evanescent light field around a subwavelength-diameter optical fiber*, Physical Review A **70** 063403, 2004.
- [19] Vetsch et al., in preparation.
- [20] Hecht E, *Optics*, (Addison Wesley), 2001.
- [21] <http://www.newport.com>
- [22] Yariv A, *Optical Electronics*, (New York: CBS College), 1985.
- [23] Saleh B, Teich M, *Fundamentals of Photonics*, (John Wiley & Sons, Inc), 1991.
- [24] Spiegel M R, Liu J and Rapún L A, *Fórmulas y Tablas de Matemática Aplicada*, (McGraw-Hill Inc, USA), 2000.
- [25] Jackson J D, *Klassische Elektrodynamik*, (John Wiley & Sons, Inc), 1999.
- [26] Arens T, Hettlich F, Karfinger C, Kockelkorn U, Lichtenegger K and Stachel H, *Mathematik*, (Spektrum Akademischer Verlag Heidelberg), 2008.
- [27] Warken F, *Dissertation*, (Friedrich-Wilhelms-Universität Bonn), 2007.
- [28] Le Kien F, Liang J Q, Hakuta K, and Balykin V I, *Field intensity distributions and polarization orientations in a vacuum-clad subwavelength-diameter optical fiber*, Opt. Commun. **242** 445, 2004.
- [29] Scheck F, *Theoretische Physik 3 - Klassische Feldtheorie*, (Springer Verlag Berlin, Heidelberg, New York), 2004.
- [30] Little B E, Laine J P and Haus H A, *A single channel dropping filter based on a cylindrical microresonator*, Optics Communications, **167** 77, 1999
- [31] Sagué G, Vetsch E, Alt W, Meschede D and Rauschenbeutel A, *Cold-Atom Physics Using Ultrathin Optical Fibers*, Physical Review Letters **99** 163602, 2007.
- [32] Metcalf H J and van der Straaten P, *Laser Cooling and Trapping*, (New York: Springer), 1999.
- [33] Steck D A, *Caesium D line data*, <http://steck.us/alkalidata/>, 2008.
- [34] Alt W, *Dissertation*, (Friedrich-Wilhelms-Universität Bonn), 2004.

- [35] Ashkin A, *Laser in Life Sciences*, Berichte der Bunsen-Gesellschaft für Physikalische Chemie **93** 255, 1988
- [36] Boustimi M, Baudon J, Candori P, and Robert J, *Van der Waals interaction between an atom and a metallic nanowire*, Physical Review B **65** 155402, 2002.
- [37] Sagué G, *Dissertation*, (Friedrich-Wilhelms-Universität Bonn), 2008.
- [38] Bjorkholm J E, *Collision-limited lifetimes of atom traps*, Physical Review A **38** 3, 1988.
- [39] Chevrollier M, Bloch D, Rahmat G, and Ducloy M, *Van der Waals-induced spectral distortions in selective-reflection spectroscopy of Cs vapor: the strong atom-surface interaction regime*, Opt. Lett. **16** 1879, 1991.
- [40] Snyder A W and Love J D, *Optical Waveguide Theory*, (Boston: Kluwer Academic Publishers) 2000 .
- [41] Chu S, Hollberg L, Bjorkholm J E, Cable A and Ashkin A, *Three-dimensional viscous confinement and cooling of atoms by resonance radiation pressure*, Physical Review Letters **55** 48, 1985.
- [42] Townsend C G, Edwards N H, Cooper C J, Zetie K P, and Foot C J, Steane A M, Szriftgiser P, Perrin H, and Dalibard J, *Phase-space density in the magneto-optical trap*, Physical Review A **52** 1423, 1995.
- [43] Schlosser N, Reymond G and Grangier P, *Collisional Blockade in Microscopic Optical Dipole Traps*, Physical Review Letters **89** 023005, 2002.
- [44] Moar P N, Huntington S T, Katsifolis J, Cahill L W, Roberts A and Nugent K A, *Fabrication, modeling, and direct evanescent field measurement of tapered optical fiber sensors*, Journal of applied Physics **85** 3395, 1999.
- [45] Love J D and Henry W M, *Quantifying loss minimisation in singlemode fibre tapers*, Electron. Lett. **22** 912, 1986.
- [46] Knoll M and Ruska E, *Das Elektronenmikroskop*, Z. Physik **78** 318, 1932.
- [47] von Ardenne M, *Das Elektronen-Rastermikroskop*, Z. Physik A Hadrons and Nuclei, **109** 553, 1938.
- [48] Sumetsky M, *How thin can a fibre be and still guide light?*, Optics Letters **21** 870, 2006.
- [49] Landau L D and Lifshitz E M, *Quantum Mechanics*, (Pergamon), 1965.
- [50] Sumetsky M, Dulashko Y, Domachuk P and Eggleton B J, *Thinnest optical waveguide: experimental test*, Optics Letters **32** 754, 2007.
- [51] Maurer C, Jesacher A, Fürhaupter S, Bernet S and Ritsch-Marte M, *Tayloring of arbitrary optical vector beams*, New Journal of Physics **9** 78, 2007.

- [52] Bajcsy M, Hofferberth S, Balic V, Peyronel T, Hafezi M, Zibrov A S, Vuletic V, Lukin M D, *Efficient all-optical switching using slow light within a hollow fiber*, arXiv:0901.0336v1 [quant-ph].

Danksagungen/Acknowledgements

Das vergangene Jahr war eines der interessantesten, intensivsten und lehrreichsten meines Lebens. Das lag allem voran an der Entscheidung, meine Diplomarbeit in der Gruppe von Arno Rauschenbeutel durchzuführen. Nach der Vorstellung des Themengebietes seiner Gruppe empfahl er mir, bei der Entscheidung auf meinen Bauch zu hören. Das habe ich getan und ich habe es zu keinem Zeitpunkt bereut. Aus diesem Grund möchte ich ihm für die Möglichkeit danken, in diesem hochspannenden Teilgebiet der Physik tätig zu sein. Ich danke ihm für die nach außen getragene Begeisterung für seine Arbeit und für den stets wertvollen Input. Am allermeisten möchte ich ihm jedoch dafür danken, dass er es geschafft hat, eine unglaublich tolle Gruppe um sich herum zu sammeln und somit ein Arbeitsklima zu schaffen, welches seinesgleichen sucht. Vor allem die tollen Mitarbeiter sind dafür verantwortlich, dass man auch in schwierigen Zeiten jeden Tag gerne zur Arbeit geht.

Allen voran möchte ich hier meinem Betreuer, Dr. Guillem Sagué danken, der mir mit seinem enormen Wissen über den Zeitraum der Diplomarbeit stets zur Seite stand und an vielen Stellen entscheidende Hinweise geben konnte. Ich danke ihm auch vor allem dafür, dass er sich immer für mich Zeit genommen hat und für seine Geduld, wenn ich an einer Stelle konzeptionelle oder experimentelle Schwierigkeiten hatte.

Auch dem Rest der Arbeitsgruppe möchte ich meinen Dank aussprechen. Über den experimentellen Beistand hinaus, den ich von jedem Einzelnen erhalten habe, danke ich allen Rauschis:

Stefanie Barz für die Vereinfachung der Startzeit und dafür, dass sie meine Aufmerksamkeit auf die Gruppe gelenkt hat,

Dr. Ruth García Fernández für das freundliche Überlassen einer gemütliche Schlafcouch,
Andreas Jöckel für die gemeinsame Zeit im Labor, die durch die Überlappung im Musikgeschmack nur noch besser wurde,

Danny O'Shea für die lustige Zeit als Roomies in Stuttgart,

Michael Pöllinger für den reibungsfreien Ablauf des Postertransports von Mainz nach Hamburg,

Daniel Reitz für die Unterhaltungen beim Warten auf meinen letzten Bus,

Olga Rehband für die gemeinsamen Nachtschichten zum Ende der Schreibphase,

Alex II für die erste Staffel *Big Bang Theory*,

Regine Schmidt für den unvergesslichen humoristischen Klassiker betreffend ihrer Spam-Mails,

Ariane Stiebeiner für das Öffnen der Zwischentür in den immer richtigen Momenten,

Eugen Vetsch für *Oceansize*,

Andreas Vogler für die Einführung in den Triathlon,

und last but definitely not least Christian Wuttke für großartige Konzertabende.

Auch gruppenübergreifend herrschte ein gutes Klima, ich möchte hier stellvertretend der

Elektronengruppe um Dr. Herwig Ott, namentlich Tatjana Gericke, Andreas Koglbauer und Peter Würz für fachliche Hilfe und soziale Interaktion danken.

Den reibungsfreien Ablauf der organisatorischen Dinge garantierten Christine Best, Julia Doré und Elvira Stuck-Kerth, dafür ein herzliches Dankeschön.

Weiterhin geht ein großer Dank auch an die Institutswerkstatt, hier vor allem an Siegbert Felzer und Peter Becker für die rasche und zuverlässige Herstellung wichtiger Versuchskomponenten.

Natürlich ist ein solches Jahr nicht ohne den entsprechenden privaten Rückhalt zu überstehen. Hier danke ich meinen Eltern, Bettina und Norbert Baade sowie meinem Bruder Christoph Baade, Laura Döhring und Finja für wichtige Abende in familiärer Runde, von denen es hoffentlich jetzt wieder mehr gibt. Ich freue mich darauf und vor allem auf Finjas glückliches Gesicht, immer wenn sie mich sieht.

Auch meinen Freunden, allen voran Anne Feldmann, Steffi Kroog, Boris Michel, Svenja Möhring, Andreas Müllers, Tobias Ohnacker, Khorschid Qurban, Christian Rosenkranz und Nora Weyer möchte ich für den nötigen Rückhalt und den dringend benötigten Ausgleich danken.

Abschließend bin ich auch meiner WG dankbar, dass sich das Aufsuchen des Schlafplatzes nachts um halb eins (der sich hin und wieder auch auf überraschende Art und Weise verändert hatte) wirklich nach *Heimkommen* anfühlte. BEHOLD! Euer König kehrt zurück.

Erklärung

Hiermit erkläre ich, dass ich die vorliegende Arbeit in allen Punkten selbständig angefertigt und keine anderen Quellen und Hilfsmittel als die angegebenen verwendet habe.

Mainz, 9. März 2009

Alexander Baade